nature portfolio

Peer Review File

Cost-effective interfacial high-concentration electrolyte for stable lithium metal batteries

Corresponding Author: Professor Jiangxuan Song

This file contains all reviewer reports in order by version, followed by all author rebuttals in order by version.
Parts of this Peer Review File have been redacted as indicated to remove third-party material.

Version 0:

Reviewer comments:

Reviewer #1

(Remarks to the Author)
This is generally an interesting approach and the results are certainly remarkable. However, several points require further clarification, and some parts of the paper remain unclear, as described in detail below.

Comments:

- Abstract: Is it really meaningful to provide a decimal place for the specific energy (NOT energy density), given the still lab-scale nature of the pouch cell?
- Page 2, lines 44-45: “uniform Li deposition”?
- Figure 1: In which way did the authors investigate the direction of the Li+ transport in their work? The scheme indicates that it is rather random in the case of SCE, but ordered and unidirectional in the case of HCE. Moreover, why is the Li+ transport superior to SCE, the SEI superior to HCE, and the cost as low as in the case of SCE?
- The reasoning for the different polymer layers is not fully clear. Also oxygen can form hydrogen bonds. Can the authors provide quantitative values for getting an idea of the difference? Why would fluorine be favorable over an oxygen-rich environment (as in classic liquid and polymer electrolytes)?
- It appears that there is no link to Figure S1 in the main text. There is a link to a Figure S1, but that appears to refer to another content, no?
- Figure S3: A more detailed discussion of the FTIR data would be appreciated.
- Figure S4a: Where is this figure discussed?
- Page 4, line 104: It is not clear which liquid electrolyte was used here, yielding the given ionic conductivity.
- Figure 2c: What about the large pores in the polymer layer on the left?
- Figure 2e/S6: Following the earlier discussion, one would expect a higher N concentration in the PVDF-HFP domains, but this is not apparent from the provided images.
- Figure S8: A more detailed discussion of this figure would be appreciated. What’s the reason to use such microscope rather than a simple one?
- Figure S9: It’s not fully clear what exactly is shown here and how this supports the general discussion.
- Supp. Note 2: How much DME was used? How much of the soaked polymer? Generally, the experimental details appear to be missing.
- Figure S11: Does the dissolution follow a linear behavior?
- Figure 3c,d: The authors refer solely to the presence and impact of TFSI, but what about the cation? And the interaction of the anion with DME and/or PVDF-HFP is not clear. How does hydrogen bonding occur in such systems? Is this really relevant compared to the interaction of the cation? And what about the other polymer phase?
- The whole discussion of the interaction between the salt/solvent and the different polymer phases is unclear.
- Page 8, lines 183-184: How do free solvent molecules contribute to a high ionic conductivity?
- Where do the authors show the “rapid Li+ transport kinetics between the Li anode and the electrolyte”?
- Figure 4: What about lower current densities, frequently used in practical devices? Is the effect similar?
- Page 11, line 256: What do the authors refer to as “hysteretic Li+ transport”?
- Figure 5a: How come that the overpotential is lower at the same current density after the evaluation of varying current densities?
- How do the authors explain the differences concerning the Li+ transference number and the (apparent) activation energy (that term would require further discussion and clarification for the given system, in fact)? This is not obvious.

Generally, the concentration gradient of the Li salt remains to be clearly proven.
- Besides, it appears that the choice of the separator for the two reference systems is not discussed in the main text, although this is an essential parameter.
- 50 um Li is not “ultra-thin”. It’s thin, but still far too thick for practical applications. In this regard, it’s not clear why the authors increased the thickness to 100 um for the larger cell to demonstrate the potential practical impact.
- How was the specific energy calculated? Which parts of the cell were considered?
- The supplier information for the electrode and cell components appears to be missing.

Reviewer #2

(Remarks to the Author)
This manuscript presents a simple approach to decouple the Li salt concentration between Li-electrolyte interface and electrolyte bulk by employing a polymeric membrane made of PVDF-HFE and CPEGDA, which confines a high-concentration of LiTFSI at the interface via hydrogen-bonding and ion-dipole interactions, as claimed by the authors. This approach seems interesting, since it can obtain the advantage of high-concentration electrolyte by forming LiF-rich SEI at the electrochemical interface, while maintaining low viscosity in the electrolyte bulk with a regular Li salt concentration of 1 M. Nevertheless, some important issues remain not addressed and answered in the current form of manuscript as listed below. Therefore, I don't recommend to publish on Nature Communications.

1. Unclear lithium salt usage and cost implications:
A crucial issue is that the amount of Li salt used for a cell is not adequately clarified, which undermines the claim that this approach reduces costs. The authors argue that high concentration electrolyte is plagued by the high price and viscosity. However, in this work, since high concentration of LiTFSI must be pre-added into the polymeric membrane, the cost would be inevitably increased compared with 1 M electrolyte. The authors should give a clear and detailed description to evaluate the amount of salt used at each experiment step, to show what concentration of electrolyte it would correspond to for each cell. A direct comparison with a Li metal cell using only electrolyte (without the membrane) is essential. Furthermore, considering the cost of PVDF and CPEGDA, does this method truly offer a cost advantage? The manuscript would benefit from a thorough economic analysis.

2. Use of fluorinated materials:
The manuscript criticizes LHCEs for their use of toxic fluorinated ethers, claiming these are not environmentally friendly. However, this work also employs PVDF-HFE, a highly fluorinated material. Moreover, the total lithium salt usage in this study appears comparable to that in LHCEs (e.g., LiFSI-DME-TTE at a 1:1.2:3 molar ratio). Additionally, preparing this membrane is neither time- nor cost-efficient compared to the straightforward preparation of LHCE. The authors should clarify the pronounced advantages of this approach over LHCEs.

3. Unclear confinement effect:
Throughout the manuscript, I did not see convincing experimental results as to why the synthesized membrane can confine the Li salt. However, this is a key part for this work.

4. Mechanism extensibility:
The manuscript attributes the confinement effect to the hydrogen-bonding and ion-dipole interactions. How about the extensibility of this approach? I wonder if other materials with these microscopic forces can achieve a similar function or not.

5. Electrochemical stability:
The electrochemical stability of this membrane is questionable. Since the membrane contains plentiful C=O bonds, which are known to be extremely unstable towards Li metal. This raises concerns about whether the membrane would decompose during cell cycling. If so, can it maintain the function and still confine Li salt after long-term cycling? Experimental evidence addressing this concern is crucial.

6. Post-cycling characterization issues:
The characterization results are confusing. Since the authors put the membrane on the Cu substrate as the working electrode, how to remove it after cycling and perform characterization like SEM and SIMS? Does it mean that the membrane is not stable and disappears after cycling?

7. Ionic conductivity of the PVDF-HFP/CPEGDA layer:
The origin of ionic conductivity for the PVDF-HFP/CPEGDA layer is not clear. At line 104, page 4, the manuscript presents a high ionic conductivity of 1.4×10-2 mS/cm. It is strange that this layer without Li salt can have a high ionic conductivity. What’s the conducting agent in this layer?

8. Raman characterization details:
Please give a detailed description on the experimental set-up for Raman characterization of electrolyte and IHCE. How to characterize the IHCE layer with LiTFSI and DME?

9. Energy density calculations:
What rate is used for calculating the energy density (506.3 Wh kg-1) shown in the manuscript? And what’s the cell energy density at 0.5 C rate?

10. Membrane properties:
Can the membrane be self-supporting? With substrate like Cu, it can only be used in anode-free batteries, then its effectiveness in Li metal pouch cells drastically weakens.

Reviewer #3

(Remarks to the Author)
This work proposes a strategy to constrain a high salt concentration through a polymer at the electrolyte-electrode interface to enhance interfacial cycling performance. While this approach appears effective in the short term, a key question remains: how long such a salt-rich interface can be maintained to provide long-term benefits? Furthermore, Furthermore, I have some questions regarding the research to understand the salt-retention mechanism.
Part 2.1 explains how the IHCE was developed; however, the information on the standard bulk electrolyte used in this work is missing from this section. Instead, it is introduced later on page 7. This disrupts the logical flow and makes it difficult to follow and understand the discussions before knowing the bulk electrolyte composition.
Part 2.2 tried to verify the retention function of IHCE and the mechanism. I have a few questions regarding this part.
1) Although the soaking experiment provides insight into the salt retention capability of the IHCE materials, i.e. how well it can trap and hold the salt within the polymer matrix in the absence of the dynamics cycling conditions, however, it may not reflect the real battery conditions. In an actual battery, current flow, ion transport during charging and discharging, and electrochemical reactions continuously alter the salt concentration in the IHCE over time. Whether the IHCE can constrain salt during and after cycling is critical for the practical application of this strategy. In addition, if the electrolyte is not DME, it will also affect the result of the soaking experiment. It is not clear what electrolyte has been used.
2) FTIR shows interactions between PVDF-HFP and DME , and between TFSI and DME. However, the binding energy is a positive value here which raised questions. Typically, binding energy is negative for favorable interactions, indicating an exothermic process. A more positive binding energy value usually suggests weaker and less stable interactions. Based on the reported values, the DME-$TFSI^-$ interaction should be slightly stronger (2.26 vs. 2.84 kcal mol^{-1} for PVDF-HFP-$TFSI^-$). This contradicts the explanation provided in the text. Please clarify how these binding energies were calculated and provide details about the methodology.
3) MD simulation details:
The structural information of PVDF-HFP and CPEGDA in the simulation is unclear. For example: What does "20 units PVDF-HFP" refer to? Does it mean 20 polymer chains? What is the structure of each chain? How is CPEGDA connected to PVDF-HFP? Is it covalently linked or physically mixed? How was the COMPASS III force field validated for this specific system? Furthermore, the annealing process details are insufficient. What does "the lowest energy configurations" refer to? Is it the final configuration after annealing or a configuration chosen based on energy minimization criteria? Please provide additional information on the structural optimization and annealing protocols.
4) The stated purpose of the MD simulation is to understand the salt-retention mechanism. However, the absence of LiTFSI salt in the model invalidates this objective. The observed porosity results from the polymer structure and DME, which is expected as polymers generally exhibit free volumes. Without explicitly including salts, the simulation cannot capture the spatial effects of salts on pore size or provide insight into ion-polymer, solvent-polymer, or solvent-ion interactions. The discussion of pore size in the current system is thus meaningless. The simulation does not provide any meaningful insights into the salt-retention mechanism.
5) The Raman analysis part should also compare the IHCE (5 M LiTFSI-DME within a polymer matrix) to a 5 M LiTFSI-DME system without the polymer matrix to provide a more direct understanding of the polymer's role in modulating ion coordination and transport.

Version 1:

Reviewer comments:

Reviewer #1

(Remarks to the Author)
The comments have been very comprehensively addressed. I do not have any further comments anymore.

Reviewer #2

(Remarks to the Author)
This study presents the development of a salt-retaining polymer interfacial layer on electrode surfaces, successfully establishing a localized high-concentration electrolyte microenvironment at the electrode-electrolyte interface. Through comprehensive experimental investigations and computational verification, the research team has systematically addressed the key scientific questions raised during the peer-review process. While the study presents intriguing findings on anion retention by the polymer layer, I have significant reservations regarding the mechanistic interpretation and the claimed novelty of this work. These limitations prevent me to recommend this publication in Nature Communications:
1. High-concentration electrolytes (HCEs, >3 M salt concentration) have gained significant research attention due to their anion-involved solvation structures, which facilitates preferential anion migration to the electrical double layer (EDL) and form the inorganic-rich SEI. While the authors demonstrate the anion retention capability of this polymer layer, the mechanism by which the retained anions migrate into the EDL and subsequently influence the SEI or CEI remains unclear. Based on classical EDL theory and interfacial reaction kinetics, I question whether such anion retention would significantly alter the EDL structure or SEI/CEI formation dynamics. Could the localized ion redistribution caused by anion confinement

truly control the interphase-formation processes?
2. The novelty of this work is questionable because PVDF-based coatings on metal anodes have already been extensively explored in prior studies, albeit with differing mechanistic interpretations (Energy Storage Mater. 2020, 24, 588; Nano Lett. 2023, 23, 276). While the current study proposes anion retention as a new mechanism, the core material (PVDF) and its application to metal anodes lack originality.
3. The proposed anion confinement mechanism remains ambiguously attributed to a combination of physical entrapment, hydrogen bonding, and ion-dipolar interactions. However, the decisive factor remains unclear, weakening the mechanistic foundation of this work.

Reviewer #3

(Remarks to the Author)
I am happy with all responses and do not have further questions.

Version 2:

Reviewer comments:

Reviewer #2

(Remarks to the Author)
The author has carefully revised the manuscript and the solved all my concerns, now this manuscript can be published on Nat. Commun.

Response Letter to Reviews

Dear Reviewers,

We are grateful to the reviewers for providing valuable suggestions and feedback to improve the quality of our manuscript. The comments and questions raised by the reviewers have helped us clarify our arguments and sparked thoughts for future works. We respond to each question raised by the reviewer in blue, and highlight the changes made to our manuscript and supplementary information in yellow background for clarity.

Review #1 (Remarks to the Author):

Overall comment: This is generally an interesting approach and the results are certainly remarkable. However, several points require further clarification, and some parts of the paper remain unclear, as described in detail below.

Response: We are grateful for your recognition of the novelty of our approach and the strength of the results. Thank you also for the time and effort you devoted to reviewing and editing our manuscript. Your insightful and constructive comments have greatly helped us improve the quality and clarity of our work. In response, we have carefully revised the manuscript and provided a comprehensive point-by-point response to address all your concerns and suggestions you raised.

1. Abstract: Is it really meaningful to provide a decimal place for the specific energy (NOT energy density), given the still lab-scale nature of the pouch cell?

Response: We appreciate your careful reading and valuable feedback. The decimal value was initially provided to maintain consistency with the detailed results in the manuscript and emphasize the precision of our calculation. However, we agree that such precision is unnecessary given the lab-scale nature of the pouch cell. Accordingly, the specific energy "506.3 Wh kg^{-1}" has been corrected to "506 Wh kg^{-1}" throughout the revised manuscript highlighted with yellow background.

2. Page 2, lines 44-45: "uniform Li deposition"?

Response: Thanks for your kind reminder. We sincerely apologize for the inaccurate description regarding Li deposition behavior under standard concentration electrolytes. Following your suggestion, the phrase "uniform Li deposition" has been revised to "uneven Li deposition" in the revised version highlighted with yellow background for clarity.

3. Figure 1: In which way did the authors investigate the direction of the Li^+ transport in their work? The scheme indicates that it is rather random in the case of SCE, but ordered and unidirectional in the case of HCE. Moreover, why is the Li^+ transport superior to SCE, the SEI superior to HCE, and the cost as low as in the case of SCE?

Response: We sincerely appreciate the reviewer's insightful comments and the opportunity to clarify the advantages of our IHCE design. In response, we have provided a systematic explanation supported by experimental data and revised analyses to address your concerns.

(1) Li^+ transport direction.

Our study primarily focuses on the gradient-concentration electrolyte design rather than directional ion transport. We acknowledge that the original schematic in Fig. 1 may have unintentionally implied an ordered Li^+ transport pathway. Typically, Li^+ transport in liquid or quasi-solid electrolytes is governed by diffusion and migration under an applied electric field and does not follow a strictly ordered trajectory. To avoid misinterpretation, we have revised Fig. 1 (now Fig. R1) to remove directional arrows, emphasizing only the Li^+ concentration gradient across the interface and bulk electrolyte.

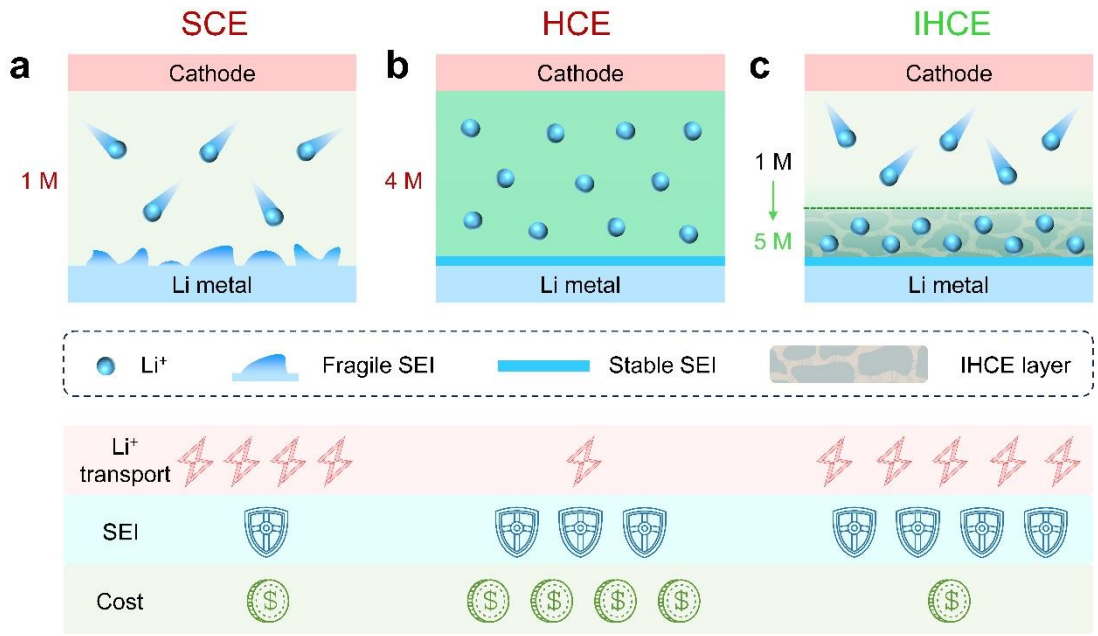

Fig. R1. Schematic for Li^+ distribution and drawbacks/advantages in different electrolytes. a, "Standard" concentration electrolyte (SCE): high ionic conductivity, fragile SEI, and low cost. b, High-concentration electrolyte (HCE): low ionic conductivity, robust SEI, and high cost. c, Interfacial high-concentration electrolyte (IHCE): high ionic conductivity in the bulk electrolyte, improved interfacial charge transfer kinetics, a robust SEI with an additional polymer protective layer, and low cost.

(2) Li^+ transport performance.

The superior ion transport in IHCE arises from the synergistic combination of a high-concentration electrolyte interfacial layer and a highly conductive bulk electrolyte. The bulk SCE (1 M LiTFSI-DME) exhibits an ionic conductivity of 7.6×10^{-3} S cm^{-1}, nearly twice that of HCE (4.0×10^{-3} S cm^{-1}, Supplementary Fig. 30), enabling rapid ion migration across the bulk electrolyte. Meanwhile, we conducted ionic conductivity measurements of the IHCE layer. As shown in Fig. R2 and Table R1 (updated in Supplementary Fig. 19 and Table 2), the IHCE exhibits an ionic conductivity of 1.1×10^{-3} S cm^{-1} within the interfacial layer, which is significantly higher than that of conventional artificial SEI layers (typically ~10^{-5} to 10^{-4} S cm^{-1})[1,2], highlighting the favorable ion transport across the IHCE layer. Furthermore, the Li^+ transference number of IHCE reaches 0.57, higher than HCE (0.42) and SCE (0.33) (Supplementary Fig. 27), indicating reduced anion polarization and more efficient Li^+ migration.

Tafel analysis shows that the exchange current density (j_0) of IHCE is 0.84 mA cm^{-2},

~2.8 times that of SCE (0.30 mA cm^{-2}) (Fig. 5e), confirming accelerated interfacial charge transfer. In addition, the activation energy (E_a) for Li^+ migration through SEI is lowest in IHCE (54.3 kJ mol^{-1}), compared to both SCE (58.9 kJ mol^{-1}) and HCE (80.6 kJ mol^{-1}) (Fig. 5f), reflecting reduced energy barriers for Li^+ mobility across SEI.

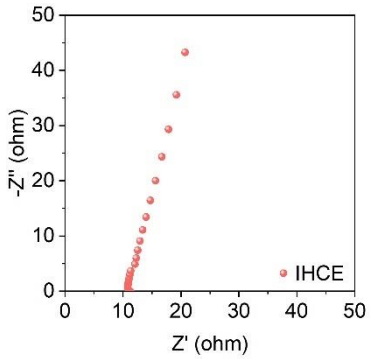

Fig. R2. Nyquist plots of the IHCE membranes at room temperature.

The ionic conductivities of the DME-swollen IHCE layer were evaluated using SS||SS symmetric cells by electrochemical impedance spectroscopy (EIS) test. The measured parameters are summarized in Supplementary Table 2 (now in Table R1). The ionic conductivities (σ) were calculated using Equation (1):

$$\sigma = \frac{L}{R_b S} \quad (1)$$

where "σ" is the ionic conductivity, "L" is the membrane thickness, "S" is the electrode area, and "R_b" is the bulk resistance obtained by AC impedance."

Table R1. The detailed parameters for the calculation of ionic conductivities of IHCE.

Polymer membrane	**L (cm)**	**R (Ω)**	**S (cm^2)**	**σ (S cm^{-1})**
IHCE (with DME)	0.025	11.2	2	1.12×10^{-3}

(3) SEI stability.

Although both IHCE and HCE promote the formation of LiF-rich SEI, as confirmed by Cryo-TEM (Supplementary Fig. 23) and TOF-SIMS (Fig. 4r, s). The SEI formed in IHCE is more mechanically and chemically stable, due to reduced solvent content and structural reinforcement from the polymer matrix. Based on electrolyte uptake (~30%,)

and the polymer content in the synthesized IHCE (9.5 wt%, Table R2), the DME content in the IHCE layer for a 6.8 Ah pouch cell is only ~1.3×10^{-4} g, representing a >99.99% reduction compared to SCE (6.59 g) or HCE (3.33 g), calculated using an E/C ratio of 1.29 g Ah^{-1}. This minimal solvent content helps mitigate SEI degradation and swelling. Detailed calculations and parameter descriptions are provided in Tables R2, 3 and Equations (2), (3). Additionally, the polymer-based IHCE layer provides mechanical support, maintaining a stable Young's modulus of ~1.56 GPa after 50 cycles (Fig. R3). This robust elasticity provides effective tolerance against volume fluctuation and helps prevent SEI rupture during cycling, contributing to long-term interfacial stability.

Table R2. DME content in the IHCE layer for 6.8 Ah pouch cell.

Li anode parameters			IHCE coating solution parameters				
Length (cm)	Width (cm)	Number	Unit-usage (μl cm^{-2})	Total usage (g)	Mass ratio of Synthesized IHCE in THF (wt%)	Polymer content in synthesized IHCE (wt%)	Polymer mass in IHCE layer (g)
8.2	6	13	2	2.27	0.2	9.5	4.3×10^{-4}
Solvent uptake of IHCE layer (wt%)			30				
DME content in IHCE layer (g)			**~1.3×10^{-4}**				

$$m_{total\ usage\ of\ IHCE\ coating\ solution} = m_{unit-usage\ of\ IHCE\ coating\ solution} \times L \times W \times N \times 2 \times \rho = 2 \times 8.2 \times 6 \times 13 \times 2 \times 0.889 \div 1000 = 2.27g \quad (2)$$

$$m_{\text{DME content in IHCE layer}} = m_{total\ usage\ of\ IHCE\ coating\ solution} \times \omega_{\text{Synthesized IHCE in THF}} \times \omega_{polymer\ in\ sythesized\ IHCE} \times \omega_{solvent\ uptake\ of\ IHCE} = 2.27 \times 0.2\% \times 9.5\% \times 30\% = 1.3 \times 10^{-4}g \quad (3)$$

Where "L", "W", and "N" are the length, width, and number of Li anode; "ρ" is density of the IHCE coating solution; "m" is the mass; "ω" is the mass ratio.

Table R3. Solvent content in 6.8 Ah Li||NCM811 pouch cells using SCE and HCE with an EC ratio of 1.29 g Ah^{-1}.

Formula		LiTFSI	DME
SCE (1 M)	Usage (g)	2.18	**6.59**
HCE (5 M)	Usage (g)	5.47	**3.33**

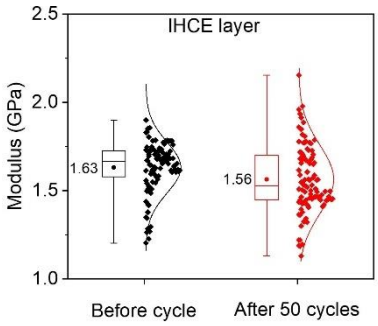

Fig. R3. Young's modulus distribution of the IHCE layer on Cu electrode before and after 50 cycles.

(4) Lithium salt usage and cost analysis.

To quantify the lithium salt consumption and associated cost, we conducted a detailed analysis using a practical 6.8 Ah Li||NCM811 pouch cell configuration specifically designed in this study (Supplementary Table 10), with an electrolyte-to-capacity (E/C) ratio of 1.29 g Ah^{-1}. All relevant parameters and discussion have been updated in Supplementary Note 10 and Supplementary Tables 12-15.

The IHCE system comprised an IHCE coating layer and a bulk electrolyte using the same composition as the SCE. Specifically, the IHCE coating solution was applied at a unit usage of 2 μl cm^{-2}, corresponding to ~1.78 mg cm^{-2}, based on its density of ~0.889 g cm^{-3}. Considering the electrode dimensions and double-sided coating on the Li foil, the unit usage of IHCE coating solution was ~0.33 g Ah^{-1} (Equation (4)). The solution contains 0.2 wt% synthesized IHCE in a THF diluent, with a LiTFSI content of 9.46 × 10^{-3} wt% (Equation (5)). Therefore, the IHCE layer contributes an additional but negligible amount of lithium salt: 3.16 × 10^{-5} g Ah^{-1} (Equation (6)).

$$m_{IHCE\ coating\ solution} = 2 \times L \times W \times N \times Unit - usage \div 6.8$$
$$= 2 \times 8.2 \times 6 \times 13 \times 1.78 \div 1000 \div 6.8 = 0.33\ g\ Ah^{-1} \quad (4)$$

$$\omega_{\text{LiTFSI in IHCE coating solution}} = \frac{m_{LiTFSI\ in\ sythesized\ IHCE}}{m_{sythesized\ IHCE}} \times \frac{m_{sythesized\ IHCE}}{m_{IHCE\ coating\ solution}} = \frac{0.46}{9.73} \times 0.2\% = 9.46 \times 10^{-3}\% \quad (5)$$

$$m_{LiTFSI\ in\ IHCE\ layer} = m_{IHCE\ coating\ solution} \times \omega_{\text{LiTFSI in IHCE coating solution}} = 0.33 \times 9.46 \times 10^{-3}\% = 3.16 \times 10^{-5}\ g\ Ah^{-1} \quad (6)$$

Where "ω" represents the mass ratio, "m" refers to mass, and "P" refers to cost. Where "L, W, N" represent length, width, and number of Li foil.

The bulk electrolytes were formulated as follows: the HCE consisted of 3 M LiDFOB + 2 M $LiBF_4$ in FEC/DEC (1: 2, v/v), while the SCE consisted of 0.6 M LiDFOB + 0.4 M $LiBF_4$ in FEC/DEC (1: 2, v/v), respectively. Based on Equations (7)-(10) and the experimental parameters summarized in Tables R4-7, the total lithium salt consumption per Ah was calculated to be ~0.126 g Ah^{-1} for SCE, ~0.425 g Ah^{-1} for HCE, and ~0.126 g Ah^{-1} for IHCE (including both SCE and IHCE layer). These results demonstrate that IHCE design achieves a ~70.4 % reduction in lithium salt usage compared to HCE, while remaining nearly identical salt consumption to SCE (~0.025% increase).

$$\omega_{LiDFOB\ (LiBF_4)} = \frac{m_{LiDFOB\ (LiBF_4)}}{m_{LiDFOB} + m_{LiBF_4} + m_{FEC} + m_{DEC}} \times 100\% \quad (7)$$

$$m_{LiDFOB\ (LiBF_4)} = C_{LiDFOB\ (LiBF_4)} \times V_{FEC+DEC} \times M_{LiDFOB\ (LiBF_4)} \quad (8)$$

$$m_{FEC\ (DEC)} = \rho_{FEC\ (DEC)} \times V_{FEC\ (DEC)} \quad (9)$$

$$m_{lithium\ salt} = m_{LiDFOB} + m_{LiBF_4} \quad (10)$$

Where "ω" represents the percentage of lithium salt relative to the total mass of the electrolyte; "m" refers to mass; "C" represents the concentration of lithium salt in electrolyte; "V" refers to volume; "ρ" represents densities of the electrolyte solvents.

For cost analysis, we considered all raw materials used for IHCE coating layer and electrolyte preparation. Prices were based on commercial suppliers, as detailed in the Methods Section and Supplementary Table 12. Using Equations (11)-(13), with all

relevant parameters summarized in Tables R4-7, the calculated costs for SCE, HCE and IHCE were ~1.25 \$ Ah^{-1}, ~1.65 \$ Ah^{-1}, and ~1.28 \$ Ah^{-1}, respectively. This result demonstrates that IHCE reduces cost by ~22.4% compared to HCE, while the added cost of the IHCE interfacial layer is minimal (increased by ~2.16% relative to SCE). This cost-effectiveness, combined with the performance advantages of IHCE, highlights its potential as a practical and scalable alternative for lithium metal batteries.

$$\begin{aligned} Cost\ of\ SCE &= P_{LiDFOB} \times m_{LiDFOB} + P_{LiBF_4} \times m_{LiBF_4} \\ &+ P_{FEC} \times m_{FEC} + P_{DEC} \times m_{DEC} \\ &= 2.18 \times 0.09 + 2.18 \times 0.04 + 1.42 \times 0.49 + 0.41 \times 0.67 \\ &= 1.25\ \$\ Ah^{-1} \end{aligned} \quad (11)$$

$$\begin{aligned} Cost\ of\ HCE &= P_{LiDFOB} \times m_{LiDFOB} + P_{LiBF_4} \times m_{LiBF_4} \\ &+ P_{FEC} \times m_{FEC} + P_{DEC} \times m_{DEC} \\ &= 2.18 \times 0.33 + 2.18 \times 0.1 + 1.42 \times 0.37 + 0.41 \times 0.49 \\ &= 1.65\ \$\ Ah^{-1} \end{aligned} \quad (12)$$

$$\begin{aligned} Cost\ of\ IHCE &= cost\ of\ IHCE\ membrane + cost\ of\ SCE \\ &= P_{IHCE\ coating\ solution} \times \frac{m_{IHCE\ coating\ solution}}{6.8} + 1.25 \\ &= 0.027 + 1.25 \\ &= 1.28\ \$\ Ah^{-1} \end{aligned} \quad (13)$$

Where "*p*" represents the unit-price of the specific electrolyte component, "*m*" is the mass.

Table R4. Raw materials usage and cost for IHCE synthesis.

Component	PVDF-HFP	LiTFSI	PEGDA	4-SH	AIBN	DMF
Mass (g)	0.74	0.46	0.15	0.035	0.0018	8.34
Density (g cm^{-3})	-	-	1.12	1.288	-	0.948
Unit-price (\$ g^{-1})	1.35	2.18	0.13	0.24	1.09	0.10
Cost (\$)	1.00	1.00	0.02	0.01	1.4×10^{-3}	0.82
Synthesized IHCE	Total mass (g)		9.73			
	Total cost (\$)		2.86			
	Unit-price (\$ g^{-1})		0.29			

Table R5. Usage and cost breakdown of the IHCE coating solution.

Component	Synthesized IHCE	THF	IHCE coating solution
Mass ratio	1	500	501
Density (g cm^{-3})	-	0.889	~0.889
Unit-price ($ g^{-1})	0.29	0.08	0.08
LiTFSI content in IHCE coating solution (%)			9.46×10^{-3}

Table R6. IHCE coating solution usage and cost for 6.8 Ah Li||NCM811 pouch cell.

Li anode parameters			IHCE coating solution parameters				
Length (cm)	Width (cm)	Number	Unit-price ($ g^{-1})	Total usage (g)	Unit-usage (g Ah^{-1})	Total cost ($)	Unit cost ($ Ah^{-1})
8.2	6	13	0.08	2.27	0.33	0.18	0.027

Table R7. Lithium salt usage and cost per Ah for 6.8 Ah Li||NCM811 pouch cells using SCE, HCE and IHCE with an E/C ratio of 1.29 g Ah^{-1}.

Electrolytes		LiDFOB	$LiBF_4$	FEC	DEC
Unit-price ($ g^{-1})		2.18	2.18	1.42	0.41
SCE	Formula	0.6 M	0.4 M	1: 2, v/v	
	Usage (g Ah^{-1})	0.088	0.038	0.49	0.67
	Cost ($ Ah^{-1})	0.19	0.08	0.71	0.27
HCE	Formula	0.6 M	0.4 M	1: 2, v/v	
	Usage (g Ah^{-1})	0.33	0.095	0.37	0.49
	Cost ($ Ah^{-1})	0.72	0.21	0.52	0.20
IHCE coating solution	Unit-cost ($ Ah^{-1})	Ratio of LiTFSI (%)	Unit-usage (g Ah^{-1})	LiTFSI usage (g Ah^{-1})	LiTFSI cost ($ Ah^{-1})
	0.027	9.46×10^{-3}	0.33	3.16×10^{-5}	6.88×10^{-5}

Summary		SCE	HCE	IHCE
	Salt usage (g Ah^{-1})	0.126	0.425	0.12603
	Salt cost ($ Ah^{-1})	0.27	0.93	0.27007
	Total cost ($ Ah^{-1})	1.25	1.65	1.28

4. The reasoning for the different polymer layers is not fully clear. Also oxygen can form hydrogen bonds. Can the authors provide quantitative values for getting an idea of the difference? Why would fluorine be favorable over an oxygen-rich environment (as in classic liquid and polymer electrolytes)?

Response: We sincerely appreciate the reviewer's insightful comment. Indeed, both oxygen (O) and fluorine (F) atoms are capable of participating in hydrogen bonding. In our IHCE system, selected as complementary components of the polymer matrix to balance mechanical integrity, ion transport, and interfacial stability. These two polymers exhibit a large Flory-Huggins interaction parameter (χ = 6.5 k), promoting phase separation and enabling the formation of a well-defined bicontinuous

microstructure (Fig. 2). PVDF-HFP, rich in F atoms, provides chemical robustness, film-forming integrity, and mechanical strength. CPEGDA, containing abundant ether (-C-O-C-) and carbonyl (C=O) groups, contributes to solvent uptake and Li^+ transport. While our initial discussion primarily focused on PVDF-HFP due to its higher mass fraction (80%) in the IHCE system, we fully agree that both the PVDF-HFP and CPEGDA phases contribute to Li^+ solvation and $TFSI^-$ immobilization.

To quantitatively assess the differences in anion-polymer interactions, we conducted DFT calculations comparing the binding energies between $TFSI^-$ and the two polymer components. The calculated binding energies for PVDF-HFP-$TFSI^-$, CEPGDA-$TFSI^-$, and DME-$TFSI^-$ are -15.03, -10.22, and -7.91 kcal mol^{-1}, respectively (Fig. R4). These results confirm that F-rich PVDF-HFP exhibits stronger interactions with $TFSI^-$ compared to O-rich CPEGDA or DME. This trend aligns with our SEM-EDS mapping results (Fig. R6), where N from $TFSI^-$ is enriched in F from PVDF-HFP regions. The enhanced anion-binding ability of PVDF-HFP may stem from the higher electronegativity of F (3.98) compared to O (3.44), rendering hydrogen atoms in PVDF-HFP more electropositive. These H atoms can more effectively engage in attractive interactions with the negatively charged $TFSI^-$. Furthermore, Wang et al.[3] demonstrated that in fluorinated ether solvents such as bis(3-fluoropropyl) ether, interact with $TFSI^-$ involves both H···F and H···O bonds. Notably, the H···F bonds are shorter than the H···O bond, indicating stronger interaction strength. These findings further support the notion that F-rich environments exhibit a superior ability to anchor $TFSI^-$ anions compared to O-rich counterparts (*Adv. Mater*. **2024**, 36, 2306462).

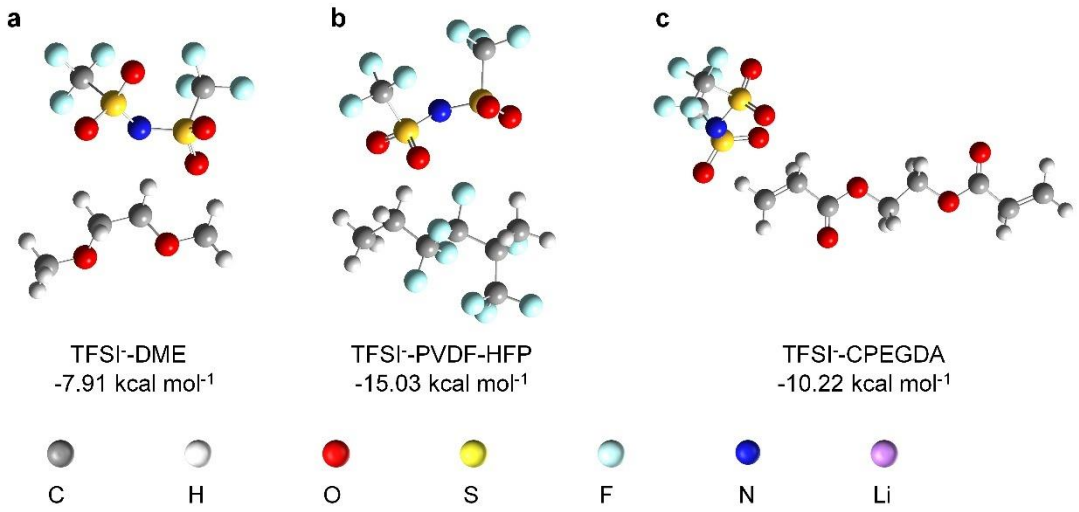

Fig. R4. Binding energies of $TFSI^-$ with DME (a), PPVDF-HFP (b) and CPEGDA (c).

5. It appears that there is no link to Figure S1 in the main text. There is a link to a Figure S1, but that appears to refer to another content, no?

Response: We sincerely thank the reviewer for pointing out the potential confusion regarding the reference to Figure S1 in the main text. We acknowledge that Figure S1 presents the contact angle measurements used to determine the Flory-Huggins interaction parameter (χ = 6.5 k), as detailed in Supplementary Note 1. However, the connection between the contact angle results and the calculation of χ was not clearly explained in the original version, potentially leading to confusion. To address this, we have revised both the main manuscript and supplementary information to clarify the relationship between the contact angle measurements in Figure S1 and the calculation of χ. The specific revisions are as follows:

(1) *Page 4, lines 95-98 in the revised Manuscript*

"As shown in Supplementary Table 1, PVDF-HFP and CPEGDA exhibit a large Flory-Huggins interaction parameter (χ = 6.5 k), determined through contact angle measurements (Supplementary Fig. 1 and Note 1), which facilitates the formation of a bicontinuous phase microstructure".

(2) *Page 2, Lines 29-31 in the revised Supplementary Information*

"Where Θ is the contact angle of two probe liquids (deionized water and glycerol)

on the substrate (PVDF-HFP and CPEGDA films), as shown in Supplementary Fig. 1, measured by contact angle measurements through DSA 30".

(3) *Page 3, Lines 35-37 in the revised supplementary information*

Addition of Supplementary Note l: "The above parameters and Flory-Huggins interaction parameters (χ = 6.5 k) calculated according to Equations (1-3), were summarized in Supplementary Table 1".

6. Figure S3: A more detailed discussion of the FTIR data would be appreciated.

Response: Thank you for your suggestion. We agree that a more detailed discussion of the FTIR data can help clarify the polymerization process. The FTIR spectra in Figure S3 illustrate the chemical bonding transformation during the synthesis of IHCE. Specifically, the characteristic absorption peak of the C=C bond in pure PEGDA at 1636 cm^{-1} and the S-H stretching vibration of 4-SH at 2570 cm^{-1} are observed in the spectra of the raw materials. After polymerization, both of these peaks disappear, indicating the successful reaction of the C=C groups in PEGDA and the S-H group in 4-SH via a "click reaction", resulting in the formation of a crosslinked polymer network. To improve clarity, we have updated Supplementary Note 2 (*Page 4, lines 44-51 in the revised Supplementary Information*) to provide a more detailed interpretation of the FTIR data shown in Supplementary Fig. 3, highlighting the chemical evolution during polymerization.

7. Figure S4a: Where is this figure discussed?

Response: We thank the reviewer for highlighting the need to clarify the discussion of Figure S4a in the main text. Figure S4a presents the Nyquist plots of the PVDF-HFP_m/$CPEGDA_n$ membranes with different weight ratios, used to calculate and optimize ionic conductivities. Although this figure was referenced in the context of ionic conductivity optimization, we realized that its specific role and the methodology for deriving ionic conductivities were not explicitly discussed, potentially leading to confusion. To address this, we have revised the manuscript and supplementary information as follows:

(1) *Page 4, lines 108-111 in the revised Manuscript*

"High ionic conductivity of 1.4 × 10^{-5} S cm^{-1}, as well as tensile strength of 91 MPa, were obtained at a PVDF-HFP/CPEGDA weight ratio of 8: 2 with 50 wt% LiTFSI, as demonstrated by Nyquist plots (Supplementary Fig. 4a and Table 2) and stress-strain curves (Supplementary Fig. 4b)."

(2) *Page 4, lines 57-63 in the revised Supplementary Information*

Addition to Supplementary Note 3: "The ionic conductivities of PVDF-HFP_m/$CPEGDA_n$ membranes were evaluated using SS||SS symmetric cells by electrochemical impedance spectroscopy (EIS) test. The measured parameters are summarized in Supplementary Table 2 (now in Table R8). The ionic conductivities (σ) were calculated using Equation (14):

$$\sigma = \frac{L}{R_b S} \tag{14}$$

where σ is the ionic conductivity, L is the membrane thickness, S is the electrode area, and R_b is the bulk resistance obtained by AC impedance."

Table R8. The detailed parameters for the calculation of ionic conductivities.

Polymer membrane	L (cm)	R (Ω)	S (cm^2)	σ (S cm^{-1})
PVDF-HFP_2/$CPEGDA_4$	0.028	96	2	1.46×10^{-5}
PVDF-HFP_4/$CPEGDA_6$	0.03	824	2	1.82×10^{-5}
PVDF-HFP_6/$CPEGDA_4$	0.03	840	2	1.79×10^{-5}
PVDF-HFP_8/$CPEGDA_2$	0.027	966	2	1.40×10^{-5}

8. Page 4, line 104: It is not clear which liquid electrolyte was used here, yielding the given ionic conductivity.

Response: We sincerely appreciate the reviewer's careful reading and valuable comment. We acknowledge that the original manuscript (now in *Page 4, lines 108-109*) did not explicitly clarify the measurement conditions for the reported ionic conductivity. To clarify, the ionic conductivity value (1.4 × 10^{-5} S cm^{-1}) was measured directly from

the PVDF-HFP$_8$/CPEGDA$_2$ polymer membrane with 50 wt% LiTFSI, without any added liquid electrolyte. LiTFSI was incorporated into the polymer matrix during the synthesis process, serving as the conducting species. The measurement was performed using EIS, as detailed in our response to Comment 7 and further described in Supplementary Note 3.

9. Figure 2c: What about the large pores in the polymer layer on the left?

Response: Thanks for your careful observation. We acknowledge that the original cross-sectional SEM image in Figure 2c may have exhibited surface irregularities arising from uneven incision during manual vertical cutting with a surgical blade. The non-uniform pressure applied during this process likely introduced artifacts that were mistakenly interpreted as large pores. To address this, we have performed new cross-sectional samples and acquired an updated SEM image. As shown in Fig. R5, the cross-sectional SEM image shows a uniform and compact structure without large-scale defects, confirming that the previously observed "pores" were indeed artifacts of sample preparation rather than inherent porosity of the polymer layer. Accordingly, we have replaced the original Figure 2c in the revised manuscript with the updated SEM image.

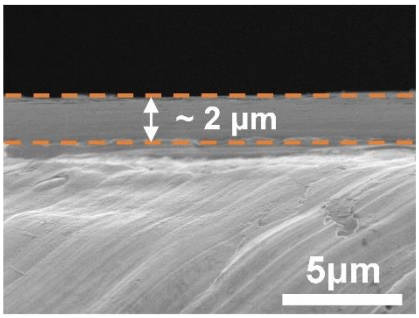

Fig. R5. Cross-sectional SEM images of dry-IHCE coated on Cu.

10. Figure 2e/S6: Following the earlier discussion, one would expect a higher N concentration in the PVDF-HFP domains, but this is not apparent from the provided images.

Response: Thank you for your valuable comment. In response, we have re-measured the EDS with extended acquisition time to improve the signal-to-noise ratio. The

updated results confirm that N concentration is indeed higher in the PVDF-HFP phase. However, due to the inherently low N content (~2.9 wt%) compared to F from PVDF-HFP (~56.8 wt%) and O from CPEGDA (~40.3 wt%), the N signal remains relatively weak. This limited signal intensity results in less distinct contrast and phase boundaries in the N elemental map compared to F or O mapping. We have updated Figure 2e and Supplementary Fig. 5 with the new EDS maps (now in Fig. R6)

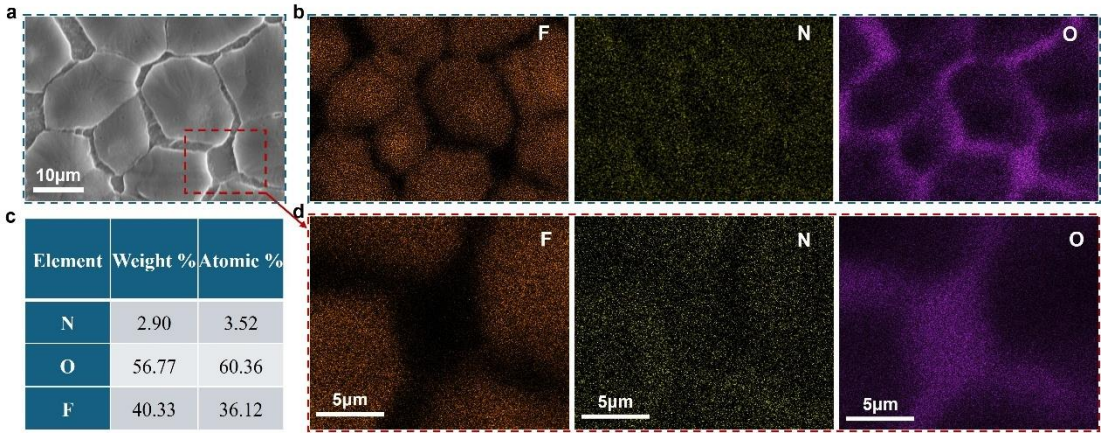

Element	Weight %	Atomic %
N	2.90	3.52
O	56.77	60.36
F	40.33	36.12

Fig. R6. SEM images and corresponding electron energy loss spectroscopy elemental mapping of dry-IHCE.

11. Figure S8: A more detailed discussion of this figure would be appreciated. What's the reason to use such microscope rather than a simple one?

Response: Thanks for your valuable suggestion regarding Figure S8. An ECLIPSE LV100N POL polarizing optical microscope (POM) was employed without polarization plates, effectively functioning similarly to a conventional microscope. The POM observations served as a complementary technique to SEM, providing supportive evidence of the structural features and distribution within the IHCE membrane at a broader scale. The macroscopic insights gained from POM are in agreement with the high-resolution surface morphology revealed by SEM, thereby reinforcing the reliability of our structural characterization. To more clearly express this point, we have made corresponding revisions to the revised Manuscript.

Compared with simple microscopes, the ECLIPSE LV100N POL microscope provides significant advantages in illumination quality. Conventional optical

microscopes typically use incandescent lamps, which often suffer from insufficient intensity, stability issues, and undesired heating, potentially leading to optical aberrations. In contrast, the ECLIPSE LV100N POL is equipped with an advanced high-brightness halogen light source with optimized filament size and increased light-source volume. This configuration significantly enhances brightness, ensuring uniformly bright illumination across the entire viewing field. Specifically, when using objectives of 50× magnification or higher, the brightness obtained is approximately 20-40% greater compared to a standard 100 W halogen lamp, thereby substantially improving image clarity and quality.

Updates in the main text of the revised Manuscript (Page 5, lines 121-122):

"This observation was further supported by polarizing optical microscopy (POM), which provided macroscopic evidence consistent with SEM observations (Supplementary Fig. 6)."

Updates in the Methods section of revised Manuscript (Page 17, lines 441-443):

"A polarized optical microscope (POM, ECLIPSE LV100N POL) and a confocal laser scanning microscope (CLSM, Leica TCS SP8 STED) were employed to characterize the phase structure of the dry IHCE membrane. The POM was operated without polarizers, functioning as a high-performance optical microscope to provide macroscopic structural insights that complement the high-resolution SEM observations."

12. Figure S9: It's not fully clear what exactly is shown here and how this supports the general discussion.

Response: Thank you for the comment. Figure S9 (now in Supplementary Fig. 7) presents 3D laser scanning confocal microscope (LSCM) images of the IHCE membrane, providing depth-resolved visualization of the spatial distribution of PVDF-HFP within the polymer matrix. Unlike SEM, which provides only surface or near-surface information, LSCM enables non-destructive optical sectioning of thicker membranes. To distinguish between the polymer phases, Nile Red was used as a fluorescent label. Since PVDF-HFP is hydrophobic, it preferentially absorbs Nile Red

and appears red in the LSCM images, whereas the hydrophilic CPEGDA remains non-fluorescent and dark. The consistent red fluorescence throughout the top-view and cross-sectional LSCM images (Supplementary Fig. 7a, b) confirms that a uniform dispersion of PVDF-HFP across the IHCE membrane, with no evidence of large-scale phase aggregation. Supplementary Fig. 7c further supports this by providing a 3D dynamic demonstration that illustrates the homogeneous distribution of PVDF-HFP phase. These observations complement SEM-EDS maps and support the conclusion that the IHCE membrane exhibits a well-defined and continuous phase-separated structure.

Updated in the revised Manuscript (Page 5, lines 123-127):

"3D laser scanning confocal microscope images (Supplementary Fig. 7) show that PVDF-HFP, selectively labeled with Nile Red, is uniformly distributed throughout the IHCE membrane. This uniform phase distribution ensures consistent polymer blending without large-scale phase separation, contributing to the structural stability and ionic transport properties of IHCE."

13. Supp. Note 2: How much DME was used? How much of the soaked polymer? Generally, the experimental details appear to be missing.

Response: Thank you for your valuable comment. To clarify, we have updated the Supplementary Information to include detailed experimental parameters regarding the dissolution analysis of LiTFSI from the IHCE membrane. As described in Supplementary Note 4, we used UV-Vis spectroscopy to monitor the LiTFSI dissolvation behavior. To prevent potential adsorption of LiTFSI onto cuvette walls, we employed a parallel sampling strategy: Seven identical IHCE membranes were individually immersed in 3 ml of anhydrous DME and sealed in an argon-filled glove box for 2, 5, 10, 20, 30, 40, and 50 days, respectively. The corresponding masses of each IHCE membrane were 39.99, 39.99, 39.60, 40.19, 40.93, 41.93, and 41.63 mg, respectively. Based on the synthesis protocol, the mass ratio of LiTFSI and the polymer to the total IHCE was 33.2% and 66.8%, respectively (Table R9), allowing us to

estimate the initial LiTFSI content in each membrane (Table R10). After soaking, the concentration of dissolved LiTFSI in DME was quantified using UV absorbance and calculated via Equations (15), (16). The residual LiTFSI content in each membrane was then calculated based on Equation (17), and the results are presented in Table R11. All relevant procedures, equations, and data tables have now been added or revised in Supplementary Note 4 and Supplementary Tables 4-6 to ensure clarity and reproducibility.

Table R9. Parameters of synthesized IHCE.

Components	PVDF-HFP	LiTFSI	PEGDA	4-SH
Mass (g)	0.74	0.46	0.15	0.035
Total mass of polymer matrix (g)	0.925			
Total mass of dry-IHCE (g)	1.385			
Ratio of LiTFSI in dry-IHCE (%)	33.2			
Ratio of polymer in dry-IHCE (%)	66.8			

Table R10. Usage of DME and dry-IHCE for UV experiments.

Time (day)	Usage of DME (ml)	Soaked dry-IHCE (mg)	Initial LiTFSI content in dry-IHCE (mg)
2	3	39.99	13.28
5	3	39.99	13.28
10	3	39.60	13.15
20	3	40.19	13.35
30	3	40.93	13.60
40	3	41.93	13.93
50	3	41.63	13.83

Standard curve equation:

$$y = 0.5253 \times x + 0.1325 \quad (15)$$

$$m_{dissolved\ LiTFSI} = x \times V_{DME} = \frac{y - 0.1325}{0.5253} \times 3 \tag{16}$$

$$\begin{aligned} C_{residual\ LiTFSI\ in\ IHCE} &= \frac{m_{residual\ LiTFSI\ in\ IHCE}}{M_{LiTFSI} \times V_{solvent\ uptake\ of\ IHCE}} \\ &= \frac{m_{LiTFSI\ in\ dry-IHCE} - m_{disssolved\ LiTFSI}}{287.09 \times \frac{m_{polymer\ in\ dry-IHCE} \times 30\%}{\rho_{DME}} \times 10^{-3}} \\ &= \frac{\left(m_{dry-IHCE} \times 0.332\right) - \left(\frac{y - 0.1325}{0.5253} \times 3\right)}{287.09 \times \frac{m_{dry-IHCE} \times 0.668 \times 30\%}{0.867} \times 10^{-3}} \end{aligned} \tag{17}$$

Where "*y*" represents the UV absorbance of the LiTFSI-DME solutions. "*x*" is the mass concentration of LiTFSI-DME solutions. "*m*" is the mass. "*V*" is the volume. "*ρ*" is the density of DME solvent. "*C*" indicates the molar concentration.

Table R11. Parameters of UV experiments.

Time (day)	UV absorbance (y)	LiTFSI in DME		Residual LiTFSI in IHCE	
		Concentration (x, mg ml^{-1})	Mass (mg)	Mass (mg)	Concentration (M)
2	0.623	0.934	2.802	10.48	3.95
5	0.632	0.952	2.855	10.43	3.93
10	0.632	0.951	2.853	10.30	3.92
20	0.686	1.054	3.162	10.18	3.82
30	0.735	1.146	3.438	10.16	3.74
40	0.803	1.276	3.829	10.10	3.63
50	0.846	1.359	4.078	9.75	3.53

14. Figure S11: Does the dissolution follow a linear behavior?

Response: Thank you for your comment. The dissolution data presented in Figure S11 (now in Supplementary Fig. 9) do not follow a strictly linear behavior over 50 days. Instead, it exhibits a three-stage dissolution behavior, reflecting a complex interplay of polymer-ion interactions and solvent penetration effects. In the initial stage (0-2 days),

a sharp decrease in LiTFSI concentration occurs, with a leakage of ~1.05 M, corresponding to a high daily dissolution rate of ~52.5%. This rapid loss is attributed to the release of surface-adsorbed or weakly bound LiTFSI species that are not strongly retained within the IHCE matrix, making them readily extracted by the electrolyte. In the intermediate stage (2-20 days), the dissolution rate significantly slows to ~0.72% per day. This suggests that the remaining LiTFSI is more strongly retained by the polymer matrix, likely due to physical confinement and molecular interactions within the IHCE structure, which effectively restrict further ion leaching. Beyond 20 days, the dissolution rate increases again to ~0.97% per day, likely due to long-term polymer relaxation and swelling. Over time, deeper solvent infiltration disrupts the ionic network, enhancing the mobility of previously confined ions and leading to an acceleration in dissolution. Despite these trends, the residual LiTFSI concentration in IHCE remained at 3.53 M after 50 days in DME, demonstrating its strong salt-retention capability.

15. Figure 3c,d: The authors refer solely to the presence and impact of TFSI, but what about the cation? And the interaction of the anion with DME and/or PVDF-HFP is not clear. How does hydrogen bonding occur in such systems? Is this really relevant compared to the interaction of the cation? And what about the other polymer phase? The whole discussion of the interaction between the salt/solvent and the different polymer phases is unclear.

Response: We sincerely appreciate the reviewer's insightful comments. To address your questions, we performed DFT calculations and spectra analysis to carefully clarify your concerns.

(1) Li^+ interactions.

Li^+ serves as the primary charge carrier, exhibiting strong coordination with DME via ion-dipole interactions (binding energy: -69.13 kcal mol^{-1}, Fig. R7a) through ether oxygen (-C-O), enabling rapid Li^+ migration via solvent channels. Li^+ also exhibits moderate interaction with CPEGDA via -C-O and carbonyl (C=O) groups, with a

binding energy of -45.35 kcal mol^{-1} (Fig. R7c). These functional groups provide reversible desolvation sites, facilitating Li^+ hopping transport via dynamic adsorption-desorption equilibria. In contrast, Li^+ forms weaker C-F···Li^+ interactions with PVDF-HFP (-40.17 kcal mol^{-1}, Fig. R7b). These findings are consistent with ^7Li NMR spectra (Fig. R8), which show upfield chemical shifts of Li^+ from DME to CPEGDA and then to PVDF-HFP, indicating a gradual decrease in solvation strength and confirming the distinct Li^+ coordination environments in IHCE compared to the bulk electrolyte.

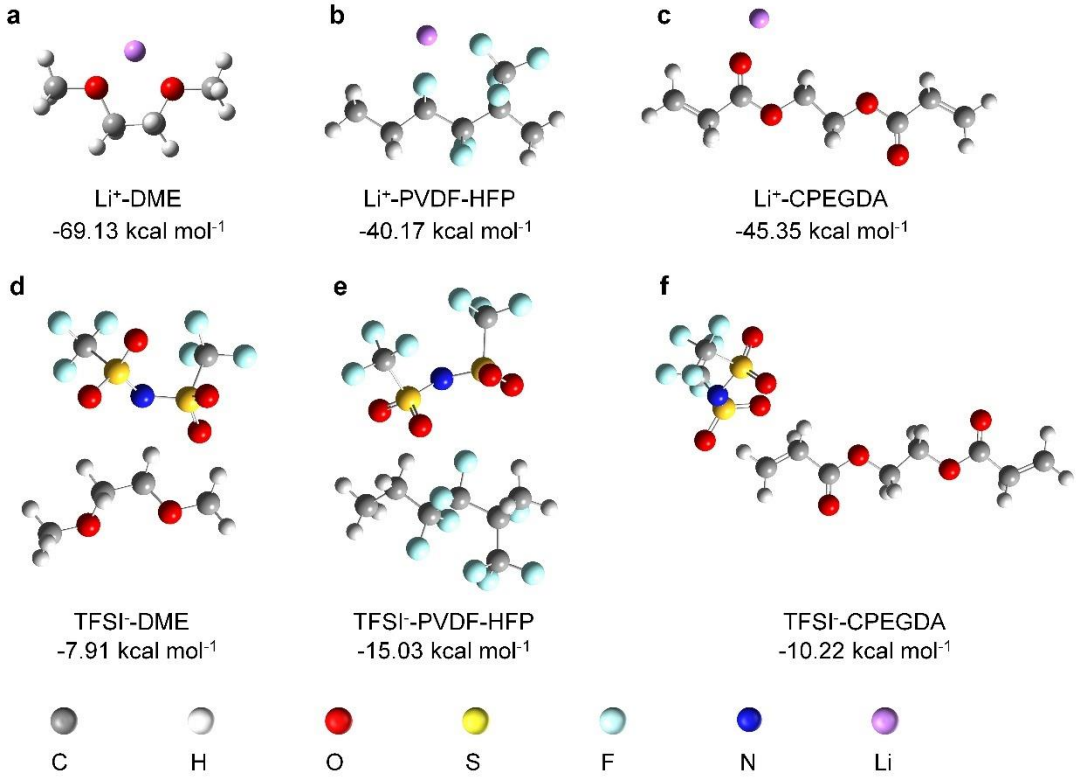

Fig. R7. Binding energies of different systems.

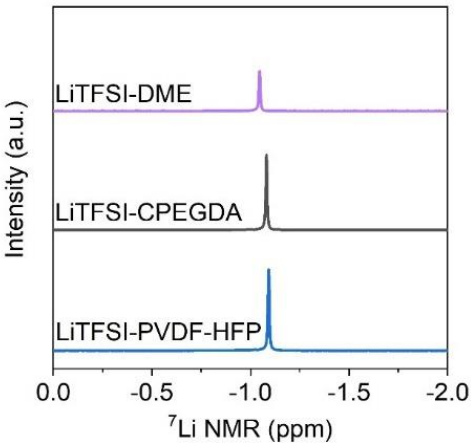

Fig. R8. ^{7}Li NMR spectra of LiTFSI-DME, LiTFSI-CPEGDA, and LiTFSI-PVDF-HFP.

(2) $TFSI^-$ interactions and hydrogen bonding.

$TFSI^-$ anions are immobilized within the IHCE network via preferential interactions with both polymer phases to suppress salt leakage. DFT calculations (Fig. R7) reveal binding energies of $TFSI^-$ with PVDF-HFP (-15.03 kcal mol^{-1}) and with CPEGDA (-10.22 kcal mol^{-1}) are substantially stronger than with DME (-7.91 kcal mol^{-1}). These results suggest that $TFSI^-$ tends to localize within the polymer matrix rather than diffusing freely into the bulk electrolyte. Upon DME coordination, ternary complexes such as PVDF-HFP-DME-$TFSI^-$ and CPEGDA-DME-$TFSI^-$ were formed, exhibiting enhanced binding energies of -19.26 kcal mol^{-1} and -22.6 kcal mol^{-1}, respectively (Fig. R9). This indicates that DME serves not only as a Li^+ solvent but also as a coordination bridge that stabilizes the anion-polymer interactions via ion-dipole and hydrogen-bond-like forces.

These results are supported by spectroscopic evidence. FTIR measurements (Fig. 3f) show that the -CF_2 of PVDF-HFP in the dry IHCE membrane shifts from 1063 and 1147 cm^{-1} to 1056 and 1133 cm^{-1} upon the introduction of DME and $TFSI^-$, indicating the formation of -F···H hydrogen bonds. Similarly, ^{1}H NMR spectra reveal downfield shifts from 3.30 and 3.33 ppm in PVDF-HFP-DME to 3.48 and 3.51 ppm in PVDF-HFP-DME-$TFSI^-$ systems (Fig. 3g), consistent with the formation of H···F and H···O interactions among DME, $TFSI^-$, and PVDF-HFP.

Furthermore, electrostatic potential (ESP) analysis (Fig. R10) shows that DME in

PVDF-HFP-DME and CPEGDA-DME complexes exhibits higher local ESP maximum (+15.3 and +10.4 kcal mol^{-1}) and less negative ESP minimum (-31.7 and -25.6 kcal mol^{-1}) compared to pure DME (+12.4 and -42.1 kcal mol^{-1}). This shift is attributed to the strong electron-withdrawing effect of the fluorinated PVDF-HFP backbone and polar oxygenated groups in CPEGDA, which enhances the electropositivity of the DME hydrogen atoms. This redistribution of electron density leads to stronger electrostatic attraction between the positively polarized hydrogen atoms and the negatively charged $TFSI^-$ anions, thereby reinforcing anion immobilization within the polymer matrix. The cooperative effect of these interactions effectively anchors $TFSI^-$ within the polymer framework, supporting the salt-retention functionality of the IHCE matrix.

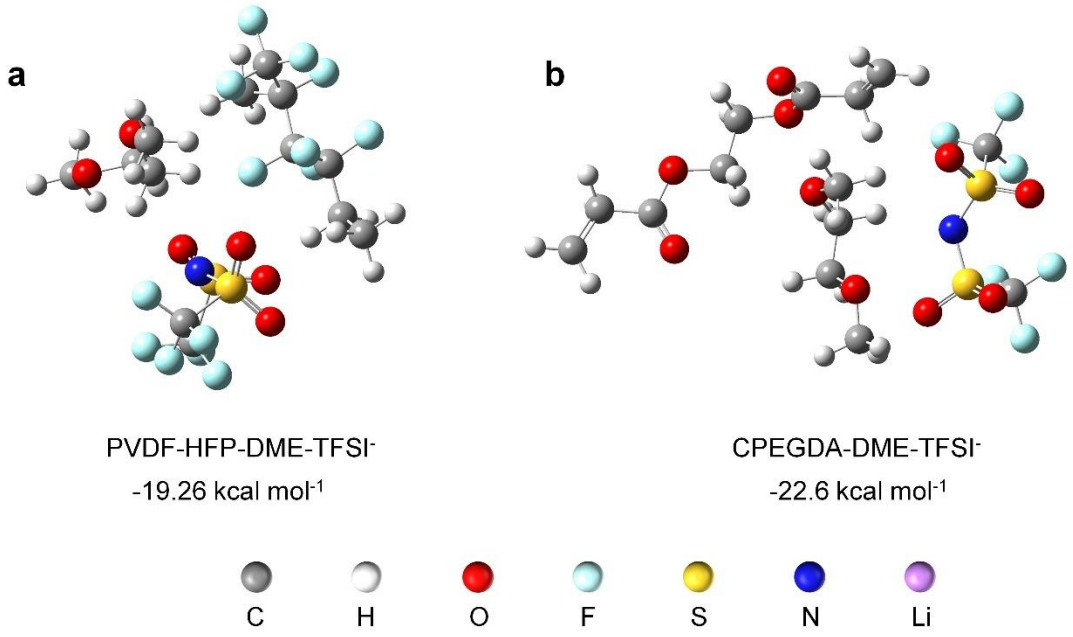

Fig. R9. a, b, The calculated binding energies of $TFSI^-$ with PVDF-HFP-DME (a) and CEPGDA-DME (b).

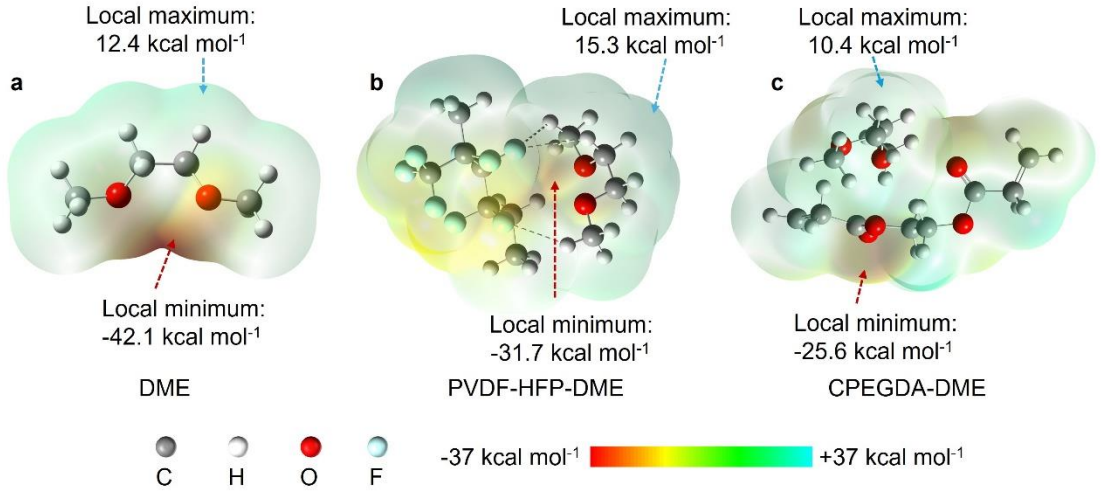

Fig. R10. The electrostatic potential (ESP) variations of DME (a) upon coordination with PVDF-HFP (b) or CPEGDA (c).

(3) Comparison of Li and $TFSI^-$ interactions.

The functions of Li^+ and $TFSI^-$ in IHCE are fundamentally different. Li^+ must remain mobile to support ionic conductivity. Its transport is facilitated by the Li^+-hopping sites provided by CPEGDA phase and DME-rich transport channels. $TFSI^-$ must be immobilized to prevent salt leakage and maintain interfacial concentration. Its retention relies on strong interactions with the polymer matrix, particularly PVDF-HFP, and is further enhanced by ternary coordination and hydrogen-bond-like interactions. This functional divergence ensures a decoupling between ionic conductivity and salt retention, allowing IHCE to exhibit a high Li^+ transference number (Fig. 5d) and stable electrochemical performance.

(4) Roles of CPEGDA phase.

CPEGDA, enriched with O-containing groups, plays a dual role within the IHCE matrix. It promotes Li^+ solvation and enhances compatibility with DME, facilitating the formation of continuous ion transport pathways. In addition, CPEGDA contributes moderately to $TFSI^-$ anchoring, as supported by binding energy (-10.22 kcal mol^{-1}) and ESP results. Its presence ensures dynamic Li^+ transport pathways and complements the anion-anchoring function of PVDF-HFP.

In summary, Li^+ and $TFSI^-$ exhibit distinct interactions with the solvent and polymer

matrix. Li^+ transport benefits from coordination with DME and CPEGDA, supporting fast ionic conduction. While $TFSI^-$ is selectively confined via strong polymer binding and hydrogen-bond-like interactions, especially with PVDF-HFP. This cooperative architecture enables the IHCE to simultaneously achieve high conductivity, stability, and salt retention.

16. Page 8, lines 183-184: How do free solvent molecules contribute to a high ionic conductivity?

Response: Thank you for your insightful question. Free solvent molecules enhance ionic conductivity primarily by increasing the number of mobile charge carriers and promoting faster Li^+ transport. In high-concentration electrolytes, Li^+ tends to coordinate with multiple anions, forming contact ion pairs (CIPs) and aggregates (AGGs). These large solvation clusters hinder Li^+ transport due to increased hydrodynamic radius and sluggish desolvation kinetics, ultimately limiting high-rate cycling performance[4–6].

This behavior can be described by the Stokes-Einstein relation (Equation (18))

$$D = \frac{k_B T}{6\pi\eta R} \tag{18}$$

where D is the diffusion coefficient, k_B is the Boltzmann constant, T is temperature, η is viscosity and R is hydrodynamic radius of the ion cluster. According to this relation, reducing R leads to an increase in D. In this context, free solvent molecules promote the formation of solvent-separated ion pairs (SSIPs) by weakening Li^+-anion interactions, thus reducing cluster size (R) and increasing Li^+ diffusivity.

Furthermore, the Nernst-Einstein relation (Equation (19))[5]:

$$\Lambda = \sum \frac{F^2}{RT}(\upsilon z^2 D) \tag{19}$$

shows that ionic conductivity (Λ) is directly proportional to diffusion coefficient (D), the number of mobile ions (υ), and their charge (z). Therefore, by enhancing the fraction of SSIPs, free solvent molecules increase both the mobility (D) and number of charge

carriers (v), resulting in higher ionic conductivity (Λ).

These theoretical frameworks are further supported by recent studies. Bao *et al*. have demonstrated that ionic conductivity increases with a higher fraction of SSIPs in the solvation structure[7]. In summary, free solvent molecules enhance ionic conductivity by decoupling Li^+-anion interactions, reducing cluster size, and increasing charge carrier mobility.

17. Where do the authors show the "rapid Li^+ transport kinetics between the Li anode and the electrolyte"?

Response: Thank you for the thoughtful question. The original statement "rapid Li^+ transport kinetics between the Li anode and the electrolyte" specifically refers to enhanced Li^+ mobility within the IHCE layer, rather than across the entire Li anode/electrolyte interface. To avoid potential overinterpretation, we have revised the manuscript (*Page 7, 8, lines 194-203*) to clarify this point and support it with experimental evidence.

Specifically, ionic conductivity measurements show that the IHCE layer exhibits a conductivity of ~1.1×10^{-3} S cm^{-1} (Fig. R2 and Table R1), which is significantly higher than that of conventional artificial protective layers (~10^{-5} to 10^{-4} S cm^{-1})[1,2]. Additionally, the IHCE achieves a Li^+ transference number (t_{Li^+} = 0.57) (Fig. 5d and Supplementary Fig. 27), outperforming SCE (0.33) and HCE (0.42), indicating reduced anion polarization and more efficient Li^+ migration. These results are further supported by Raman spectroscopy analysis (Supplementary Fig. 18), which reveals a substantial fraction of contact ion pairs (CIPs, 47.5%) and solvent-separated ion pairs (SSIPs, 37.6%), indicating a well-balanced solvation environment that facilitates both high t_{Li^+} and sufficient ionic conductivity. Taken together, the combination of a high t_{Li^+} and moderate ionic conductivity enables efficient Li^+ transport with IHCE layer, as originally stated.

18. Figure 4: What about lower current densities, frequently used in practical devices? Is the effect similar?

Response: We thank the reviewer for raising this important point. To address this, we conducted a detailed analysis of Li deposition behavior at a lower current density of 1 mA cm^{-2} (Figs. R11-12) and compared it with the previously reported results at a high current density of 4 mA cm^{-2} (Fig. 4 and Supplementary Fig. 20). Our findings confirm that IHCE@Cu maintains consistent suppression of Li dendrite growth and volume expansion at both low and high current densities, demonstrating its robustness under practical operating conditions.

At 1 mA cm^{-2}, the Li deposition in SCE exhibits loose, porous and rod-like structures (Fig. R11a) with a thickness of ~7.8 μm after 1 cycle. After 50 cycles, severe cracks and voids appear, leading to a substantial thickness increase to ~13.2 μm (~69.2% expansion, Fig. R11b-d). In HCE, the initial deposition morphology appears relatively compact (~5.4 μm thick, Fig. R12a, b), however, after continued cycling, the layer expands to ~7.9 μm, corresponding to a ~46.3% increase in thickness (Fig. R12c, d). In sharp contrast, IHCE@Cu enables compact and uniform Li deposition with minimal volume expansion, increasing only from ~5.1 μm to ~5.9 μm after 50 cycles (~15% expansion) (Fig. R11e-h). The initial deposited Li thickness (~5.1 μm) closely aligns with the theoretical value (~5 μm for 1 mAh cm^{-2}). Even after 50 cycles, the deposited Li layer remains highly compact, with only a slight thickness increase to ~5.9 μm (~15.7% expansion). These trends are consistent with the results at 4 mA cm^{-2}, where IHCE@Cu limits expansion to ~31.4% (5.1 → 6.7 μm, Fig. 4f, h), significantly lower than SCE (~67.5%) and HCE (~61.8%). These results demonstrate that IHCE maintains stable Li deposition across different current densities, effectively suppressing dendrite growth and mitigating volume expansion.

Updated in the revised Manuscript (Page 9, lines 225-231):

"This suppression of Li dendrite growth and volume expansion is also evident under a lower current density of 1 mA cm^{-2} (Supplementary Figs. 21, 22). In the SCE system, the deposited Li expands from ~7.8 μm to ~13.2 μm after 50 cycles, corresponding to a ~69.2% increase. In the HCE system, the thickness increases from ~5.4 μm to ~7.9 μm (~46.3% increase). In sharp contrast, IHCE@Cu maintains a compact morphology,

with only a slight thickness increase to from ~5.1 μm to ~5.9 μm (~15.7% increase).”

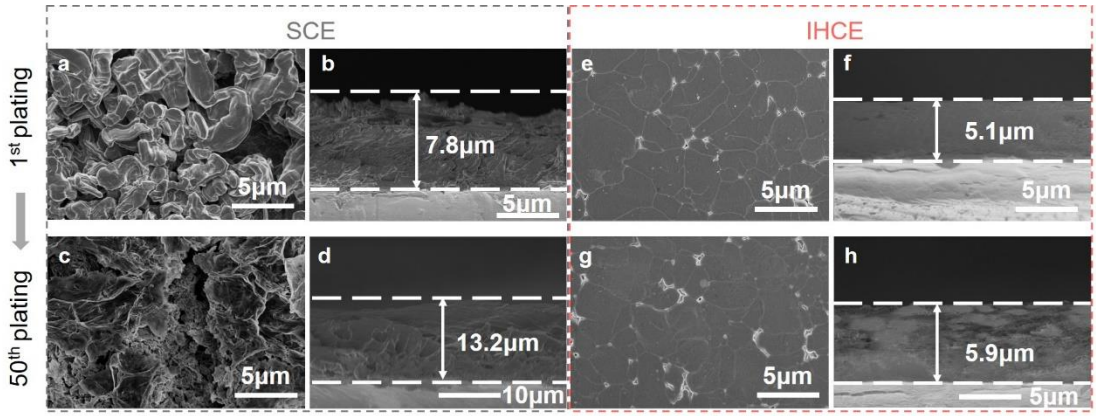

Fig. R11. The SEM images of deposited Li at a current density of 1 mA cm^{-2}. (a, c, e, g) Top view and (b, d, f, h) cross-sectional SEM images of deposited Li on bare Cu (a-d) and IHCE@Cu (e-h) in SCE after 1 cycle and 50 cycles.

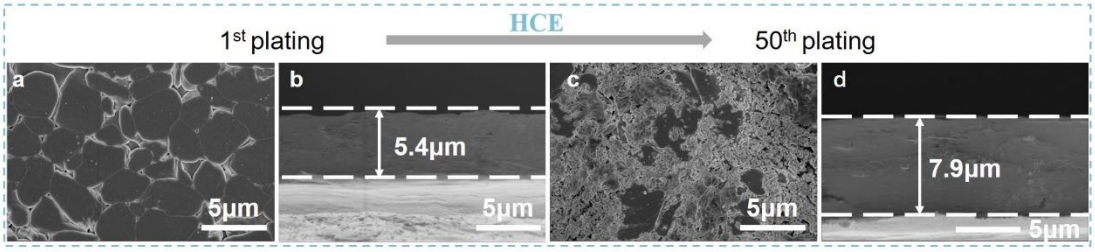

Fig. R12. The SEM images of deposited Li at a current density of 1 mA cm^{-2}. (a, c) Top view and (b, d) cross-sectional SEM images of deposited Li on bare Cu in HCE after 1 cycle (a-b) and 50 cycles (c-d).

19. Page 11, line 256: What do the authors refer to as “hysteretic Li^+ transport”?

Response: Thank you for your constructive suggestion. The term “hysteretic Li^+ transport” refers to the delayed response of Li^+ migration to the applied electric field, particularly under high current densities. This leads to a temporal mismatch between ion supply from the bulk electrolyte and Li^+ depletion at the anode surface. This phenomenon results in severe concentration polarization and interfacial instability, where the local Li^+ concentration at the electrode interface rapidly decreases. It can be quantitatively described by Sand’s Equation (20):

$$\tau = \pi D \left(\frac{eC_0}{2J}\right)\left(\frac{\mu_a + \mu_c}{\mu_a}\right) \quad (20)$$

Where “τ” is Sand’s time, the time required for Li^+ depletion at the anode surface to

reach zero, "D" is the Li^+ diffusion coefficient, "e" is the electronic charge, "C_0" is the initial concentration of the electrolyte, "J" is the applied current density, "μ_a" and "μ_c" are the mobilities of the anion and Li^+, respectively.

Under high current densities (J), Li^+ is rapidly consumed at the anode interface. However, due to the limited diffusion coefficient (D) and low initial Li^+ concentration (C_0), the transport of Li^+ from the bulk electrolyte cannot keep up with interfacial demand. As a result, the Li^+ concentration near the electrode surface drops to near zero before steady-state can be reached, as described by Sand's time (τ). The difference in mobilities between Li^+ (μ_c) and anions (μ_a) further contributes to this imbalance, delaying ionic response and intensifying concentration gradients[8].

20. Figure 5a: How come that the overpotential is lower at the same current density after the evaluation of varying current densities?

Response: Thank you for raising this insightful observation. The reduction in overpotential at the same current density after the evaluation of varying current densities in Figure 5a can be attributed to the electrochemical activation of the interface. To validate this, we performed EIS measurements on Li||Li symmetric cells before and after rate performance test (0.5 to 6 mA cm^{-2}), without returning to lower current densities. As shown in Fig. R13, all systems (SCE, HCE, and IHCE) exhibit a clear reduction in interfacial resistance after high-rate cycling, compared to their initial states. This indicates the gradual formation of a more stable and ion-conductive SEI layer during cycling, which directly reduces interfacial resistance and renders lower overpotential upon returning to the same current density. This phenomenon has been widely observed in lithium metal systems[9–11].

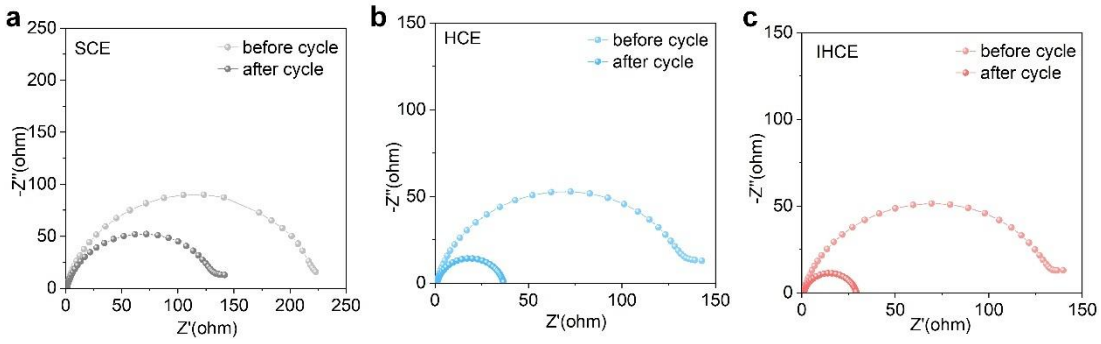

Fig. R13. Nyquist plots of Li||Li cells cycling in (a) SCE, (b) HCE and (c) IHCE before and after cycling (from 0.5 to 6 mA cm^{-2}).

21. How do the authors explain the differences concerning the Li^+ transference number and the (apparent) activation energy (that term would require further discussion and clarification for the given system, in fact)? This is not obvious.

Response: Thank you for highlighting this important point. The Li^+ transference number (t_{Li^+}) and activation energy (E_a) describe different aspects of ion transport and interface behavior. The t_{Li^+} is defined as the fraction of total ionic current carried by Li^+ and can be expressed as Equation (21):

$$t_{Li^+} = \frac{Q_{Li^+}}{Q_{Li^+} + Q_{anions}} = \frac{u_{Li^+}}{u_{Li^+} + u_{anions}} \quad (21)$$

Where Q and u represent the charge contribution and mobility of Li^+ and anions, respectively. The higher t_{Li^+} observed in IHCE (0.57) compared to HCE (0.42) and SCE (0.33) can be attributed to the reduced mobility of anions, which are partially immobilized within the polymer matrix. This anion-constraining effect increases the relative contribution of Li^+ to total ionic conduction.

The E_a discussed in the manuscript refers to the energy barriers for Li^+ migration through SEI. It is influenced by the structural and compositional characteristics of the SEI and is calculated using Equation (22):

$$\frac{T}{R_{SEI}} = Aexp\left(-\frac{E_a}{RT}\right) \quad (22)$$

where T is the absolute temperature, R is the gas constant, R_{SEI} is the SEI resistance, and A is the pre-exponential factor. The lower E_a of IHCE (54.3 kJ mol^{-1}) and HCE

(58.9 kJ mol^{-1}) compared to SCE (80.6 kJ mol^{-1}) is attributed to the formation of highly ion-conductive LiF-rich SEI layers, which facilitate Li^+ migration and reduce interfacial resistance.

22. Generally, the concentration gradient of the Li salt remains to be clearly proven.

Response: We sincerely thank the reviewer for this thoughtful comment. We fully agree that clearly demonstrating the presence of a lithium salt concentration gradient is crucial for validating the IHCE design. To directly visualize the LiTFSI concentration gradient between the IHCE layer and the adjacent standard-concentration electrolyte (SCE), we performed Raman mapping based on the characteristic S-N-S stretching vibration band of $TFSI^-$ (740-749 cm^{-1}). This vibrational mode is highly sensitive to salt coordination environment and concentration. Specifically, solid LiTFSI exhibits a peak at ~749 cm^{-1}, while 1 M LiTFSI-DME shows a peak near ~740 cm^{-1}. Therefore, this vibrational mode can serve as a reliable indicator of local LiTFSI concentration.

Due to the vertical configuration of our Raman spectrometer, the laser is fixed perpendicular to the sample stage and cannot be angled. As a result, the laser can only be directed vertically onto the sample from above. However, since the Raman signal is highly dependent on the position of the laser focal point, performing vertical depth profiling by scanning from the top SCE layer to the bottom IHCE@Cu interface may cause significant signal attenuation and increase the measurement errors. To address this limitation, we improved the experimental method. As illustrated in Fig. R14, the IHCE@Cu electrode and the SCE (1 M LiTFSI-DME) were assembled in a sealed in-situ Raman cell. Specifically, the IHCE@Cu sample was cut into a rectangular strip (14 mm × 4 mm) and affixed to the inner edge of a black O-ring (Fig. R14a), ensuring that both the IHCE layer and the adjacent SCE regions were aligned within the same focal plane. Next, SCE was injected into the blue region and allowed to naturally spread over the exposed IHCE@Cu surface via capillary action, simulating the realistic interfacial conditions. Finally, a transparent optical window (Ø = 22 mm) was placed over the assembly, followed by a metal cell lid secured with screws. During Raman mapping tests, the laser was focused on the IHCE surface and scanned laterally across the IHCE

layer to the SCE region (Fig. R14b). The resulting 2D Raman mapping image (Fig. R15), the signal intensity correlates with the characteristic $TFSI^-$ peak position, which is sensitive to local salt concentration. A distinct contrast in signal intensity is observed between the IHCE and SCE regions, providing direct evidence of a lithium salt concentration gradient extending from the IHCE toward the SCE.

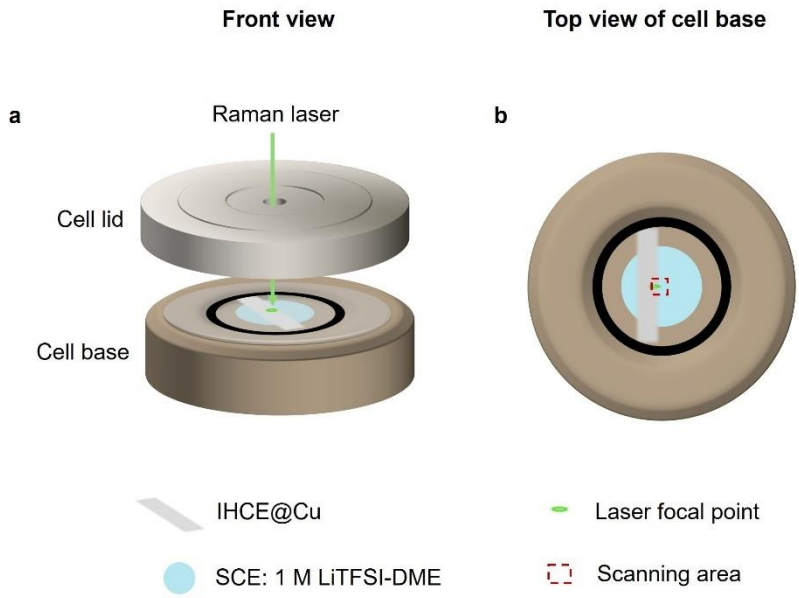

Fig. R14. Schematic diagram of the Raman spectroscopy measurement.

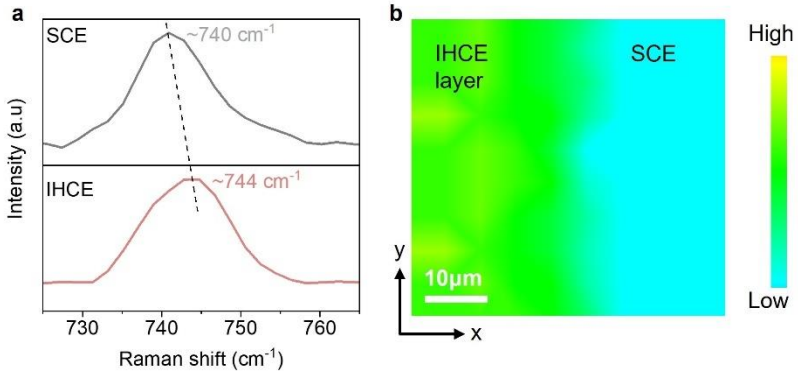

Fig. R15. a, Raman spectra of the SCE (1 M LiTFSI-DME) and IHCE (5 M LiTFSI-DME within a polymer matrix), respectively. b, 2D Raman mapping of IHCE, showing intensity distribution of the Raman band at 740-749 cm^{-1} from IHCE layer to SCE.

23. Besides, it appears that the choice of the separator for the two reference systems is not discussed in the main text, although this is an essential parameter.

Response: Thank you for pointing out this important detail. To ensure consistency and

fair comparison, we used same separator across all battery systems. Specifically, as stated in the Methods - Coin cell assembly (*Page 19, lines 511-512* in the Manuscript), we described: "All 2032-type coin cells were assembled with a wet single-sided ceramic polyethylene (PE) separator." Similarly, in the Methods - Fabrication of Li-metal pouch cell (*Page 19, lines 497-498* in the Manuscript), we described: "A wet single-sided ceramic polyethylene (16 μm, Shenzhen Numi Technology Co., Ltd) was used as the separator." For transparency, all supplier information for the electrode and cell components was updated in Supplementary Table 12.

24. 50 μm Li is not "ultra-thin". It's thin, but still far too thick for practical applications. In this regard, it's not clear why the authors increased the thickness to 100 μm for the larger cell to demonstrate the potential practical impact.

Response: We sincerely appreciate the reviewer's comment. Following your suggestion, the term "ultra-thin" has been corrected to "thin" in the revised Manuscript to ensure accuracy. Regarding the use of 100 μm Li foil in larger-format pouch cells, this choice was made to maintain consistency with the 50 μm Li foil used in coin cells when accounting for structural differences between the two formats (Fig. R16). In coin cells, a single-sided cathode is paired with a 50 μm Li foil. Differently, pouch cells are assembled as double-sided cathode → separator → Li foil (100 μm) → separator → double-sided cathode, where each Li foil serves as two cathodes. Thus, the effective Li thickness per cathode remains 50 μm, consistent with the coin cell setup. We agree that further reducing Li thickness (< 50 μm) is critical for maximizing the energy density in practical applications. In future work, we will explore the integration of thinner Li foils (e.g., 20-50 μm) into pouch cell configurations to further enhance the practical applicability of our IHCE strategy.

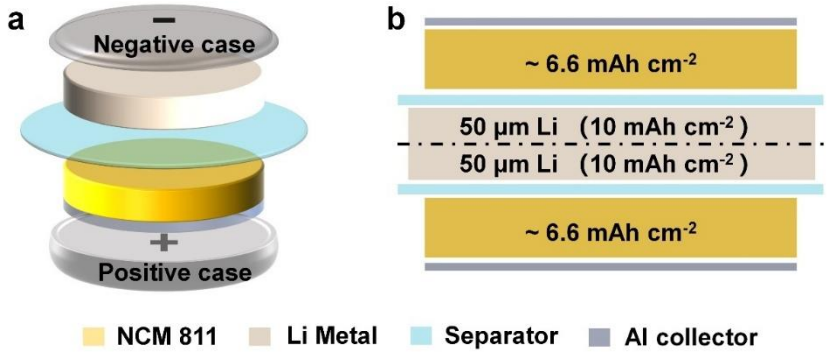

Fig. R16. Configurations of coin-type (a) and pouch-type cell (b).

25. How was the specific energy calculated? Which parts of the cell were considered?

Response: Thank you for your question. The specific energy was calculated using Equation (23):

$$Specific\ energy\ density\ (Wh\ kg^{-1}) = \frac{\text{Discharge capacity (Ah)} \times \text{Mid-value voltage (V)}}{\text{Total weight (kg)}} = \frac{6.8\ Ah \times 3.8\ V}{0.05104\ (kg)} = 506\ Wh\ kg^{-1} \quad (23)$$

In this work, the initial discharge capacity of 6.8 Ah was measured at 0.1 C. The total cell weight used for energy density calculation includes all battery parameters: cathode, anode (Li metal foil), electrolyte, separator, Al current collector, as well as cell package and lugs. The detailed parameters of the energy density calculation and the weight of each component in the pouch cell are provided in Tables R12, 13.

Table R12. The detailed parameters of the energy density calculation (0.1 C).

Discharge capacity (Ah)	Mid-value voltage (V)	Test condition (C)	Total weight (kg)	Energy density (Wh kg^{-1})
6.8	3.8	0.1	0.05104	506

Table R13. The weight of each component in the pouch cell.

Cathode (g)	Anode (g)	Electrolyte (g)	Separator (g)	Al foil (g)	Package and lugs (g)	Total weight (g)
33.26	3.57	8.77	1.6	1.74	2.10	51.04

26. The supplier information for the electrode and cell components appears to be missing.

Response: Thank you for your comment. To ensure transparency and reproducibility, we have provided detailed supplier information for all key materials, including the NCM811 cathode, Li foil, electrolyte, separator and Al foil. These details are now included in Table R14 and have also been incorporated into the revised Supplementary Table 12.

Table R14. The detailed supplier information for the electrode and cell components.

NCM811 cathode	Li foil	Electrolyte components	Separator	Al foil
Xian Safty Energy Technology Co., Ltd	China Energy Lithium Co., Ltd	Suzhou Dodo Chem Co., Ltd	Shenzhen Numi Technology Co., Ltd	Shenzhen Shuanghai Trading Co., Ltd.

Review #2 (Remarks to the Author):

Overall comment: This manuscript presents a simple approach to decouple the Li salt concentration between Li-electrolyte interface and electrolyte bulk by employing a polymeric membrane made of PVDF-HFE and CPEGDA, which confines a high-concentration of LiTFSI at the interface via hydrogen-bonding and ion-dipole interactions, as claimed by the authors. This approach seems interesting, since it can obtain the advantage of high-concentration electrolyte by forming LiF-rich SEI at the electrochemical interface, while maintaining low viscosity in the electrolyte bulk with a regular Li salt concentration of 1 M. Nevertheless, some important issues remain not addressed and answered in the current form of manuscript as listed below. Therefore, I don't recommend to publish on Nature Communications.

Response: We sincerely appreciate the reviewer's constructive feedback, which has helped us improve the clarity and rigor of our work. We acknowledge that the original manuscript lacked clarity in several key points. In response, we provide a detailed point-by-point response below.

1. Unclear lithium salt usage and cost implications:

A crucial issue is that the amount of Li salt used for a cell is not adequately clarified, which undermines the claim that this approach reduces cost. The authors argue that high concentration electrolyte is plagued by the high price and viscosity. However, in this work, since high concentration of LiTFSI must be pre-added into the polymeric membrane, the cost would be inevitably increased compared with 1 M electrolyte. The authors should give a clear and detailed description to evaluate the amount of salt used at each experiment step, to show what concentration of electrolyte it would correspond to for each cell. A direct comparison with a Li metal cell using only electrolyte (without the membrane) is essential. Furthermore, considering the cost of PVDF and CPEGDA, does this method truly offer a cost advantage? The manuscript would benefit from a thorough economic analysis.

Response: We thank the reviewer for raising this important point. We fully agree that a

thorough and transparent evaluation of lithium salt consumption and overall cost is critical to validating the cost-effectiveness of our proposed IHCE approach. To address this concern, we have now performed a comprehensive analysis of salt usage and materials cost at each experiment step. In particular, we performed calculations based on a practical 6.8 Ah Li||NCM811 pouch cell configuration specifically designed in this study (Supplementary Table 10), with an electrolyte-to-capacity (E/C) ratio of 1.29 g Ah^{-1}. All relevant parameters and discussion have been updated in Supplementary Note 10 and Supplementary Tables 13-16.

(1) Clarification of lithium salt usage in the IHCE layer.

The IHCE coating solution was applied at a unit usage of 2 μl cm^{-2}, corresponding to ~1.78 mg cm^{-2} (based on a density of ~0.889 g cm^{-3}). Accounting for the electrode dimensions (8.2 × 6.0 cm^2) and double-sided coating on the Li foil, the total usage of IHCE coating solution per Ah was calculated to be ~0.33 g Ah^{-1} (Equation (24)). In addition, the coating solution contains 0.2 wt% synthesized IHCE in a THF diluent, with 9.46 × 10^{-3} wt% LiTFSI (Equation (25)). Therefore, the IHCE layer contributes only 3.16 × 10^{-5} g Ah^{-1} of lithium salt (Equation (26)), which is negligible compared to the total salt used in the electrolyte system.

$$m_{IHCE\ coating\ solution} = 2 \times L \times W \times N \times Unit - usage \div 6.8 = 2 \times 8.2 \times 6 \times 13 \times 1.78 \div 1000 \div 6.8 = 0.33\ g\ Ah^{-1} \quad (24)$$

$$\omega_{\text{LiTFSI in IHCE coating solution}} = \frac{m_{LiTFSI\ in\ sythesized\ IHCE}}{m_{sythesized\ IHCE}} \times \frac{m_{sythesized\ IHCE}}{m_{IHCE\ coating\ solution}} = \frac{0.46}{9.73} \times 0.2\% = 9.46 \times 10^{-3}\% \quad (25)$$

$$m_{LiTFSI\ in\ IHCE\ layer} = m_{IHCE\ coating\ solution} \times \omega_{\text{LiTFSI in IHCE coating solution}} = 0.33 \times 9.46 \times 10^{-3}\% = 3.16 \times 10^{-5}\ g\ Ah^{-1} \quad (26)$$

Where "ω" represents the mass ratio, "m" refers to mass, and "L, W, N" represent length, width, and number of Li foils.

(2) Total lithium salt consumption comparison.

The IHCE system combines a standard-concentration bulk electrolyte (SCE) with an

IHCE coating layer. For comparison, systems using only bulk electrolytes (SCE and HCE) without a membrane were also evaluated.

The formulations used for HCE and SCE were 3 M LiDFOB + 2 M $LiBF_4$ and 0.6 M LiDFOB + 0.4 M $LiBF_4$ in FEC/DEC (1: 2, v/v), respectively. Based on Equations (27)-(30) and the detailed parameters listed in Tables R17, 18, the total lithium salt consumption per Ah was determined as: ~0.126 g Ah^{-1} for SCE, ~0.425 g Ah^{-1} for HCE, and ~0.126 g Ah^{-1} for IHCE system (SCE + IHCE layer). These results demonstrate that IHCE design reduces lithium salt usage by ~70.4 % compared to HCE, while maintaining nearly identical salt consumption to SCE (only ~0.025% increase), despite incorporating a highly salt-concentrated interfacial layer.

$$\omega_{LiDFOB\ (LiBF_4)} = \frac{m_{LiDFOB\ (LiBF_4)}}{m_{LiDFOB} + m_{LiBF_4} + m_{FEC} + m_{DEC}} \times 100\% \quad (27)$$

$$m_{LiDFOB\ (LiBF_4)} = C_{LiDFOB\ (LiBF_4)} \times V_{FEC+DEC} \times M_{LiDFOB\ (LiBF_4)} \quad (28)$$

$$m_{FEC\ (DEC)} = \rho_{FEC\ (DEC)} \times V_{FEC\ (DEC)} \quad (29)$$

$$m_{lithium\ salt} = m_{LiDFOB} + m_{LiBF_4} \quad (30)$$

Where "ω" represents the percentage of lithium salt relative to the total mass of the electrolyte; "m" refers to mass; "C" represents the concentration of lithium salt in electrolyte; "V" refers to volume; "ρ" represents densities of the electrolyte solvents.

(3) Cost analysis.

We performed a cost analysis considering all components used in the IHCE system, including PVDF-HFP, CPEGDA, LiTFSI and bulk electrolyte. Unit prices were obtained from commercial suppliers, as detailed in the Methods section and Supplementary Tables 12, 13 and 16. Based on Equations (31)-(33) and the parameters summarized in Tables R15-18, the calculated costs for SCE, HCE and IHCE were ~1.25 \$ Ah^{-1}, ~1.65 \$ Ah^{-1}, and ~1.28 \$ Ah^{-1}, respectively. These findings demonstrate that IHCE reduces cost by ~22.4% compared to HCE, while introducing only ~2.16% additional cost relative to SCE, primarily attributed to the polymer coating. These

results quantitatively confirmed the cost-effectiveness and practical scalability of the IHCE approach.

$$\begin{aligned} Cost\ \ of\ \ SCE &= P_{LiDFOB} \times m_{LiDFOB} + P_{LiBF_4} \times m_{LiBF_4} \\ &+P_{FEC} \times m_{FEC} + P_{DEC} \times m_{DEC} \\ &= 2.18 \times 0.09 + 2.18 \times 0.04 + 1.42 \times 0.49 + 0.41 \times 0.67 \\ &= 1.25\ \ \$\ \ Ah^{-1} \end{aligned} \tag{31}$$

$$\begin{aligned} Cost\ \ of\ \ HCE &= P_{LiDFOB} \times m_{LiDFOB} + P_{LiBF_4} \times m_{LiBF_4} \\ &+P_{FEC} \times m_{FEC} + P_{DEC} \times m_{DEC} \\ &= 2.18 \times 0.33 + 2.18 \times 0.1 + 1.42 \times 0.37 + 0.41 \times 0.49 \\ &= 1.65\ \ \$\ \ Ah^{-1} \end{aligned} \tag{32}$$

$$\begin{aligned} Cost\ \ of\ \ IHCE &= cost\ \ of\ \ IHCE\ \ membrane + cost\ \ of\ \ SCE \\ &= P_{IHCE\ \ coating\ \ solution} \times \frac{m_{IHCE\ \ coating\ \ solution}}{6.8} + 1.25 \\ &= 0.027 + 1.25 \\ &= 1.28\ \ \$\ \ Ah^{-1} \end{aligned} \tag{33}$$

Where "*p*" represents the unit-price of the specific electrolyte component, "*m*" is the mass.

Table R15. Raw materials usage and cost for IHCE synthesis.

Component	PVDF-HFP	LiTFSI	PEGDA	4-SH	AIBN	DMF
Mass (g)	0.74	0.46	0.15	0.035	0.0018	8.34
Density (g cm^{-3})	-	-	1.12	1.288	-	0.948
Unit-price ($ g^{-1})	1.35	2.18	0.13	0.24	1.09	0.10
Cost ($)	1.00	1.00	0.02	0.01	1.4×10^{-3}	0.82
Synthesized IHCE	Total mass (g)		9.73			
	Total cost ($)		2.86			
	Unit-price ($ g^{-1})		0.29			

Table R16. Usage and cost breakdown of the IHCE coating solution.

Component	Synthesized IHCE	THF	IHCE coating solution
Mass ratio	1	500	501
Density (g cm^{-3})	-	0.889	~0.889
Unit-price ($ g^{-1})	0.29	0.08	0.08
LiTFSI content in IHCE coating solution (%)			9.46×10^{-3}

Table R17. IHCE coating solution usage and cost for a 6.8 Ah pouch cell.

Li anode parameters			IHCE coating solution parameters				
Length (cm)	Width (cm)	Number	Unit-price ($ g^{-1})	Total usage (g)	Unit-usage (g Ah^{-1})	Total cost ($)	Unit cost ($ Ah^{-1})
8.2	6	13	0.08	2.27	0.33	0.18	0.027

Table R18. Lithium salt usage and cost per Ah for 6.8 Ah Li||NCM811 pouch cells using SCE, HCE and IHCE with an E/C ratio of 1.29 g Ah^{-1}.

Electrolytes		LiDFOB	$LiBF_4$	FEC	DEC
Unit-price ($ g^{-1})		2.18	2.18	1.42	0.41
SCE	Formula	0.6 M	0.4 M	1: 2, v/v	
	Usage (g Ah^{-1})	0.088	0.038	0.49	0.67
	Cost ($ Ah^{-1})	0.19	0.08	0.71	0.27
HCE	Formula	0.6 M	0.4 M	1: 2, v/v	
	Usage (g Ah^{-1})	0.33	0.095	0.37	0.49
	Cost ($ Ah^{-1})	0.72	0.21	0.52	0.20
IHCE coating solution	Unit-cost ($ Ah^{-1})	Ratio of LiTFSI (%)	Unit-usage (g Ah^{-1})	LiTFSI usage (g Ah^{-1})	LiTFSI cost ($ Ah^{-1})
	0.027	9.46×10^{-3}	0.33	3.16×10^{-5}	6.88×10^{-5}

Summary		SCE	HCE	IHCE
	Salt usage (g Ah^{-1})	0.126	0.425	0.12603
	Salt cost ($ Ah^{-1})	0.27	0.93	0.27007
	Total cost ($ Ah^{-1})	1.25	1.65	1.28

2. Use of fluorinated materials:

The manuscript criticizes LHCEs for their use of toxic fluorinated ethers, claiming these are not environmentally friendly. However, this work also employs PVDF-HFE, a highly fluorinated material. Moreover, the total lithium salt usage in this study appears comparable to that in LHCEs (e.g., LiFSI-DME-TTE at a 1: 1.2: 3 molar ratio). Additionally, preparing this membrane is neither time- nor cost-efficient compared to the straightforward preparation of LHCE. The authors should clarify the pronounced advantages of this approach over LHCEs.

Response: Thank you for your insightful comments. We appreciate the opportunity to

clarify the advantages of our IHCE strategy over traditional LHCEs, particularly in terms of environmental impact, lithium salt consumption, and cost-effectiveness. Our key points are outlined below:

(1) Environmental considerations:

Although both LHCE and IHCE systems incorporate fluorinated components, their environmental impact differs significantly. LHCEs rely on volatile perfluorinated ether solvents such as TTE, which are prone to evaporation and leakage, raising concerns over long-term ecological safety. In contrast, the fluorinated content in IHCE arises from PVDF-HFP, a solid, non-volatile polymer, which poses no evaporation risk. To quantify this difference, we calculated the F content in PVDF-HFP ($C_5H_2F_8$) and TTE ($C_5H_4F_8O$), based on their actual usage in a 1 Ah Li||NCM811 pouch cell. Using the design parameters from our 6.8 Ah cell and an E/C ratio of 1.29 g Ah^{-1} (Supplementary Table 10), we found that TTE in LHCE (LiFSI-DME-TTE at a 1: 1.2: 3 molar ratio) contributes to F content of ~0.58 g Ah^{-1}, whereas PVDF-HFP in IHCE membrane contributes to F content of only ~3.56×10^{-5} g Ah^{-1}. This represents a >99.99% reduction in F content in the IHCE system (Table R19). Thus, our approach is much more aligned with global green manufacturing principles and low-F strategies. Detailed calculation was performed using Equations (34)-(41), with all parameters provided in Table R19.

Calculation of atomic percentage of F in TTE and PVDF-HFP, respectively：

$$F_{TTE}\% = \frac{8 \times M_F}{5 \times M_C + 4 \times M_H + 8 \times M_F + M_O} = \frac{8 \times 19}{5 \times 12 + 4 \times 1 + 8 \times 19 + 16} \times 100\% = 65.5\% \quad (34)$$

$$F_{PVDF-HFP}\% = \frac{8 \times M_F}{5 \times M_C + 2 \times M_H + 8 \times M_F} = \frac{8 \times 19}{5 \times 12 + 2 \times 1 + 8 \times 19} \times 100\% = 71\% \quad (35)$$

Calculation of mass percentage of fluorinated component LHCE (TTE) and IHCE

(PVDF-HFP), respectively：

$$TTE_{LHCE}\% = \frac{n_{TTE} \times M_{TTE}}{n_{LiFSI} \times M_{LiFSI} + n_{DME} \times M_{DME} + n_{TTE} \times M_{TTE}} \times 100\% = \frac{3 \times 200.05}{1 \times 187.07 + 1.2 \times 90.12 + 3 \times 200.05} \times 100\% = 67.03\% \quad (36)$$

$$PVDF - HFP_{IHCE}\% = \frac{m_{LiTFSI\ in\ sythesized\ IHCE}}{m_{sythesized\ IHCE}} \times \frac{m_{sythesized\ IHCE}}{m_{IHCE\ coating\ solution}} \times 100\% = \frac{0.74}{9.73} \times \frac{1}{501} \times 100\% = 1.52 \times 10^{-2}\% \quad (37)$$

Calculation of TTE and PVDF-HFP usage in a 1 Ah Li||NCM811 pouch cell:

The F component consumption in a 1 Ah Li||NCM811 pouch cell was estimated based on the design parameters of our 6.8 Ah pouch cell (Supplementary Table 10), using E/C ratio = 1.29 g Ah^{-1}. The usage of IHCE coating solution was ~0.33 g Ah^{-1} (Equation (24)):

$$m_{TTE} = 1.29 \times TTE_{LHCE}\% = 0.86\ g\ Ah^{-1} \quad (38)$$

$$m_{PVDF-HFP} = m_{IHCE\ coating\ solution} \times PVDF - HFP_{IHCE}\% = 0.33 \times 1.52 \times 10^{-2}\% = 5.02 \times 10^{-5}\ g\ Ah^{-1} \quad (39)$$

Calculation of F atomic mass percentage in LHCE and IHCE, respectively:

$$m_{F\ in\ LHCE} = m_{TTE} \times TTE_{LHCE}\% = 0.86 \times 67.03\% = 0.58\ g\ Ah^{-1} \quad (40)$$

$$m_{F\ in\ IHCE} = m_{PVDF-HFP} \times F_{PVDF-HFP}\% = 5.02 \times 10^{-5} \times 71\% = 3.56 \times 10^{-5}\ g\ Ah^{-1} \quad (41)$$

Where "*m*" represents mass. "*M*" represents molecular mass. "*n*" represents "molar ratio".

Table R19. Comparison of fluorine content in 1 Ah Li||NCM811 pouch cell with an E/C ratio of 1.29 g Ah^{-1}.

Parameter	IHCE (This Work)	LHCE (LiFSI-DME-TTE (1:1.2:3, molar ratio))
Fluorinated Material	PVDF-HFP	TTE
Ratio of F atom in PVDF-HFP or TTE (%)	71	65.5
Ratio of fluorinated Material	1.52×10^{-4}	0.67
Usage of fluorinated Material (g Ah^{-1})	5.02×10^{-5}	0.86
F content (g Ah^{-1})	3.56×10^{-5}	0.58

(2) Lithium salt usage.

A key limitation of LHCEs is the need to sustain a localized high salt concentration throughout the bulk electrolyte, which results in excessive salt consumption. For example, the LHCE (LiFSI-DME-TTE at a 1: 1.2: 3 molar ratio) consumes lithium salt with ~0.27 g Ah^{-1}. In contrast, IHCE confines the high-concentration electrolyte only at the electrode interface, while the bulk electrolyte remains at 1 M. As a result, the total lithium salt consumption in IHCE is reduced to ~0.13 g Ah^{-1}, representing a ~51.9% decrease compared to the LHCE. This reduction in salt usage also translates to a significant cost advantage, lowering the electrolyte cost from ~1.85 \$ Ah^{-1} in the LHCE to ~1.28 \$ Ah^{-1} in the IHCE, corresponding to a ~30.8% decrease. These findings demonstrate that IHCE retains the ion-transport and interfacial stabilization benefits of LHCEs while substantially reducing lithium salt consumption. The specific calculations are based on Equations (42)-(44), with detailed parameters provided in Table R20.

$$\omega_{a,b,c} = \frac{n_{a,b,c} \times M_{a,b,c}}{\sum_{a}^{c} n \times M} \times 100\% \quad (42)$$

$$m_{a,b,c} = \omega_{a,b,c} \times 1.29 \ \ g \ \ Ah^{-1} \quad (43)$$

$$Cost \ \ of IHCE = \sum_{a}^{c} \omega \times m \times P \quad (44)$$

Where "*n*" represents molar ratio. "*M*" represents molar mass. "*ω*" and "*P*" represent the mass ratio and unit-price of each electrolyte components, respectively. "*a*, *b*, *c*" represents LiFSI, DME and TTE, respectively.

Table R20. Lithium salt usage and cost of 1 Ah Li||NCM811 pouch cells using LHCE and IHCE with an E/C ratio of 1.29 g Ah^{-1}

Electrolytes		LiFSI	DME	TTE
1.29 g LHCE	Formula (molar ratio)	1.00	1.20	3.00
	Unit-price ($ g^{-1})	2.18	2.18	1.42
	Usage (g)	0.27	0.16	0.86
	Cost ($)	0.59	0.08	1.18
Summary		LHCE		IHCE
	Salt usage (g Ah^{-1})	0.27		0.13
	Cost ($ Ah^{-1})	1.85		1.28

(3) Scalability and cost-effectiveness.

While IHCE fabrication involves a polymer matrix preparation step, the overall process remains simple and scalable. The polymer matrix is synthesized via a "click chemistry reaction", which is known for its high efficiency, selectivity, and operational simplicity. After synthesis, the polymer is applied through a straightforward solution-coating process. This coating process is fully compatible with roll-to-roll manufacturing techniques already used in commercial electrode fabrication. In terms of cost, although IHCE includes additional polymeric components, our quantitative analysis shows that it significantly reduces the overall consumption of lithium salt and fluorinated solvents - two major cost drivers in LHCE systems. As detailed in Table R20, the electrolyte-related cost per Ah for IHCE-based pouch cells is reduced by ~30.8% compared to LHCE-based counterparts. This is primarily due to using a standard 1 M electrolyte in the bulk and the strategic localization of the salt-rich phase to the interfacial region only. Additionally, the IHCE serves as an interfacial protection layer,

which is expected to integrate into various conventional cell architectures. The IHCE-based Li||NCM811 pouch cells in our study exhibit excellent cycling performance, retaining 75.8% of their initial capacity after 200 cycles at 0.5 C with a high energy density of 506 Wh kg^{-1} (Fig. 6f). In contrast, state-of-the-art LHCE-based pouch cells typically show lower cycle life (<175 cycles), as summarized in recent publications (Table R21). This long-term cycling stability enabled by IHCE reduces degradation-related costs and underscores its practical potential for scalable and sustainable lithium metal battery applications.

Table R21. Comparison of pouch-type LMBs in this work and reported LHCE-based systems.

Energy density (Wh kg^{-1})	Cathode loading (mAh cm^{-2})	N/P ratio	E/C (g Ah^{-1})	Cycle life	Refs.
506	6.6	1.5	1.29	200 cycles	This work
505.9	4.2	1.5	1.25	130 cycles	Nat. Energy, 2024, 9, 987.
472	5.2	2.0	1.2	150 cycles	Adv. Mater. 2023, 35, 2301171
440.0	5.6	1.8	2.1	140 cycles	Nat. Energy, 2023, 8, 725.
430	5.6	1.8	2.04	173 cycles	Angew. Chem. Int. Ed. 2023, 135, e202306889.

3. Unclear confinement effect:

Throughout the manuscript, I did not see convincing experimental results as to why the synthesized membrane can confine the Li salt. However, this is a key part for this work.

Response: We sincerely appreciate the reviewer's critical feedback regarding the salt confinement mechanism in our IHCE membrane. This is indeed a central part of our work. To address this, we have reinforced our explanation by incorporating both updated MD simulations and experimental evidence, which collectively demonstrate that the salt-retention behavior arises from a synergistic combination of sub-nanometer confinement and molecular interactions.

(1) Physical confinement.

The primary mechanism responsible for long-term salt retention is the sub-nanometer

confinement imposed by the bicontinuous polymer matrix. To clarify this point, we conducted new MD simulations to investigate the physical structure of IHCE. Specifically, we compared the following three systems: (i) polymer blends: PVDF-HFP/CPEGDA, (ii) polymer blends + solvent: PVDF-HFP/CPEGDA-DME, and (iii) IHCE system: PVDF-HFP/CPEGDA-DME-LiTFSI. As shown in Fig. R17, the inclusion of DME leads to the free volume in PVDF-HFP+CPEGDA matrix increasing from 7275.04 $Å^3$ to 10319.41 $Å^3$, reflecting an expanded polymer network and enhanced segmental motion. Upon LiTFSI incorporation, the free volume decreased to 9530.56 $Å^3$, indicating partial occupation of internal cavities by $TFSI^-$ anions. Notably, pore size distribution analysis reveals that in the IHCE system, the dominant pore diameters are below 2.5 Å, significantly smaller than the solvated diameter of $TFSI^-$ (>9 Å). This confirms that the polymer matrix imposes strong spatial restrictions on solvated $TFSI^-$.

Furthermore, the diffusion coefficient of $TFSI^-$ in the IHCE membrane was calculated to be 0.04×10^{-2} Å ps^{-1}, in stark contrast to 2.47×10^{-2} Å ps^{-1} in bulk 1 M LiTFSI-DME electrolyte (SCE) (Fig. R18). This ~98.4% reduction in $TFSI^-$ mobility directly validates the effectiveness of sub-nanometer scale confinement in suppressing salt diffusion.

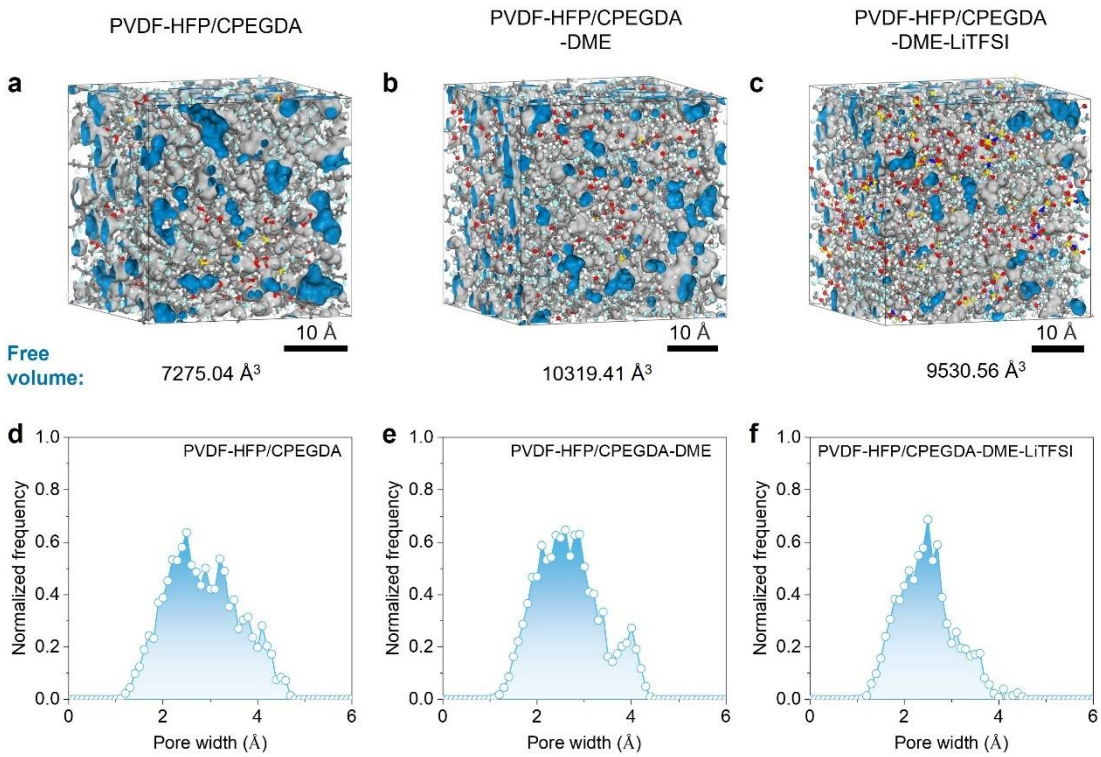

Fig. R17. a-c, Three-dimensional view of fractional free volume models of PVDF-HFP/CPEGDA polymer blends (a), PVDF-HFP/CPEGDA-DME (b), PVDF-HFP/CPEGDA-DME-LiTFSI (c, IHCE) by molecular simulations. The grey surface indicates the van der Waals surface, and the blue surface is the Connolly surface with a probe radius of 1.3 Å. d-f, Normalized pore size distribution derived from molecular simulation as shown in (a-c).

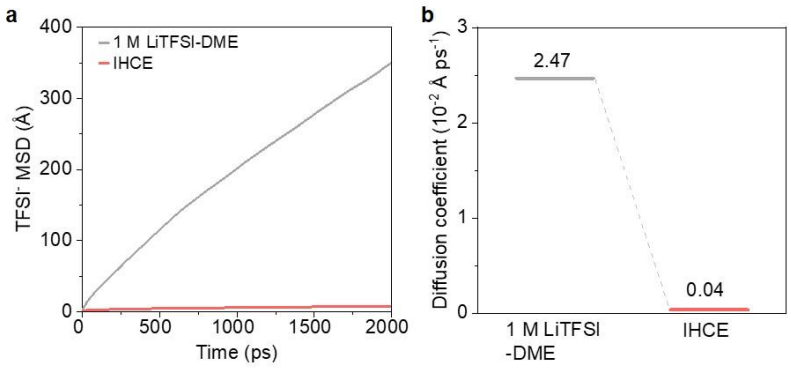

Fig. R18. Calculated MSD as a function of the simulation time (a) and diffusion coefficients of $TFSI^-$ (b) in SCE (1 M LiTFSI-DME) electrolyte and IHCE layer.

(2) Anion anchoring with molecular interactions

In addition to physical confinement, hydrogen bonding and ion-dipole interactions further assist in $TFSI^-$ immobilization. FTIR analysis (Fig. 3f) shows redshifts in the -CF_2 (PVDF-HFP) vibrational bands from 1063 and 1147 cm^{-1} to 1056 and 1133 cm^{-1}

upon DME and $TFSI^-$ addition, indicating the formation of H···F interactions among PVDF-HFP, DME, and $TFSI^-$. ^1H NMR spectra (Fig. 3g) reveal downfield shifts of DME from PVDF-HFP-DME-$TFSI^-$ (3.48 and 3.51 ppm) to PVDF-HFP-DME (3.30 and 3.33 ppm), reflecting the formation of H···O and H···F interactions among DME, $TFSI^-$ and PVDF-HFP.

DFT calculations further quantify these interactions, revealing that $TFSI^-$ binds more strongly to PVDF-HFP (-15.03 kcal mol^{-1}) and CPEGDA (-10.22 kcal mol^{-1}) than to DME (-7.91 kcal mol^{-1}). When DME is present, ternary complexes such as PVDF-HFP-DME-$TFSI^-$ and CPEGDA-DME-$TFSI^-$ show even stronger binding energies (-19.26 and -22.60 kcal mol^{-1}, respectively), suggesting that DME acts as a coordination bridge between the polymer and the anion. This is further supported by electrostatic potential (ESP) analysis (Fig. R19), which shown that DME in PVDF-HFP-DME and CPEGDA-DME complexes displays higher local ESP maximum (+15.3 and +10.4 kcal mol^{-1}) and less negative ESP minimum (-31.7 and -25.6 kcal mol^{-1}) compared to pure DME (+12.4 and -42.1 kcal mol^{-1}). This redistribution of electron density enhances the electrostatic affinity of DME toward $TFSI^-$ within the polymer matrix, further contributing to its immobilization.

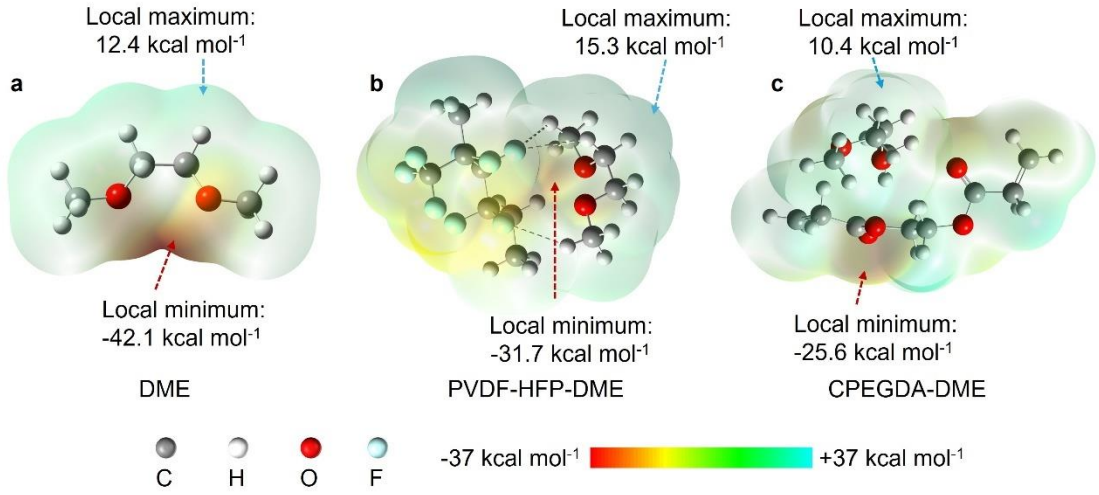

Fig. R19. The electrostatic potential (ESP) variations of DME (a) upon coordination with PVDF-HFP (b) or CPEGDA (c).

In summary, while hydrogen bonding and ion-dipolar interactions contribute to local

anchoring of $TFSI^-$, it is the spatial confinement provided by the polymer matrix that primarily governs long-term salt retention. The synergistic effect of structural restriction and molecular interactions enables the IHCE membrane to effectively immobilize LiTFSI under both static and operational conditions.

To clarify these points, we have made corresponding revisions to the revised Manuscript (*Pages 6, 7*) and updated the relevant content in Fig. 3 and Supplementary Figs. 12-17.

Table R22. Binding energies of $TFSI^-$ with various systems.

System	Binding energy (kcal mol^{-1})
DME-$TFSI^-$	-7.91
PVDF-HFP-$TFSI^-$	-15.03
CPEGDA-$TFSI^-$	-10.22
PVDF-HFP -DME-$TFSI^-$	-19.26
CPEGDA-DME-$TFSI^-$	-22.60

4. Mechanism extensibility:

The manuscript attributes the confinement effect to the hydrogen-bonding and ion-dipole interactions. How about the extensibility of this approach? I wonder if other materials with these microscopic forces can achieve a similar function or not.

Response: We thank the reviewer for raising this important question. While hydrogen bonding and ion-dipole interactions are critical for $TFSI^-$ immobilization. Our study shows that durable salt retention arises not only from molecular interactions, but also from their synergy with spatial confinement, as elaborated in our response to Comment 3.

To evaluate whether hydrogen bonding and ion-dipole interactions alone are sufficient to achieve similar confinement, we synthesized a comparative polymer (PFO) rich in fluorinated and ether segments but lacking the sub-nanometer-confined microstructure. The membrane was prepared via free-radical copolymerization of

perfluorohexylethyl acrylate (PFHEA) and polyethylene glycol diacrylate (PEGDA). The PFHEA-to-PEGDA monomer ratio was adjusted to yield a polymer membrane with a DME uptake of ~30 wt%, matching that of the IHCE membrane. The LiTFSI content was fixed at 50 wt% relative to total polymer mass to maintain comparable salt loading. AIBN initiator was added at 1 wt% of total monomer mass, and the polymerization was carried out at 65 °C for 12 h to ensure complete reaction. After polymerization, the resulting membrane was dried under vacuum to remove residual solvent and form a free-standing film. Using the same salt-retention testing protocol employed for IHCE, the membrane was soaked in DME, and the LiTFSI concentration was monitored over time. The mass of each PFO membrane was ~46 mg. After soaking in DME, the concentration of dissolved LiTFSI was quantified via UV absorbance and calculated using Equations (45), (46). The residual LiTFSI content remaining in the membranes was determined using Equation (47), with results summarized in Table R23. We found that the residual LiTFSI concentration in the PFO membrane dropped sharply from 3.5 M (after 2 days) to 2.0 M (after 5 days), and further to 1.2 M (after 10 days) (Fig. R20). These results suggest that hydrogen bonding and dipole interactions alone are insufficient to maintain salt confinement and the essential role of sub-nanometer-confined microstructure in achieving durable salt retention.

Standard curve equation:

$$y = 0.5253 \times x + 0.1325 \tag{45}$$

$$m_{dissolved\ LiTFSI} = x \times V_{DME} = \frac{y - 0.1325}{0.5253} \times 3 \tag{46}$$

$$\begin{aligned} C_{residual\ LiTFSI\ in\ IHCE} &= \frac{m_{residual\ LiTFSI\ in\ IHCE}}{M_{LiTFSI} \times V_{solvent\ uptake\ of\ IHCE}} \\ &= \frac{m_{LiTFSI\ in\ dry-IHCE} - m_{disssolved\ LiTFSI}}{287.09 \times \frac{m_{polymer\ in\ dry-IHCE} \times 30\%}{\rho_{DME}} \times 10^{-3}} \\ &= \frac{\left(m_{dry-IHCE} \times 0.332\right) - \left(\frac{y - 0.1325}{0.5253} \times 3\right)}{287.09 \times \frac{m_{dry-IHCE} \times 0.668 \times 30\%}{0.867} \times 10^{-3}} \end{aligned} \tag{47}$$

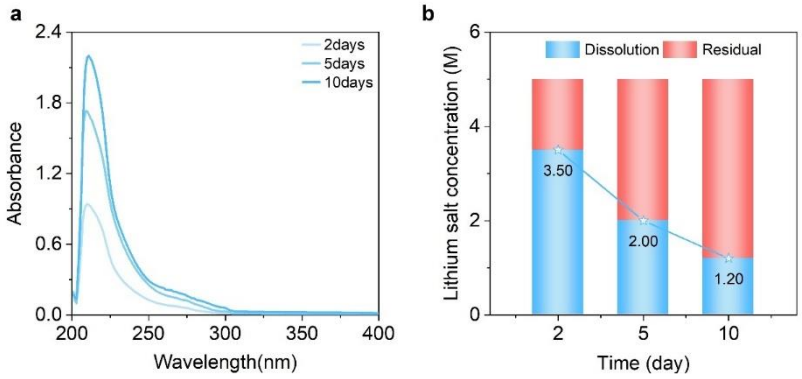

Fig. R20. a, Quantitative monitoring of LiTFSI dissolution concentration of PFO in the DME immersion solution via ultraviolet-visible (UV-Vis) measurements over various days. b, Dissolution and residual concentration profiles of LiTFSI in PFO versus immersion time.

Table R23. Parameters of UV experiments.

Time (day)	UV absorbance (y)	LiTFSI in DME		Residual LiTFSI in PFO	
		Concentration (x, mg ml^{-1})	Mass (mg)	Mass (mg)	Concentration (M)
2	0.942	1.541	4.623	10.743	3.5
5	1.732	3.045	9.135	6.078	2.0
10	2.201	3.936	11.808	3.730	1.2

5. Electrochemical stability:

The electrochemical stability of this membrane is questionable. Since the membrane contains plentiful C=O bonds, which are known to be extremely unstable towards Li metal. This raises concerns about whether the membrane would decompose during cell cycling. If so, can it maintain the function and still confine Li salt after long-term cycling? Experimental evidence addressing this concern is crucial.

Response: Thank you for raising this important concern. We agree that carbonyl (C=O) groups in CPEGDA may exhibit reactivity toward Li metal, which could potentially affect the electrochemical stability of the IHCE membrane. However, this reactivity is expected to be localized at the interfacial region in direct contact with Li metal, and does not compromise the stability or salt-retention function of the bulk IHCE membrane. To directly investigate this, we conducted a post-cycling interfacial stability test using free-standing IHCE membranes. Unlike the configuration where IHCE is coated on Cu,

this setup allowed direct contact between the IHCE and Li, enabling us to isolate and observe any chemical changes occurring specifically at the interface between IHCE and Li metal anode.

Specifically, we prepared self-supporting IHCE membranes and placed them in direct contact with Li metal, followed by the assembly of Li||Cu half cells. These cells were cycled under 1 mA cm^{-2} with a deposition capacity of 1 mAh cm^{-2} for 50 cycles. After cycling, the membranes were disassembled in an argon-filled glovebox, rinsed with anhydrous DME to remove residual salt, vacuum dried, and then subjected to XPS depth profiling. Importantly, the XPS measurements were performed on the membrane surface that had direct contact with Li, enabling accurate assessment of interfacial decomposition.

As shown in Fig. R21, the surface of the cycled IHCE membrane exhibits a slight decrease in the -C=O signal (~288.3 eV) compared to the pristine membrane, suggesting some surface-level decomposition of CPEGDA. However, after 30 s of Ar^+ sputtering, the C 1s spectra of the cycled membrane closely resemble that of the pristine one, with nearly unchanged intensities of both -C=O and -C-O peaks. This indicates that electrochemical reaction is confined to the surface, while the bulk membrane remains chemically intact. Moreover, the characteristic PVDF-HFP peaks at ~292.9 eV ($-CF_3$) and ~290.4 eV ($-CF_2$) remain unchanged after cycling, confirming the mechanical and chemical robustness of the fluorinated backbone. In parallel, the Li 1s spectra provide further insight into salt retention. The LiTFSI peak at ~55.8 eV remains clearly visible after cycling, with only a slight surface intensity reduction, while the signal after sputtering is nearly identical to that of the uncycled membrane. These results suggest that, despite minor reaction of C=O groups at the Li interface, the IHCE membrane retains its electrochemical stability, and the LiTFSI remains effectively confined within the polymer matrix during prolonged cycling.

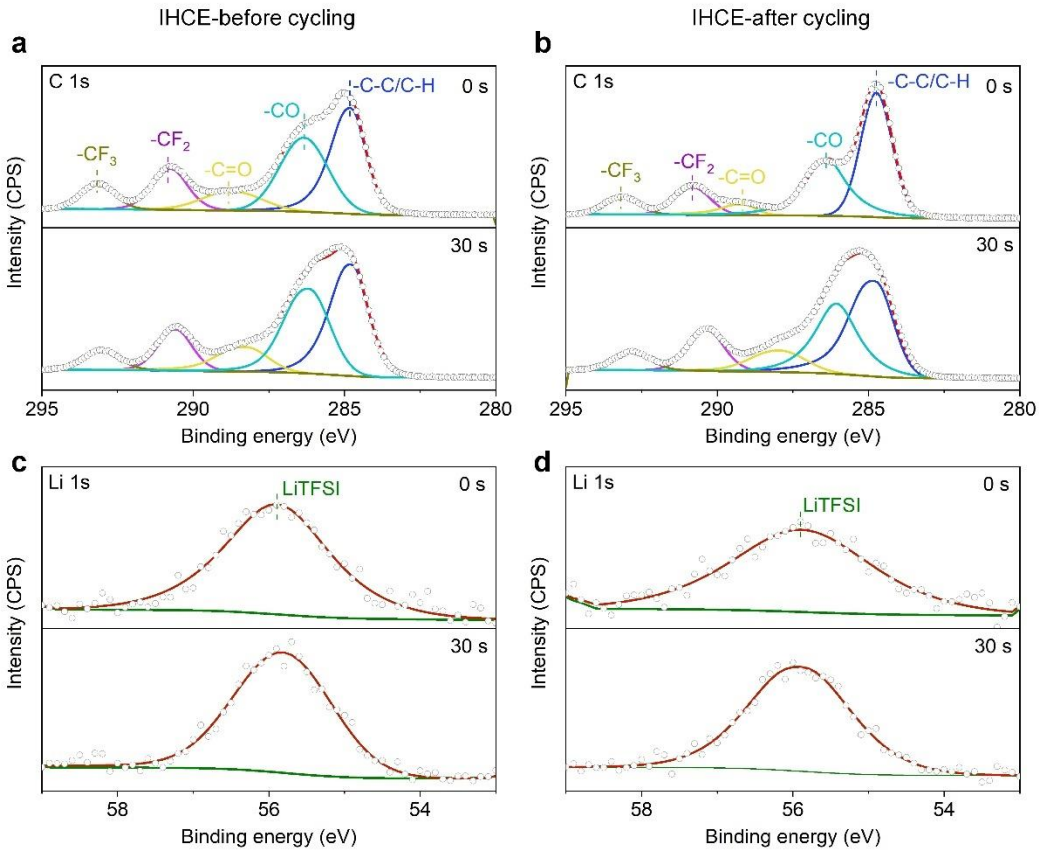

Fig. R21. Comparison of high-resolution XPS spectra of C 1s (a, b) and Li 1s (c, d) at the surface and after 30 s Ar^+ sputtering for IHCE membrane before and after cycling.

6. Post-cycling characterization issues:

The characterization results are confusing. Since the authors put the membrane on the Cu substrate as the working electrode, how to remove it after cycling and perform characterization like SEM and SIMS? Does it mean that the membrane is not stable and disappears after cycling?

Response: Thank you for your thoughtful comment. We confirm that the IHCE membrane remains chemically and mechanically stable after electrochemical cycling and does not degrade or disappear. However, for post-cycling analyses such as SEM and TOF-SIMS, it is essential to remove the membrane to analyze the deposited Li layer and SEI. To achieve this, we utilized anhydrous tetrahydrofuran (THF) as a selective solvent to dissolve the IHCE membrane. THF was originally employed as the dispersing solvent during the preparation of the IHCE@Cu coating solution and is capable of dissolving the polymer matrix without disturbing the underlying Li metal.

The cycled IHCE@Cu electrodes were gently rinsed with THF for 5 minutes inside an argon-filled glovebox, enabling effective removal of the membrane.

To validate the stability and selective removability of the IHCE, we performed comparative optical and SEM analyses. As shown in Fig. R22, the membrane begins to dissolve within 1 minute in THF and is nearly completely removed after 3 minutes, leaving only trace fragments inside the bottle wall. In contrast, the membrane remains structurally intact after 60 days of soaking in DME, clearly confirming its long-term chemical stability in the electrolyte environment. Moreover, cross-sectional SEM images of IHCE@Cu after Li plating (1 mAh cm^{-2}) were acquired before and after THF treatment (Fig. R23). The unwashed sample shows a continuous polymer layer covering the Li surface (Fig. R23a), while the washed sample reveals complete membrane removal, exposing the underlying Li deposit (Fig. R23b). These results collectively confirm that the membrane remains stable during cycling and can be selectively removed by THF for post-cycling analysis.

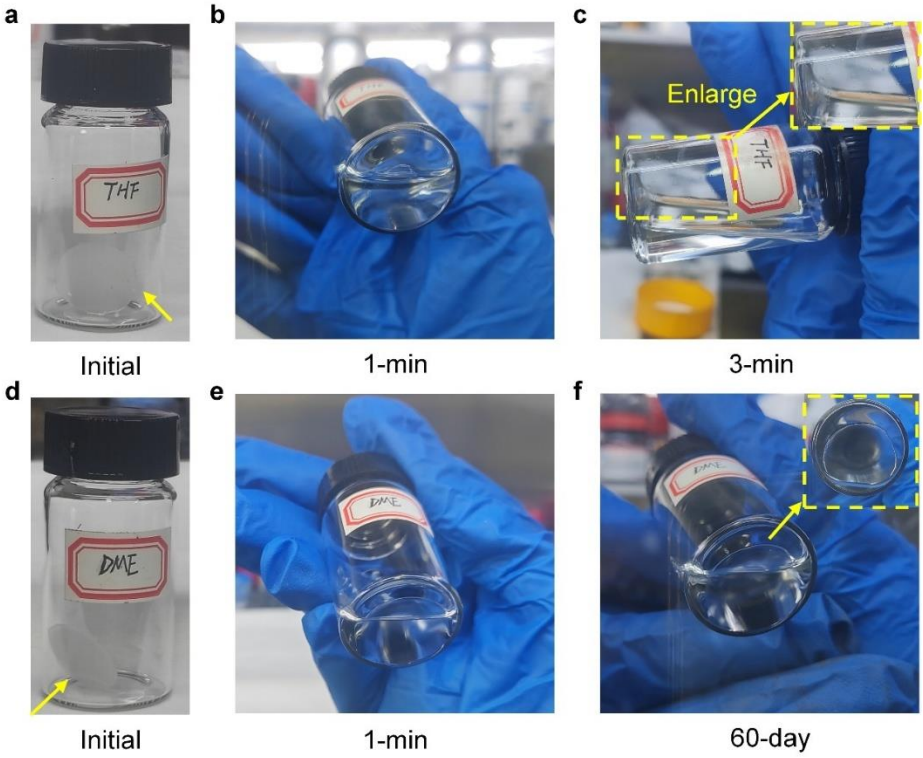

Fig. R22. Optical photographs of the IHCE membrane before and after immersion in anhydrous THF (a-c) and DME (d-f).

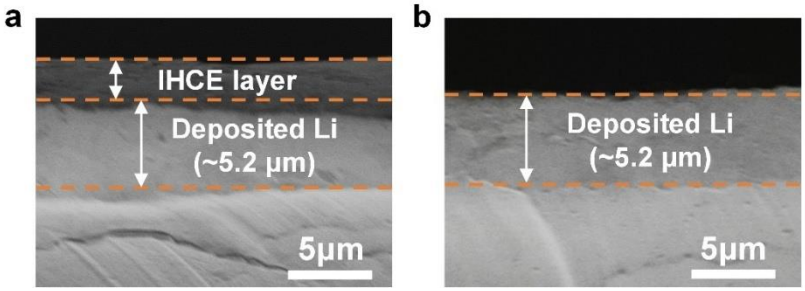

Fig. R23. Cross-sectional SEM image of Li deposition morphology on IHCE@Cu at a deposition capacity of 1 mAh cm^{-2}. a, without THF washing, showing the intact IHCE membrane covering the deposited Li. b, after THF washing, revealing the clean Li surface following complete removal of the IHCE layer.

7. Ionic conductivity of the PVDF-HFP/CPEGDA layer:

The origin of ionic conductivity for the PVDF-HFP/CPEGDA layer is not clear. At line 104, page 4, the manuscript presents a high ionic conductivity of 1.4×10^{-2} mS/cm. It is strange that this layer without Li salt can have a high ionic conductivity. What's the conducting agent in this layer?

Response: We thank the reviewer for raising this important point. The ionic

conductivity of the PVDF-HFP/CPEGDA polymer layer (1.4×10^{-5} S cm^{-1}) arises from LiTFSI, which was incorporated into the polymer matrix during the synthesis process. As described in the Methods section of the manuscript, LiTFSI was added at the beginning of the synthesis, before polymerization: "Firstly, 0.74 g PVDF-HFP, 0.46 g LiTFSI, and 8.34 g DMF were added to a round-bottomed flask and stirred at 50 °C until completely dissolved. The concentration of LiTFSI was controlled at 50 wt% relative to the total mass of the PVDF-HFP/CPEGDA polymers to obtain the polymer matrix of IHCE." After dissolution, PEGDA monomer, crosslinker, and initiator were added, followed by nitrogen bubbling and thermal curing to form the crosslinked structure. The LiTFSI remains embedded within the polymer network, serving as the mobile ion source. To avoid any further misunderstanding, we have clarified this point explicitly in the revised Methods and main text as follows:

(1) *Page 4, lines 108, 109 in the revised Manuscript*

"High ionic conductivity of 1.4×10^{-5} S cm^{-1}, as well as tensile strength of 91 MPa, were obtained at a PVDF-HFP/CPEGDA weight ratio of 8: 2 with 50 wt% LiTFSI."

(2) *Pages 16, 17, lines 413-419 in the revised Manuscript*

"PVDF-HFP (0.74 g), LiTFSI (0.46 g), and DMF (8.34 g) were added to a round-bottom flask and stirred at 50 °C until a homogeneous solution was obtained. After cooling to room temperature, PEGDA (0.15 g), 4-SH crosslinker (0.035 g), and AIBN (0.0018 g) were introduced into the mixture and dispersed thoroughly. The resulting solution was deoxygenated by purging with nitrogen for 1 h. Polymerization was then carried out by heating the mixture in an oil bath at 65 °C for 1 h, yielding a crosslinked CPEGDA network embedded with PVDF-HFP and LiTFSI."

8. Raman characterization details:

Please give a detailed description on the experimental set-up for Raman characterization of electrolyte and IHCE. How to characterize the IHCE layer with LiTFSI and DME?

Response: We thank the reviewer for highlighting the need to clarify our Raman characterization methodology. Given the high volatility of DME, solvent evaporation could alter the electrolyte concentration and compromise spectral accuracy. To address this, we employed sealed environments for both liquid electrolyte and DME-swollen IHCE membrane. The detailed procedures are as follows:

(1) Raman characterization of electrolyte:

To prevent DME evaporation, a small amount of electrolyte was drawn into a capillary tube inside an argon-filled glovebox. Both ends of the capillary was quickly flame-sealed after removal from the glovebox. This ensured that Raman spectra accurately reflected the original ionic coordination environment without being affected by solvent evaporation.

(2) Preparation of DME-swollen IHCE membrane.

LiTFSI was incorporated during the synthesis of the IHCE membrane to ensure homogeneous salt distribution. The synthesis process is described in the Methods section. After polymerization, the solution was cast into a PTFE mold and cured at 70 °C for 12 hours to form a self-standing IHCE membrane. The resulting IHCE membrane was then cut into 9-mm diameter discs and immersed in DME for 1 hour inside an argon-filled glovebox to enable complete solvent absorption.

(3) Raman characterization of DME-swollen IHCE.

For Raman analysis, the DME-swollen IHCE membrane was placed into a sealed in-situ Raman cell. As illustrated in Fig. R24, the cell consisted of a base with an O-ring (Ø = 10 mm, Fig. R24a) to ensure a tight seal. The IHCE membrane was placed in the central region, covered with a transparent optical window (Ø = 22 mm, Fig. R24b) to allow laser penetration while preventing DME evaporation. Finally, a metal cell lid was secured (Fig. R24c, d). All assembly steps were conducted inside an argon-filled glovebox before removing the sealed cell for Raman measurement.

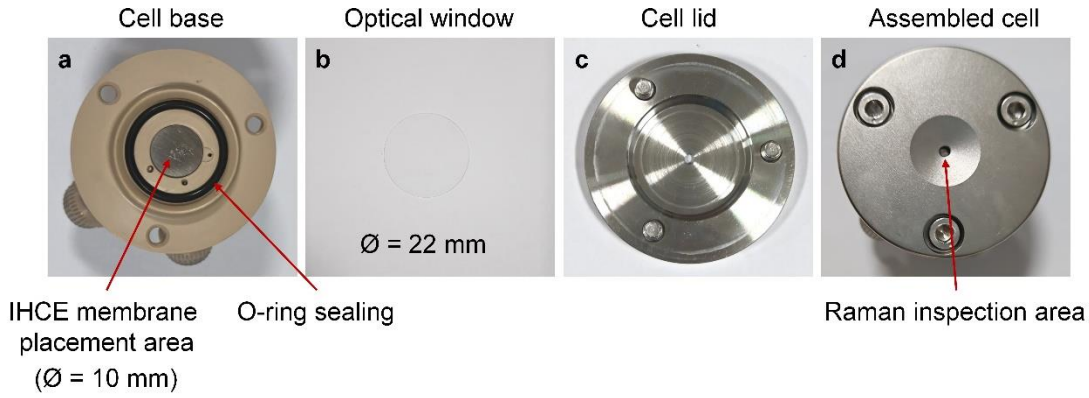

Fig. R24. Raman cell setup images.

9. Energy density calculations:

What rate is used for calculating the energy density (506.3 Wh kg^{-1}) shown in the manuscript? And what's the cell energy density at 0.5 C rate?

Response: Thank you for your question. The energy density (506.3 Wh kg^{-1}) reported in the manuscript was measured at the rate of 0.1 C. The total mass of the cell - including the cathode, anode, electrolyte, separator, aluminum current collector, packaging, and lugs - was 0.05104 kg. Detailed parameters have been included in Table R24. The calculation follows the standard Equation (48):

$$Energy\ \ density\ \ (Wh\ \ kg^{-1}) = \frac{\text{Discharge capacity (Ah)} \times \text{Mid} - \text{value voltage (V)}}{\text{Total weight (kg)}} \quad (48)$$

(1) At 0.1 C, an initial discharge capacity of 6.8 Ah and a mid-value voltage of 3.8 Ah were obtained, resulting in:

$$Energy\ \ density\ \ (Wh\ \ kg^{-1}) = \frac{6.8\ \ Ah\ \ \times 3.8\ \ V}{0.05104\ \ (kg)} \approx 506\ \ Wh\ \ kg^{-1} \quad (49)$$

Table R24. The detailed parameters of the energy density calculation (0.1 C).

Discharge capacity (Ah)	Mid-value voltage (V)	Cycling condition (C-rate)	Total weight (kg)	Energy density (Wh kg^{-1})
6.8	3.8	0.1	0.05104	506

(2) At 0.5 C, a discharge capacity of 6.2 Ah was achieved. The energy density was calculated as:

$$Energy\ density\ (Wh\ kg^{-1}) = \frac{6.2\ Ah \times 3.8\ V}{0.05104\ (kg)} \approx 462\ Wh\ kg^{-1} \quad (50)$$

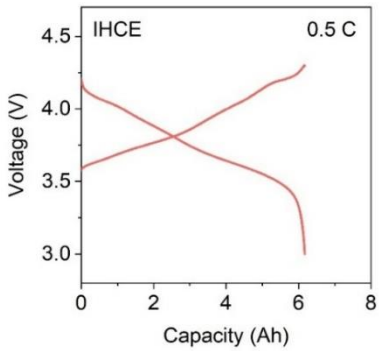

Fig. R25. Voltage profiles of IHCE@Li||NCM811 pouch cells at 0.5 C.

Table R25. The detailed parameters of the energy density calculation (0.5 C).

Discharge capacity (Ah)	Mid-value voltage (V)	Cycling condition (C-rate)	Total weight (kg)	Energy density (Wh kg^{-1})
6.2	3.8	0.5	0.05104	462

10. Membrane properties:

Can the membrane be self-supporting? With substrate like Cu, it can only be used in anode-free batteries, then its effectiveness in Li metal pouch cells drastically weakens.

Response: We sincerely appreciate your insightful comment. We confirm that IHCE membrane is fully self-supporting and does not rely on any substrate, such as Cu, for structural integrity. Below, we provide clarification regarding its mechanical properties and practical application in various battery configurations.

The self-supporting nature of the IHCE membrane is demonstrated in Fig. R26, which shows the membrane in its original, wrapped, and folded states, highlighting its remarkable flexibility. In addition, the IHCE membrane exhibits a tensile strength of 91 MPa (Supplementary Fig. 4b), indicating its mechanical robustness and ability to function independently without a support layer.

In our study, the IHCE was employed in multiple cell configurations by directly coating it onto electrode surfaces (Li or Cu). Cu foil was used only in Li||Cu half cells for visualization of Li deposition morphology (Fig. 4 and Supplementary Figs. 20-22).

In Li||Li symmetric cells, Li||NCM811 coin cells, and Li metal pouch cells, IHCE layer was coated directly onto the Li metal foil, forming a compact and uniform protective layer. The detailed preparation process for both IHCE@Cu and IHCE@Li electrodes was described in the Methods section. Importantly, the IHCE membrane is not limited to anode-free batteries, as demonstrated in our results. In IHCE@Li||Li cells, stable cycling over 300 h was achieved with a low and stable overpotential of 43 mV at 4 mA cm^{-2}, whereas both HCE and SCE exhibited overpotentials exceeding 200 mV after only 20 h (Supplementary Fig. 25). Additionally, in IHCE@Li||NCM811 full cells, 82% capacity retention was maintained after 328 cycles at 0.5 C (Fig. 6a), further confirming the interfacial stability imparted by IHCE. More importantly, in IHCE@Li||NCM811 pouch cells, the IHCE was also directly coated onto Li foil to form the IHCE@Li anode without Cu substrate. These pouch cells delivered a high energy density of 506 Wh kg^{-1} and retained 75.8% capacity over 200 cycles at 0.5 C (Fig. 6f), demonstrating the practicality and structural integrity of IHCE in large-format lithium metal batteries. These results confirm that IHCE is fully applicable to traditional Li metal pouch cells and is not limited to anode-free batteries.

Fig. R26. Photographs of the self-supporting IHCE membrane in its original (a), wrapped (b), and folded states (c).

Review #3 (Remarks to the Author):

Overall comment: This work proposes a strategy to constrain a high salt concentration through a polymer at the electrolyte-electrode interface to enhance interfacial cycling performance. While this approach appears effective in the short term, a key question remains: how long such a salt-rich interface can be maintained to provide long-term benefits? Furthermore, I have some questions regarding the research to understand the salt-retention mechanism.

Response: We sincerely appreciate the reviewer's constructive feedback. The long-term stability of the salt-rich interface layer and the underlying salt-retention mechanism are indeed critical to evaluating the effectiveness of our IHCE strategy. In response, we have carefully revised the manuscript to clarify these aspects and provided a detailed explanation in the point-by-point responses below.

1. Part 2.1 explains how the IHCE was developed; however, the information on the standard bulk electrolyte used in this work is missing from this section. Instead, it is introduced later on page 7. This disrupts the logical flow and makes it difficult to follow and understand the discussions before knowing the bulk electrolyte composition.

Response: Thank you for this helpful comment. We agree that the delayed description of the bulk electrolyte composition may interrupt the logical flow and cause ambiguity in understanding the design of the IHCE system. To address this, we have revised the manuscript to introduce the bulk electrolyte compositions earlier in the text. These formulations are now briefly referenced in Part 2.1 and comprehensively detailed in the "Coin cell assembly" of the Methods section.

Updated in the revised Manuscript (*Page 4, lines 91-98*

"In this work, we constructed a salt-concentrated interfacial layer based on a polymer matrix of poly(vinylidene fluoride-co-hexafluoropropylene) (PVDF-HFP) and cross-linked polyethylene glycol diacrylate (CPEGDA) (Fig. 2a, b). This interfacial layer was integrated with standard-concentration bulk electrolyte, consisting of 1 M LiFSI in DME, for use in half-cell configurations. As shown in Supplementary Table 1, PVDF-

HFP and CPEGDA exhibit a large Flory-Huggins interaction parameter (χ = 6.5 k), determined through contact angle measurements (Supplementary Fig. 1 and Note 1), which facilitates the formation of a bicontinuous phase microstructure".

2. Part 2.2 tried to verify the retention function of IHCE and the mechanism. I have a few questions regarding this part.

1) Although the soaking experiment provides insight into the salt retention capability of the IHCE materials, i.e. how well it can trap and hold the salt within the polymer matrix in the absence of the dynamics cycling conditions, however, it may not reflect the real battery conditions. In an actual battery, current flow, ion transport during charging and discharging, and electrochemical reactions continuously alter the salt concentration in the IHCE over time. Whether the IHCE can constrain salt during and after cycling is critical for the practical application of this strategy. In addition, if the electrolyte is not DME, it will also affect the result of the soaking experiment. It is not clear what electrolyte has been used.

Response: We thank the reviewer for the thoughtful and constructive comments regarding the salt retention ability of IHCE under realistic electrochemical conditions. Below, we address the concerns you raised in detail.

(1) Salt-retention ability of IHCE after electrochemical cycling.

To evaluate whether the IHCE can retain lithium salt after cycling, we performed post-cycling characterization using XPS depth profiling, Raman spectroscopy and UV-Vis spectroscopy, following extended electrochemical operation. Specifically, Li||Cu half cells were assembled using self-supporting IHCE membranes in direct contact with Li metal, and subjected to cycling at 1 mA cm^{-2} with a deposition capacity of 1 mAh cm^{-2} for 50 cycles. After cycling, the cells were disassembled in an argon-filled glovebox, and the IHCE membranes were carefully retrieved, rinsed with anhydrous DME to remove residual surface electrolyte salt, and vacuum-dried for subsequent analysis.

As shown in Fig. R27, the Li 1s XPS signal corresponding to LiTFSI (~55.8 eV)

remains clearly detectable on the cycled IHCE surface, with only a minor reduction in intensity. After 30 s of Ar^+ sputtering, the Li 1s signal closely resembles that of the uncycled membrane, indicating that LiTFSI remains effectively confined within the polymer matrix during cycling. Moreover, the structural integrity of the IHCE membrane is also preserved after cycling. C 1s XPS spectra from PVDF-HFP (~292.9 eV for -CF_3 and ~290.4 eV for -CF_2) and CPEGDA (~288.3 eV for -C=O and ~286.6 eV for -C-O) remain consistent before and after cycling, confirming the chemical stability of the polymer network. Additionally, Raman spectroscopy (Fig. R28) reveals that the S-N-S stretching vibrations of $TFSI^-$ (~745 cm^{-1}) remains detectable on the cycled IHCE surface, further confirming the retention of LiTFSI within the interfacial layer after cycling.

To quantitatively assess the residual salt concentration, we employed UV-Vis spectroscopy. The polymer components in the IHCE matrix exhibit no UV absorbance, while LiTFSI displays distinct absorbance peak ~210 nm, corresponding to the n→π* transition of -SO_2 in LiTFSI, making it suitable for quantification. IHCE membranes of identical mass (33 mg) were dissolved in 6 ml of THF before and after cycling, and the UV absorption spectra were measured. A UV standard curve was first established using a series of LiTFSI-THF standard solutions with known concentrations (Fig. R29). The UV absorption spectrum of the THF solution containing the uncycled IHCE membrane (Fig. R30) was then recorded. Using the standard curve equation, the uncycled IHCE was yielded a LiTFSI concentration of 5.0 M, which is in excellent agreement with the designed concentration. This result validates the reliability and accuracy of the UV-based quantification method for LiTFSI content. After cycling, the same procedure was applied to the cycled IHCE membrane (Fig. R30), and the residual LiTFSI concentration was determined to be 4.6 M based on Equations (51)-(53). The detailed results are provided in Table R26. These findings conclusively demonstrate that the IHCE retains a high-concentration LiTFSI environment even after electrochemical cycling, confirming its salt confinement capability under realistic operating conditions.

Standard curve equation:

$$y = 0.1056 \times x + 0.6572 \tag{51}$$

$$\begin{aligned} m_{residual\ LiTFSI\ in\ IHCE} &= x \times V_{THF} \\ &= \frac{y - 0.6572}{0.1056} \times 6 \\ &= \frac{1.046 - 0.6572}{0.1056} \times 6 \\ &= 10.098\text{mg} \end{aligned} \tag{52}$$

$$\begin{aligned} C_{residual\ LiTFSI\ in\ IHCE} &= \frac{m_{residual\ LiTFSI\ in\ IHCE}}{M_{LiTFSI} \times V_{solvent\ uptake\ of\ IHCE}} \\ &= \frac{10.098}{287.09 \times \frac{m_{polymer\ in\ dry-IHCE} \times 0.3}{\rho_{DME}} \times 10^{-3}} \\ &= \frac{10.098}{287.09 \times \frac{33 \times 0.668 \times 0.3}{0.867} \times 10^{-3}} \\ &= 4.6\text{M} \end{aligned} \tag{53}$$

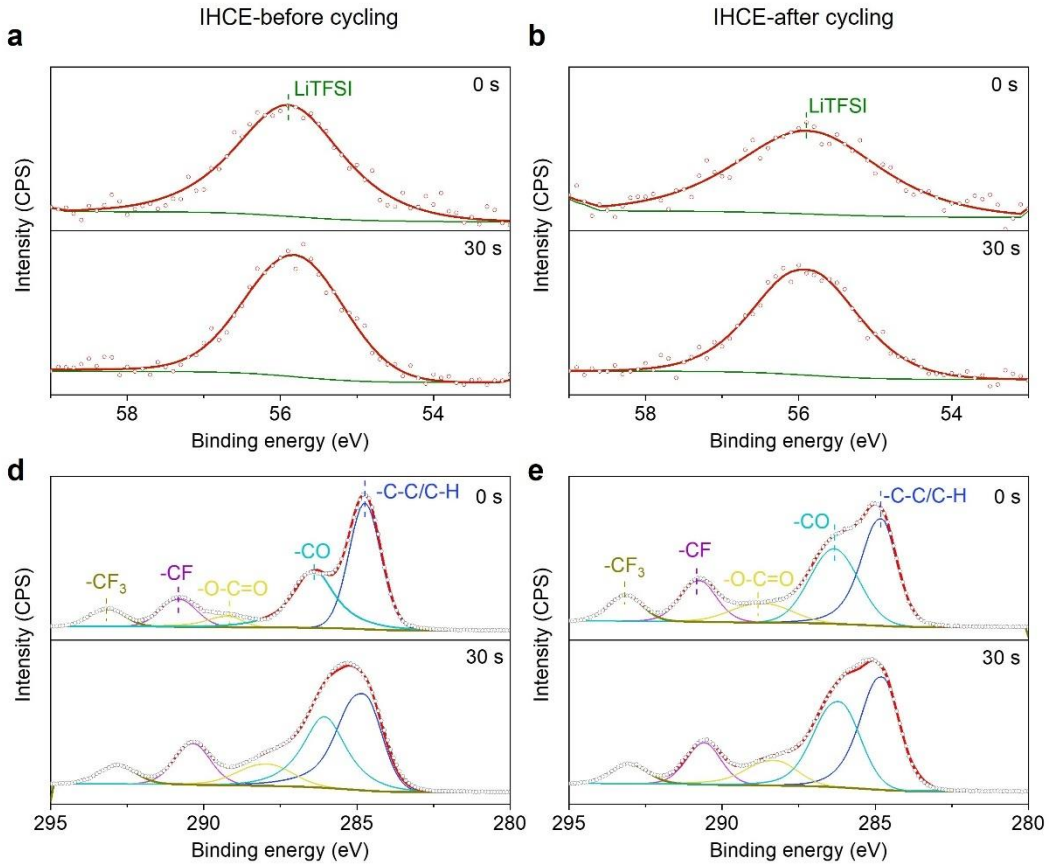

Fig. R27. Comparison of high-resolution XPS spectra of Li 1s (a, b) and C 1s (c, d) at the surface and after 30 s Ar+ sputtering for IHCE membrane before and after cycling.

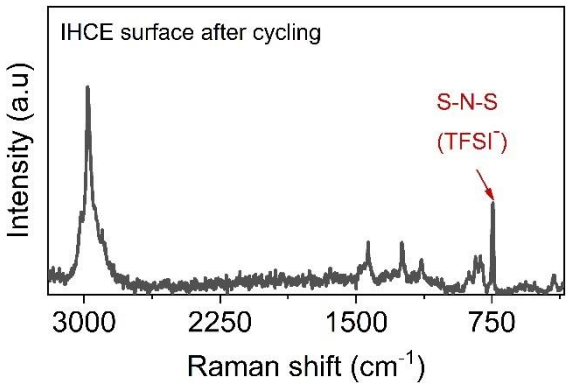

Fig. R28. Raman spectrum of IHCE@Cu surface after 50 cycles under 1 mA cm^{-2} with a deposition capacity of 1 mAh cm^{-2}.

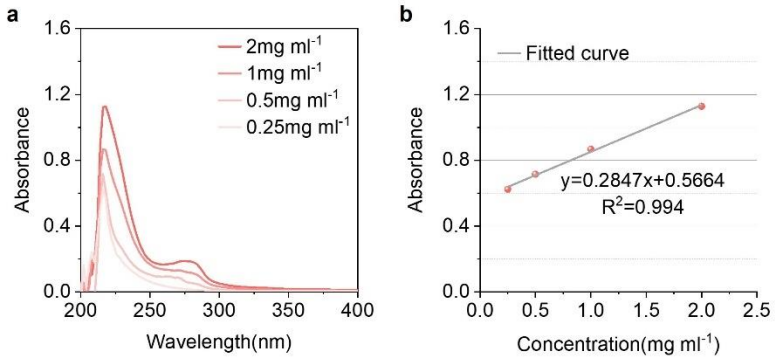

Fig. R29. The UV/Vis spectra of LiTFSI-THF solutions at various mass concentrations (a) and the corresponding standard line (b).

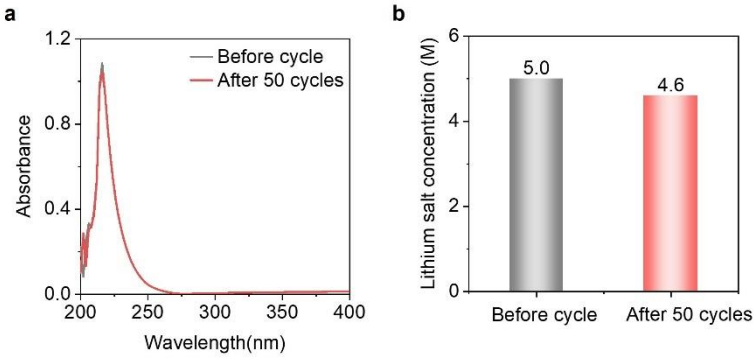

Fig. R30. Quantitative monitoring of LiTFSI concentration of IHCE membranes via ultraviolet-visible (UV-Vis) measurements before and after 50 cycles.

Table R26. Parameters and results of UV measurements.

	Mass of dry-IHCE (mg)	Volume of THF (ml)	UV absorbance (y)	Mass concentration (x, mg ml^{-1})	LiTFSI in IHCE	
					Mass (mg)	Concentration (M)
Before cycle	33	6	1.087	1.827	10.960	5.0
After 50 cycles	33	6	1.046	1.683	10.098	4.6

(2) Solvent dependence of salt-retention behavior of IHCE.

To further evaluate the solvent dependence of the salt-retention behavior of IHCE, UV-Vis spectroscopy was also employed following soaking experiments in a carbonate-based solvent system (FEC/DEC, 1:2 v/v). Similar to the DME-based procedure, UV-Vis analysis was used to quantify the amount of LiTFSI retained in the IHCE membrane after immersion in the carbonate solvent. Notably, the solvent uptake of IHCE in FEC/DEC mixed solvent was measured to be ~31%, and the density of FEC/DEC (1.135 g cm^{-3}) is significantly higher than that of DME (0.867 g cm^{-3}). As a result, the same mass of IHCE membrane in FEC/DEC exhibits a higher internal electrolyte concentration of ~6.34 M, compared to 5.0 M in the DME-based system.

To quantify the amount of LiTFSI leached into FEC/DEC, a UV standard curve was first established by measuring the absorbance spectra of a series of LiTFSI-FEC/DEC standard solutions at ~210 nm (Fig. R31). Seven identical IHCE membranes were individually immersed in 3 ml of anhydrous FEC/DEC (1: 2, v/v) and sealed in an argon-filled glove box for 2, 5, 10, 20, 30, 40, and 50 days, respectively. The corresponding masses of each IHCE membrane were 51.53, 50.72, 49.23, 48.16, 48.07, 49.76, and 50.09 mg, respectively. According to the synthesis protocol, the mass ratios of LiTFSI (33.2%) and polymer matrix (66.8%) in the total IHCE (Supplementary Table 4), and combined with the solvent uptake ratio and density, the initial LiTFSI content in each membrane was estimated.

The concentration of dissolved LiTFSI was determined based on Equations (54)-(56). The initial LiTFSI and the residual LiTFSI contents for each membrane are summarized

in Tables 27, 28. As shown in Fig. R32, even after 50 days of immersion in FEC/DEC, the IHCE maintained a residual LiTFSI concentration >4.55 M. Compared to the initial 6.34 M concentration of LiTFSI in IHCE (FEC/DEC solvent), the daily dissolution rate was less than 0.98% during 2-50 days, demonstrating the good salt-retention ability of IHCE in carbonate-based electrolyte solvent.

These findings indicate that salt-confinement mechanism in IHCE, driven by spatial confinement and molecular interactions, remains effective across both carbonate and ether-based electrolytes, highlighting the broad applicability of the IHCE strategy. Accordingly, we have updated corresponding discussions and revisions to the revised Manuscript and Supplementary Information.

Updated in the revised Manuscript (*Page 6, lines 145-147*):

"Moreover, IHCE also exhibited similarly strong salt-retention performance in carbonate-based solvents such as FEC/DEC, as detailed in Supplementary Fig. 10, 11, Tables 7, 8 and Note 5".

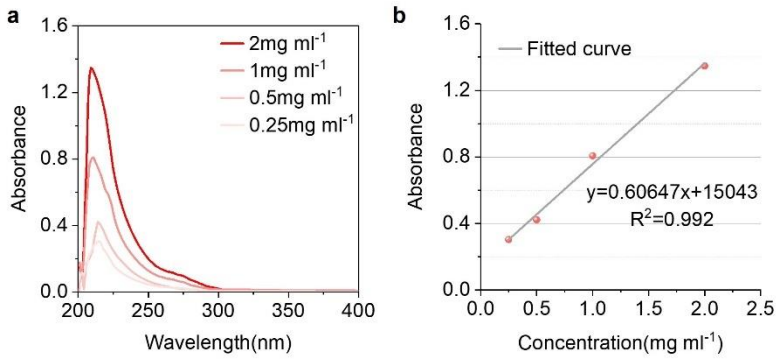

Fig. R31. The UV/Vis spectra of LiTFSI-FEC/DEC (1: 2, v/v) solutions at various mass concentrations (a) and the corresponding standard line (b).

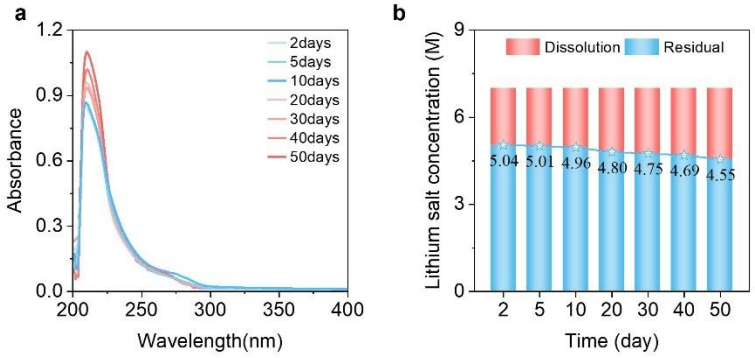

Fig. R32. a, Quantitative monitoring of LiTFSI dissolution concentration of IHCE in the FEC/DEC (1: 2, v/v) immersion solution via ultraviolet-visible (UV-Vis) measurements over various days. b, Dissolution and residual concentration profiles of LiTFSI in IHCE versus immersion time.

Table R27. Usage of FEC/DEC mixed solvent and dry-IHCE for UV experiments.

Time (day)	Usage of FEC/DEC (ml)	Soaked dry-IHCE (mg)	Initial LiTFSI content in dry-IHCE (mg)
2	3	51.53	17.11
5	3	50.72	16.85
10	3	49.23	16.35
20	3	48.16	16.00
30	3	48.07	15.97
40	3	49.76	16.53
50	3	50.09	16.64

Standard curve equation:

$$y = 0.60647 \times x + 0.15043 \tag{54}$$

$$m_{dissolved\ \ LiTFSI} = x \times V_{FEC+DEC} = \frac{y - 0.15043}{0.60647} \times 3 \tag{55}$$

$$C_{residual\ LiTFSI\ in\ IHCE} = \frac{m_{residual\ LiTFSI\ in\ IHCE}}{M_{LiTFSI} \times V_{solvent\ uptake\ of\ IHCE}} = \frac{m_{LiTFSI\ in\ dry-IHCE} - m_{disssolved\ LiTFSI}}{287.09 \times \frac{m_{polymer\ in\ dry-IHCE} \times 31\%}{\rho_{FEC+DEC}}} = \frac{(m_{dry-IHCE} \times 0.332) - \left(\frac{y - 0.15043}{0.60647} \times 3\right)}{287.09 \times \frac{m_{dry-IHCE} \times 0.668 \times 31\%}{1.135} \times 10^{-3}} \quad (56)$$

Where "*y*" represents the UV absorbance of the LiTFSI-FEC/DEC (1: 2, v/v) solutions. "*x*" is the mass concentration of LiTFSI-FEC/DEC (1: 2, v/v). "*m*" is the mass. "*V*" is the volume. "*ρ*" is the density of LiTFSI-FEC/DEC (1: 2, v/v). "*C*" indicates the molar concentration.

Table R28. Parameters of UV experiments.

Time (day)	UV absorbance (y)	LiTFSI in FEC/DEC		Residual LiTFSI in IHCE	
		Concentration (x, mg ml^{-1})	Mass (mg)	Mass (mg)	Concentration (M)
2	0.860	1.170	3.510	13.60	5.04
5	0.865	1.178	3.535	13.31	5.01
10	0.870	1.186	3.559	12.79	4.96
20	0.936	1.295	3.886	12.11	4.8
30	0.960	1.335	4.005	11.96	4.75
40	1.020	1.434	4.301	12.22	4.69
50	1.100	1.566	4.697	11.94	4.55

2) FTIR shows interactions between PVDF-HFP and DME, and between TFSI and DME. However, the binding energy is a positive value here which raised questions. Typically, binding energy is negative for favorable interactions, indicating an exothermic process. A more positive binding energy value usually suggests weaker and less stable interactions. Based on the reported values, the DME-TFSI$^-$ interaction should be slightly stronger (2.26 vs. 2.84 kcal mol^{-1} for PVDF-HFP-TFSI$^-$). This

contradicts the explanation provided in the text. Please clarify how these binding energies were calculated and provide details about the methodology.

Response: We thank the reviewer for the careful observation and valuable feedback. We apologize for the confusion caused by the earlier description of the binding energies. As the reviewer correctly pointed out, binding energy should conventionally be expressed as a negative value for favorable (exothermic) interactions, with more negative values indicating stronger binding. In our initial version, the calculated binding energies for PVDF-HFP-$TFSI^-$ and DME-$TFSI^-$ were -2.84 kcal mol^{-1} and -2.26 kcal mol^{-1}, respectively. To facilitate an intuitive comparison of the interaction strength, we plotted the absolute values of these energies in a bar chart format. However, this was not clearly stated in the main text, which may have led to a misunderstanding.

In our previous computational approach, we performed geometry optimization and frequency analysis using B3LYP/6-31G+(d)/SMD, combined with single-point energy calculations employing the 6-311G+(d,p) basis set. This approach is commonly used and provides reliable thermodynamic data for conventional molecular systems[12]. However, inspired by a recently published study[13] that demonstrated improved accuracy in modeling weak noncovalent interactions, we have adopted a more rigorous computational protocol in the revised version: (a) Geometry re-optimization using M06-2X/6-311G+(d,p)/SMD with confirmation of no imaginary frequencies. This functional significantly enhances the modeling of weak interactions through empirical dispersion correction and accurate description of medium-range electron correlation effects[14]; (b) During single-point energy calculations at the M06-2X/Def2-TZVP level, counterpoise for basis set superposition error (BSSE) was applied[15]. This combined methodology rigorously addresses long-range dispersion interactions and basis set incompleteness errors, yielding more accurate binding energy calculations and reliable descriptions of weak interactions in the system[14,15].

Using this refined methodology, the recalculated binding energies are as follows: PVDF-HFP-$TFSI^-$: -15.03 kcal mol^{-1} and DME-$TFSI^-$: -7.91 kcal mol^{-1}, respectively (Fig. 3e). These updated results also demonstrate that $TFSI^-$ binds more strongly to

PVDF-HFP than to DME, reinforcing our original conclusion that PVDF-HFP provides superior anion anchoring ability and enables salt retention within the IHCE structure. The updated results have been incorporated into Figure 3 of the revised Manuscript. In addition, the detailed computational methodology has been updated in the Methods section - DFT calculations (*Pages 21, 22, lines 571-528*) as follows:

"All DFT calculations were performed using Gaussian 16. Geometry optimizations and vibrational frequency analyses were conducted at the M062X hybrid functional[14] with the 6-311+G(d,p) basis set. The solvent effects were incorporated via the SMD solvation model[16] to simulate an implicit solvent environment. Frequency calculations confirmed the absence of imaginary frequencies, ensuring all optimized structures corresponded to local minima on the potential energy surface.

Subsequent single-point energy calculations were carried out at the M06-2X functional with the Def2-TZVP basis set[17]. For M06-2X, the default DFT-D3(0) dispersion correction with zero-damping was applied, as the functional inherently includes medium-range correlation effects[18]. To account for Basis Set Superposition Error (BSSE) in interaction energy calculations, the counterpoise method[15] was employed. The binding energy was calculated (E_{BE}) as:

$$E_{BE} = E_{AB} + E_{BSSE} - E_A - E_B \quad (57)$$

where "E_{AB}" is the energy of the dimer system, "E_A" and "E_B" are the energies of the isolated monomers, and "E_{BSSE}" denotes the BSSE correction term derived from the counterpoise correction method."

3). MD simulation details:

The structural information of PVDF-HFP and CPEGDA in the simulation is unclear. For example: What does "20 units PVDF-HFP" refer to? Does it mean 20 polymer chains? What is the structure of each chain? How is CPEGDA connected to PVDF-HFP? Is it covalently linked or physically mixed? How was the COMPASS III force field validated for this specific system? Furthermore, the annealing process details are insufficient. What does "the lowest energy configurations" refer to? Is it the final

configuration after annealing or a configuration chosen based on energy minimization criteria? Please provide additional information on the structural optimization and annealing protocols.

Response: We sincerely thank the reviewer for these detailed and constructive comments. We agree that clarification of the simulation methodology is essential, and we provide full responses to each point below.

The term "20 units PVDF-HFP" refers to 20 individual polymer chains, each containing two repeat units. Each repeat unit consists of nine vinylidene fluoride (VDF) monomers and one hexafluoropropylene (HFP) monomer, consistent with experimental composition ratios. The CPEGDA chains were physically mixed with PVDF-HFP chains in the simulation box, consistent with the experimental fabrication process described in the Methods section. The molecular structures of PVDF-HFP, CPEGDA, LiTFSI, and DME used in the simulation are shown in Fig. R33 and have also been included in the Supplementary Fig. 12 for clarity.

We employed the COMPASS III force field because it offers broad coverage for organic, inorganic, and polymeric systems based on first-principles parameterization. It has been widely validated in prior studies for accurately modeling polymer segmental dynamics, ion-polymer interactions, and solvation structures, especially for systems comprising C, H, O, N, S, and F elements[19]. This validation supports its applicability to our IHCE system.

To achieve a thermodynamically stable configuration, we performed an annealing process of 20 cycles, ramping the system temperature between 298 K and 500 K. Simulations were carried out under the NPT ensemble, using the Nose thermostat for temperature control and the Berendsen barostat for pressure regulation, respectively. A time step of 1 fs was used, and the total annealing time was 100 ps. The term "lowest-energy configurations" refers to the final structure obtained after annealing, selected based on energy minimization criteria. This configuration represents the most stable configuration for subsequent process.

To improve clarity, we have updated the Methods section of the revised Manuscript (*Pages 20, 21, lines 551-569*) as follows:

"Molecular dynamics (MD) simulations were employed to model the IHCE membrane structures, followed by pore distribution analysis using the Zeo++ code. The initial system consisted of 20 PVDF-HFP chains, each containing two repeat units made up of nine vinylidene fluoride (VDF) monomers and one hexafluoropropylene (HFP) monomer. In addition, the system included 5 CPEGDA chains, and 123 DME molecules. These components were randomly packed into a cubic simulation box with PVDF-HFP and CPEGDA physically mixed. The molecular structures of PVDF-HFP, CPEGDA, LiTFSI, and DME used in the simulation are shown in Supplementary Fig. 12. Simulations were performed using the COMPASS III force field in the Materials Studio 2020. Van der Waals and Coulomb interactions were calculated using atom-based and Ewald methods, respectively, with a cut-off value of 12.5 Å. The model was initially subjected to structural optimization. To achieve a thermodynamically stable configuration, we performed an annealing process of 20 cycles, ramping the system temperature between 298 K and 500 K. Simulations were carried out under the NPT ensemble, using the Nose thermostat for temperature control and the Berendsen barostat for pressure regulation, respectively. A time step of 1 fs was used, and the total annealing time was 100 ps. Subsequently, the lowest-energy configuration obtained after annealing was fully relaxed under periodic boundary conditions for 800 ps in the NPT ensemble (P = 1 atmosphere, T = 298.0 K). A 5 ns production run was finally conducted in the canonical (constant NVT) ensemble under the Nose-Hoover thermostat. This simulation time was sufficient for the system to reach equilibrium of temperature, potential and total energy. Finally, the equilibrium configuration was analyzed using Zeo++ (version 0.3)[20–22] and the atom volumes & surfaces tool in Materials Studio."

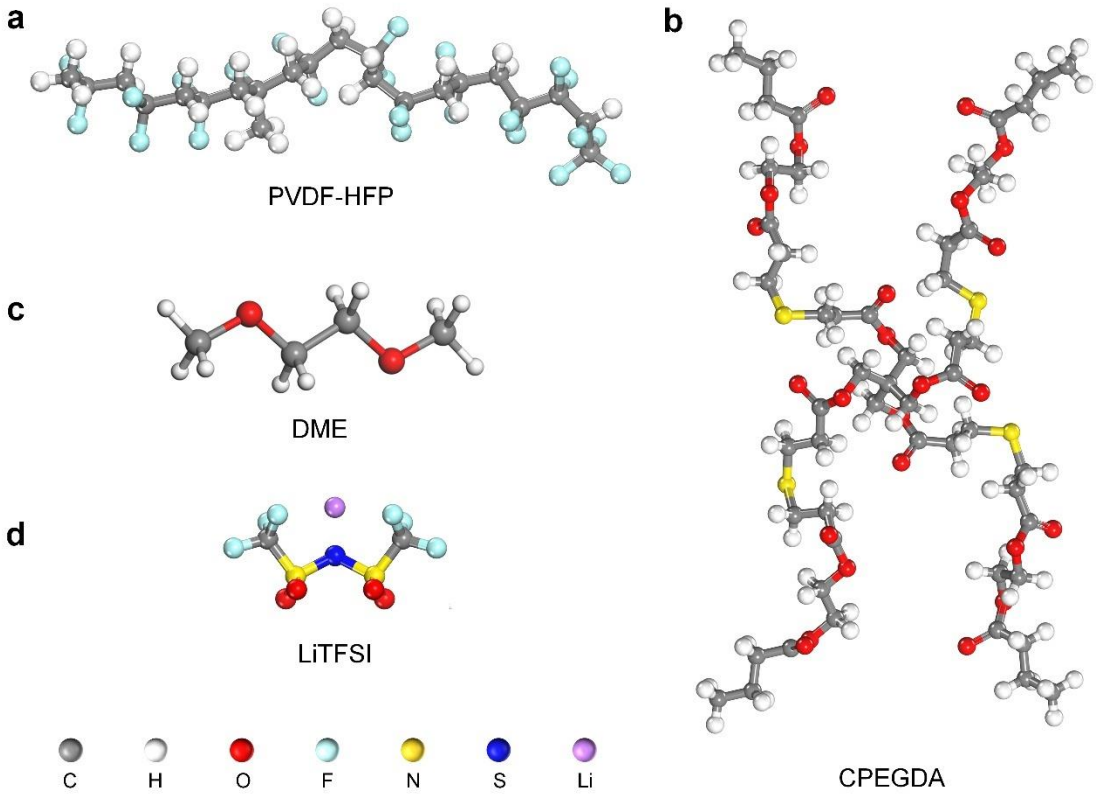

Fig. R33. Molecular structures of representative PVDF-HFP chains (a), CPEGDA chains (b), DME (c), and LiTFSI (d) used in the simulation.

4). The stated purpose of the MD simulation is to understand the salt-retention mechanism. However, the absence of LiTFSI salt in the model invalidates this objective. The observed porosity results from the polymer structure and DME, which is expected as polymers generally exhibit free volumes. Without explicitly including salts, the simulation cannot capture the spatial effects of salts on pore size or provide insight into ion-polymer, solvent-polymer, or solvent-ion interactions. The discussion of pore size in the current system is thus meaningless. The simulation does not provide any meaningful insights into the salt-retention mechanism.

Response: Thank you for your professional question. We fully agree that the absence of LiTFSI in the original MD simulations limited the validity of conclusions related to the salt-retention mechanism. To address this concern, we conducted additional MD simulations incorporating LiTFSI to better elucidate the spatial confinement for salt retention in the IHCE.

Specifically, we compared the following three systems: (i) polymer blends: PVDF-

HFP/CPEGDA, (ii) polymer blends + solvent: PVDF-HFP/CPEGDA-DME, and (iii) IHCE system: PVDF-HFP/CPEGDA-DME-LiTFSI. As shown in Fig. R34, the inclusion of DME leads to an increase in total free volume from 7275 $Å^3$ to 10319 $Å^3$, due to expanded polymer network and enhanced segmental mobility. Upon the addition of LiTFSI, the free volume decreases to 9530 $Å^3$, indicating that LiTFSI partially occupies the free volume within the polymer matrix. Furthermore, pore size distribution analysis revealed that in IHCE system, the majority of pores are narrowly distributed below 2.5 Å, which is significantly smaller than the solvated diameter of $TFSI^-$ (>9 Å). These results demonstrate that the polymer matrix can impose significant spatial confinement on $TFSI^-$, thereby impeding its transport.

To further validate this, we calculated the diffusion coefficient (D) of $TFSI^-$ within the IHCE layer and compared it with that in a standard 1 M LiTFSI-DME electrolyte (SCE). D_{TFSI^-} in the IHCE was found to be 0.04×10^{-2} Å ps^{-1}, whereas it was 2.47×10^{-2} Å ps^{-1} in the SCE (Fig. R35). This represents a ~98.4% reduction in $TFSI^-$ mobility, supporting that the polymer matrix effectively confines $TFSI^-$, even when the IHCE is exposed to SCE.

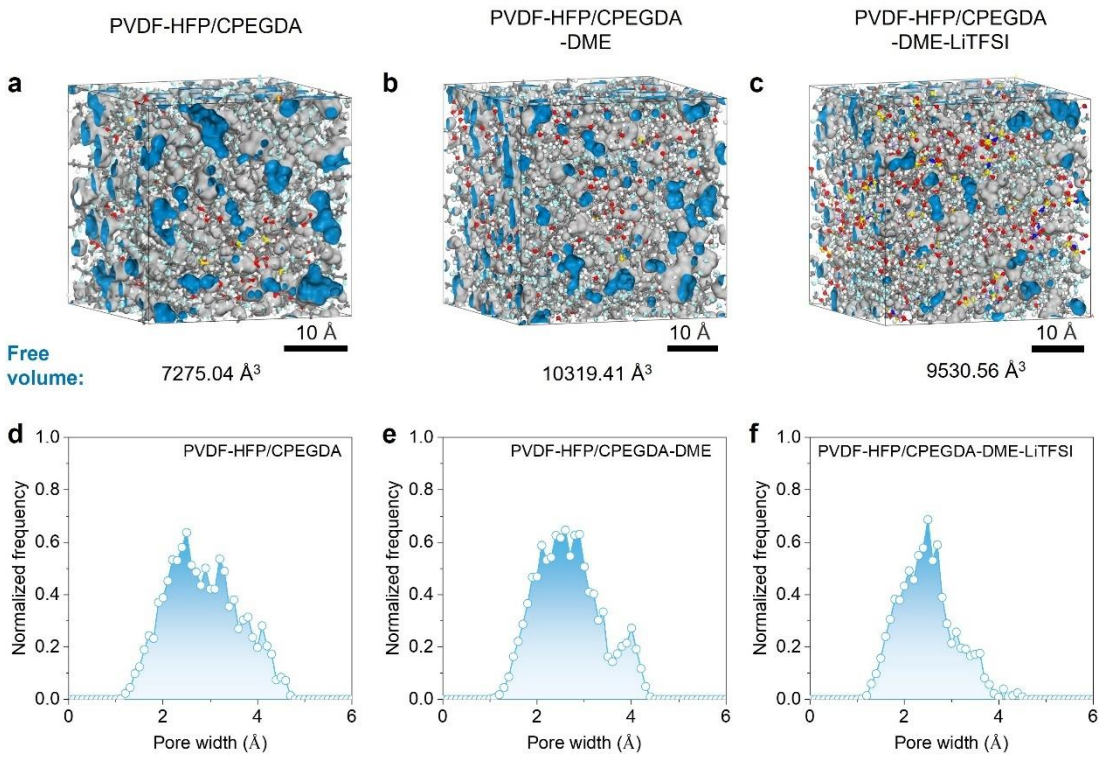

Fig. R34. a-c, Three-dimensional view of fractional free volume models of PVDF-HFP + CPEGDA polymer blends (a), PVDF-HFP + CPEGDA + DME (b), PVDF-HFP + CPEGDA + DME + LiTFSI (c, IHCE) by molecular simulations. The grey surface indicates the van der Waals surface, and the blue surface is the Connolly surface with a probe radius of 1.3 Å. d-f, Normalized pore size distribution derived from molecular simulation as shown in (a-c).

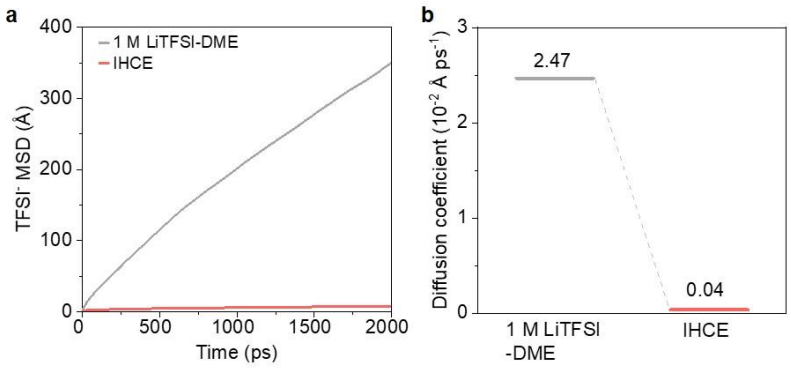

Fig. R35. Calculated MSD as a function of the simulation time (a) and diffusion coefficients of $TFSI^-$ (b) in SCE (1 M LiTFSI-DME) electrolyte and IHCE layer.

5). The Raman analysis part should also compare the IHCE (5 M LiTFSI-DME within a polymer matrix) to a 5 M LiTFSI-DME system without the polymer matrix to provide a more direct understanding of the polymer's role in modulating ion coordination and transport.

Response: We sincerely thank the reviewer for the valuable suggestion. To provide a more direct understanding of the polymer's role in modulating ion coordination and transport, we have conducted additional Raman spectroscopy measurements on the bulk 5 M LiTFSI-DME electrolyte (without the polymer matrix) and systematically compared it with the IHCE system (5 M LiTFSI-DME within a polymer matrix). The comparative analysis yields the following insights:

(1) Ion coordination: Both spectra exhibit deconvoluted peaks within the 740-749 cm^{-1}, corresponding to three distinct $TFSI^-$ coordination environments: solvent-separated ion pairs (SSIPs) at ~740 cm^{-1}, contact ion pairs (CIPs) at ~744 cm^{-1}, and aggregates (AGGs) at ~749 cm^{-1}. Compared to 5 M LiTFSI-DME electrolyte (Fig. R36), IHCE exhibits an increased fraction of CIPs and a reduced fraction of AGGs, suggesting that the polymer matrix alters the local ion solvation structure and suppresses excessive ion clustering.

(2) Ion transport: In 5 M LiTFSI-DME electrolyte, strong Li^+-$TFSI^-$ interactions lead to the formation of AGGs, which are known to impede Li^+ transport. In contrast, the IHCE system shows an increase in CIPs (47.5%) and a meaningful fraction of SSIPs (37.6%), which collectively support more efficient Li^+ mobility. The increased CIPs content contributes to a higher Li^+ transference number, while the presence of SSIPs ensures sufficient ionic conductivity. This balanced coordination environment enables rapid and efficient Li^+ transport across the IHCE layer.

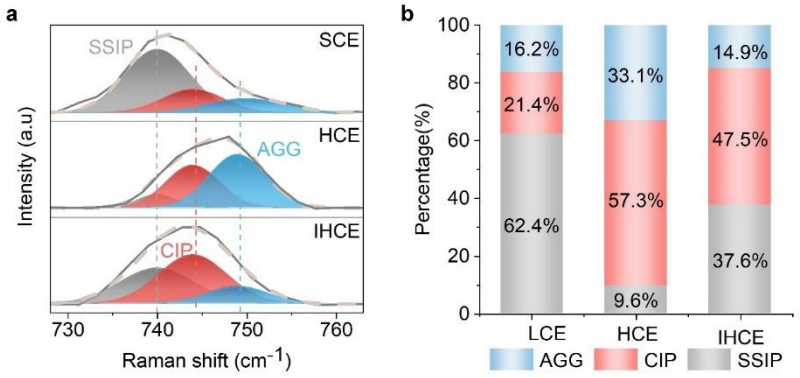

Fig. R36. a, Raman spectra of the SCE (1 M LiTFSI-DME), HCE (5 M LiTFSI-DME) and IHCE (5 M LiTFSI-DME within a polymer matrix), respectively. b, Quantitative analysis of the relative

proportions of SSIPs, CIPs, and AGGs in the corresponding system.

Reference

1. Feng, Y. *et al.* Production of high-energy 6-Ah-level Li | |LiNi0.83Co0.11Mn0.06O2 multi-layer pouch cells via negative electrode protective layer coating strategy. *Nat Commun* **14**, 1–11 (2023).
2. Pokharel, J. *et al.* Manipulating the diffusion energy barrier at the lithium metal electrolyte interface for dendrite-free long-life batteries. *Nat Commun* **15**, 3085 (2024).
3. Xu, J. *et al.* Revealing the Anion–Solvent Interaction for Ultralow Temperature Lithium Metal Batteries. *Advanced Materials* **36**, 2306462 (2024).
4. Wang, C.-Y. *et al.* Fast charging of energy-dense lithium-ion batteries. *Nature* **611**, 485–490 (2022).
5. Kim, S. C. *et al.* High-entropy electrolytes for practical lithium metal batteries. *Nat Energy* **8**, 814–826 (2023).
6. Boyle, D. T. *et al.* Resolving Current-Dependent Regimes of Electroplating Mechanisms for Fast Charging Lithium Metal Anodes. *Nano Lett.* **22**, 8224–8232 (2022).
7. Yu, Z. *et al.* Rational solvent molecule tuning for high-performance lithium metal battery electrolytes. *Nat Energy* **7**, 94–106 (2022).
8. Li, G. Regulating Mass Transport Behavior for High-Performance Lithium Metal Batteries and Fast-Charging Lithium-Ion Batteries. *Advanced Energy Materials* **11**, 2002891 (2021).
9. Jang, J. *et al.* Miniature Li+ solvation by symmetric molecular design for practical and safe Li-metal batteries. *Nat Energy* 1–11 (2025) doi:10.1038/s41560-025-01733-9.
10. Cao, L. *et al.* In Situ-Constructed Multifunctional Composite Anode with Ultralong-Life Toward Advanced Lithium-Metal Batteries. *Advanced Materials* **36**, 2406034 (2024).
11. Zhang, G. *et al.* A monofluoride ether-based electrolyte solution for fast-charging

and low-temperature non-aqueous lithium metal batteries. *Nat Commun* **14**, 1081 (2023).

12. Stephens, P. J., Devlin, F. J., Chabalowski, C. F. & Frisch, M. J. Ab Initio Calculation of Vibrational Absorption and Circular Dichroism Spectra Using Density Functional Force Fields. *J. Phys. Chem.* **98**, 11623–11627 (1994).
13. Ye, G. *et al.* All-Solid-State Lithium Metal Batteries with Microdomain-Regulated Polycationic Solid Electrolytes. *Advanced Materials* **37**, 2417829 (2025).
14. Zhao, Y. & Truhlar, D. G. The M06 suite of density functionals for main group thermochemistry, thermochemical kinetics, noncovalent interactions, excited states, and transition elements: two new functionals and systematic testing of four M06-class functionals and 12 other functionals. *Theor Chem Account* **120**, 215–241 (2008).
15. Boys, S. F. & Bernardi, F. The calculation of small molecular interactions by the differences of separate total energies. Some procedures with reduced errors. *Molecular Physics* **19**, 553–566 (1970).
16. Marenich, A. V., Cramer, C. J. & Truhlar, D. G. Universal Solvation Model Based on Solute Electron Density and on a Continuum Model of the Solvent Defined by the Bulk Dielectric Constant and Atomic Surface Tensions. *J. Phys. Chem. B* **113**, 6378–6396 (2009).
17. Weigend, F. & Ahlrichs, R. Balanced basis sets of split valence, triple zeta valence and quadruple zeta valence quality for H to Rn: Design and assessment of accuracy. *Phys. Chem. Chem. Phys.* **7**, 3297 (2005).
18. Grimme, S., Ehrlich, S. & Goerigk, L. Effect of the damping function in dispersion corrected density functional theory. *J Comput Chem* **32**, 1456–1465 (2011).
19. Sun, H., Ren, P. & Fried, J. R. The COMPASS force field: parameterization and validation for phosphazenes. *Computational and Theoretical Polymer Science* **8**, 229–246 (1998).
20. Ongari, D. *et al.* Accurate Characterization of the Pore Volume in Microporous Crystalline Materials. *Langmuir* **33**, 14529–14538 (2017).
21. Willems, T. F., Rycroft, C. H., Kazi, M., Meza, J. C. & Haranczyk, M. Algorithms

and tools for high-throughput geometry-based analysis of crystalline porous materials. *Microporous and Mesoporous Materials* **149**, 134–141 (2012).

22. Pinheiro, M. *et al.* Characterization and comparison of pore landscapes in crystalline porous materials. *Journal of Molecular Graphics and Modelling* **44**, 208–219 (2013).

Response Letter to Reviews

Review #2 (Remarks to the Author):

Overall comment: This study presents the development of a salt-retaining polymer interfacial layer on electrode surfaces, successfully establishing a localized high-concentration electrolyte microenvironment at the electrode-electrolyte interface. Through comprehensive experimental investigations and computational verification, the research team has systematically addressed the key scientific questions raised during the peer-review process. While the study presents intriguing findings on anion retention by the polymer layer, I have significant reservations regarding the mechanistic interpretation and the claimed novelty of this work. These limitations prevent me to recommend this publication in Nature Communications:

Response: We sincerely appreciate your constructive feedback and thoughtful comments on our manuscript. We are especially grateful for your recognition of our efforts in establishing a localized high-concentration electrolyte microenvironment at the electrode-electrolyte interface and addressing the scientific questions raised during the peer-review process. However, we regret that concerns remain regarding the mechanistic interpretation and the claimed novelty of our work. In response, we have thoroughly revised the manuscript to more clearly elucidate the underlying mechanisms and to further highlight the distinctiveness of our approach in comparison with existing literature.

1. High-concentration electrolytes (HCEs, >3 M salt concentration) have gained significant research attention due to their anion-involved solvation structures, which facilitates preferential anion migration to the electrical double layer (EDL) and form the inorganic-rich SEI. While the authors demonstrate the anion retention capability of this polymer layer, the mechanism by which the retained anions migrate into the EDL and subsequently influence the SEI or CEI remains unclear. Based on classical EDL theory and interfacial reaction kinetics, I question whether such anion retention would significantly alter the EDL structure or SEI/CEI formation dynamics. Could the

localized ion redistribution caused by anion confinement truly control the interphase-formation processes?

Response: We thank the reviewer for raising this important question regarding the relationship between anion confinement, EDL structure, and interphase formation. To clarify this relationship, we provide both theoretical analysis and supporting experimental data below.

The electric double layer (EDL) is the interfacial region at the electrode/electrolyte interface where electrochemical reactions predominantly occur[1,2]. It typically comprises the inner Helmholtz plane (IHP), outer Helmholtz plane (OHP), and a diffusive layer. The structure and composition of the EDL are strongly influenced by the electrode potential, electrolyte composition, and lithium salt concentration[1]. Specifically, the IHP is defined by the locus of specifically adsorbed ionic and molecular species and is directly linked to the subsequent formation of the solid electrolyte interphase (SEI)[3,4]. Thus, reduction of electrolyte species within the IHP represents a dominant pathway for SEI formation.

To understand how electrolyte concentration and polymer confinement influence EDL architecture, we performed molecular dynamics (MD) simulations under a negative field of 0.06 V $Å^{-1}$. In high-concentration electrolytes (HCEs, 5 M LiTFSI-DME), strong ion-pairing effects promote the formation of contact ion pairs (CIPs) and aggregates (AGGs) (Supplementary Fig. 20), resulting in $TFSI^-$ anions integrating into the Li^+ solvation sheath. This allows $TFSI^-$ to co-migrate into the IHP (Figs. R1a, 2a), thereby facilitating inorganic-rich SEI formation through anion reduction[5]. Our interfacial high-concentration electrolyte (IHCE) shares a similar solvation structure with HCE but introduces a key distinction: the electrolyte is confined within a bi-continuous polymer matrix (PVDF-HFP/CPEGDA). This confinement significantly reduces the diffusion coefficient of $TFSI^-$ (Fig. R3), impeding its migration away from the Li interface and enabling anion enrichment at the interface despite electrostatic repulsion. As a result, the EDL is restructured and $TFSI^-$ remains available in the IHP (Figs. R1b, 2a) for localized reduction. To further clarify the role of salt concentration,

we also compared EDL structures of SCE (1 M LiTFSI-DME) and ISCE (SCE confined within the same PVDF-HFP/CPEGDA polymer matrix used in IHCE). In SCE, the solvation environment is dominated by solvent-separated ion pairs (SSIPs)[1], and $TFSI^-$ anions are largely excluded from the IHP due to electrostatic repulsion (Figs. R1c, 2b). ISCE exhibits slightly more $TFSI^-$ near the interface due to limited ion mobility, yet its lower salt concentration maintains an SSIP-dominated structure, with the IHP still primarily occupied by solvents (Figs. R1d, 2b). These results suggest that although polymer confinement restricts ion transport, it is the high salt concentration that is essential for generating an anion-rich EDL.

The details of MD simulations are provided as follows:

All molecular dynamics (MD) simulations were performed using the COMPASSIII force field in Materials Studio 2023. A Li (001) slab–electrolyte interface was modeled, with van der Waals and Coulomb interactions calculated using atom-based and Ewald methods, respectively (cut-off: 12.5 Å). The model was initially subjected to structural optimization. To achieve a thermodynamically stable configuration, we performed an annealing process consisting of 20 cycles, ramping the system temperature between 298 K and 500 K. Simulations were carried out under the NPT ensemble, utilizing the Nose thermostat for temperature control and the Berendsen barostat for pressure regulation. A time step of 1 fs was used, and the total annealing time was 100 ps. Subsequently, the lowest-energy configuration obtained after annealing was fully relaxed under periodic boundary conditions for 4 ns in the NPT ensemble (P = 1 atmosphere, T = 298.0 K). A 5 ns production run was finally conducted in the canonical (constant NVT) ensemble under the Nose-Hoover thermostat. To investigate the influence of external electric fields on ion migration and interfacial structuring, a uniform electric field of 0.05 V $Å^{-1}$ was applied perpendicular to the lithium metal surface (z-direction) during the NVT production run. The simulation time was sufficient to ensure full equilibration of temperature, pressure, potential energy and ion distribution near the electrode interface.

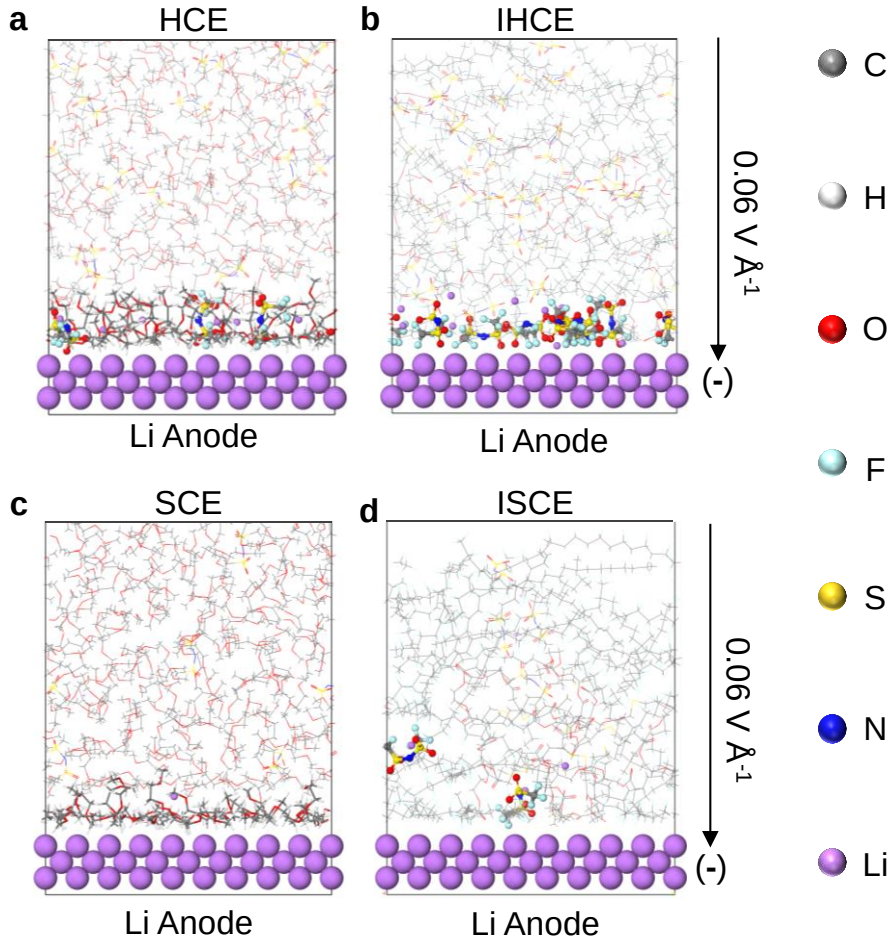

Fig. R1. The relative concentration of $TFSI^-$ molecules near the Li anode surface in HCE (5 M LiTFSI-DME) (a), IHCE (5 M LiTFSI-DME confined in PVDF-HFP/CPEGDA polymer matrix) (b), SCE (1 M LiTFSI-DME) (c), and ISCE (1 M LiTFSI-DME confined in PVDF-HFP/CPEGDA polymer matrix) (d).

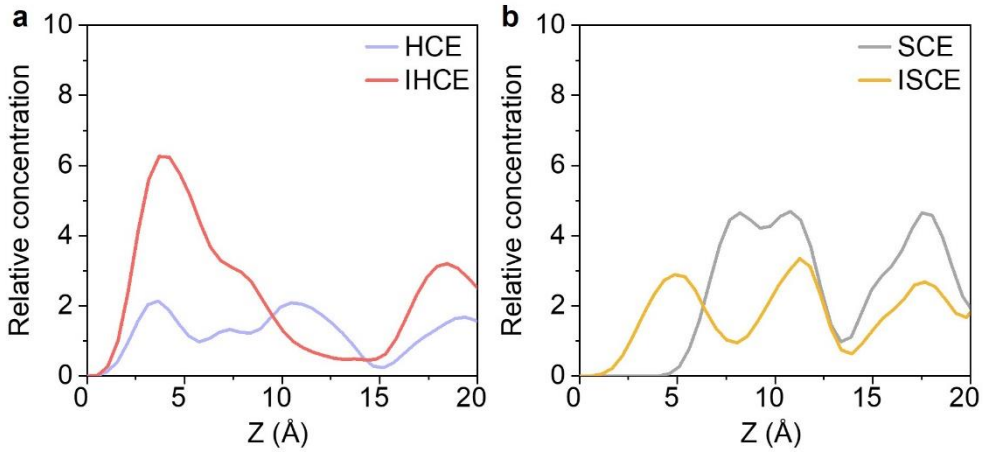

Fig. R2. Relative concentration of $TFSI^-$ in HCE (5 M LiTFSI-DME) and IHCE (5 M LiTFSI-DME confined in PVDF-HFP/CPEGDA polymer matrix) (a), SCE (1 M LiTFSI-DME) and ISCE (1 M LiTFSI-DME confined in PVDF-HFP/CPEGDA polymer matrix) (b) as a function of distance from the anode surface.

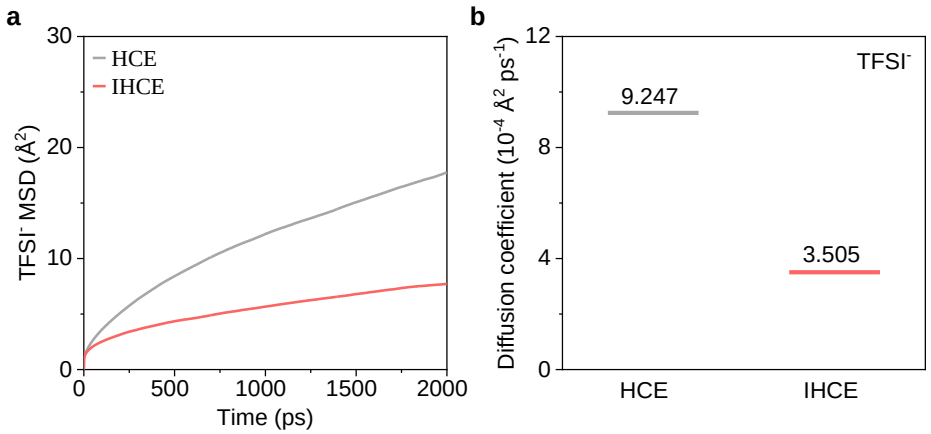

Fig. R3. Calculated MSD as a function of the simulation time (a) and diffusion coefficients of $TFSI^-$ (b) in HCE (5 M LiTFSI-DME) electrolyte and IHCE layer.

To experimentally validate this conclusion, we performed cryo-TEM and TOF-SIMS characterization of SEI morphology and composition for the ISCE system. Cryo-TEM (Fig. R4a) revealed that the SEI formed in the ISCE@Cu is highly amorphous and ~20 nm thick, approximately three times thicker than that in IHCE@Cu (~7 nm, Supplementary Fig. 25). Moreover, 3D TOF-SIMS depth profiling (Fig. R4b) shows that $C_2H_3O^-$ (organic components) and LiF_2^- (LiF) signals reached their maximum peak intensities almost simultaneously in ISCE, with LiF_2^- experiencing a steep drop afterward. This indicates a predominance of organic-rich SEI components in ISCE, consistent with solvent-driven reduction. Moreover, the 3D sputtering images confirmed that SEI components in the ISCE system were sparse and lacked the compact and dense structure observed in the IHCE (Fig. R4c). In contrast, IHCE generates more inorganic-rich fractions in the SEI, supporting the conclusion that anion retention in the IHP directly modulates SEI chemistry.

In summary, both simulations and experimental results demonstrate that high lithium salt concentration plays a decisive role in the reconstruction of EDL, while polymer confinement further enhances anion localization in the IHP. This mechanism of EDL-induced SEI formation is similar to that observed in HCE, where an increased anion accumulation in the IHP facilitates the formation of inorganic-rich SEI via anion decomposition.

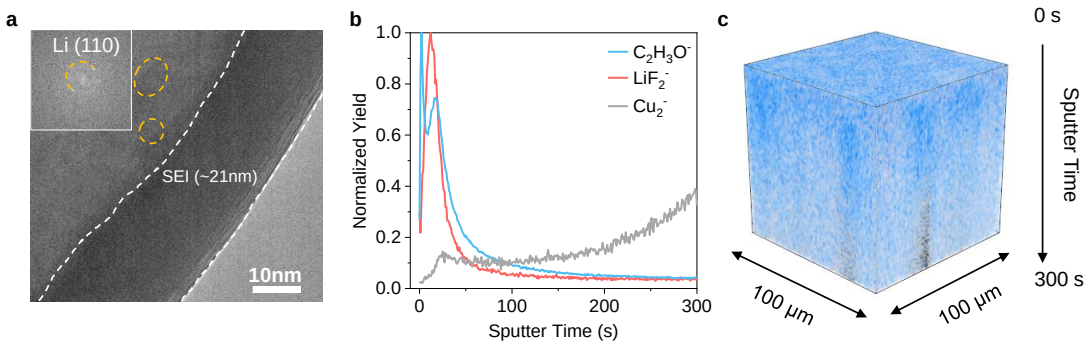

Fig. R4. a, Cryo-TEM images of SEI formed on ISCE@Cu. b, c, TOF-SIMS depth profiles (b) and 3D reconstructed sputtering images (c) of SEI on the cycled ISCE@Cu surface. The red color represents LiF_2^-, the blue color represents $C_2H_3O^-$ and the grey color represents Cu_2^-.

2. The novelty of this work is questionable because PVDF-based coatings on metal anodes have already been extensively explored in prior studies, albeit with differing mechanistic interpretations (Energy Storage Mater. 2020, 24, 588; Nano Lett. 2023, 23, 276). While the current study proposes anion retention as a new mechanism, the core material (PVDF) and its application to metal anodes lack originality.

Response: Thank you for the reviewer's comments regarding the novelty of our work. While PVDF-based materials have been studied previously, we emphasize that our work introduces a fundamentally new interfacial electrolyte architecture with a distinctive design concept, composition, structure, and functionality. To clarify the distinctiveness of our IHCE, we summarized the key differences in Table R1 and provided key distinctions and novelties as follows:

Table R1. Detailed comparison of our work with two representative references.

Category	**This work**	***Energy Storage Mater.* 2020**	***Nano Lett.* 2023**
Polymer	PVDF-HFP + CPEGDA	PVDF	PVDF-HFP
Morphology	Bi-continuous phase-separated structure	Dense	Porous
Ionic conductivity	1.12×10^{-3} S cm^{-1}	Not reported	6.92×10^{-4} S cm^{-1}
Tensile strength	91 MPa	Not reported	Not reported
Solvent uptake	~30 wt%	Not reported	294~370 wt%
Salt retention	3.53 M after 50 days	Not reported	Not reported

(1) Conceptual innovation: Our study introduces a novel concept of an interfacial high-concentration electrolyte (IHCE), which is fundamentally distinct from previously reported electrolyte engineering strategies, such as high-concentration electrolytes (>3 M, HCE) and localized high-concentration electrolytes, as well as other interfacial protection approaches. Instead of saturating the entire electrolyte with high salt concentration (HCE, 5 M LiTFSI-DME), we localized this concentrated environment with a bi-continuous phase-separated polymer matrix at the electrode interface, while maintaining a conventional 1 M electrolyte in the bulk. This strategy enables enhanced Li^+ flux and SEI formation, while preserving the high ionic conductivity and low cost of the 1 M bulk electrolyte. Compared to conventional HCEs, this strategy reduces lithium salt consumption by approximately 70%, while increasing salt usage by only ~0.12‰ relative to standard 1 M systems. Such a gradient-concentration design provides a new paradigm for electrolyte engineering in LMBs.

In contrast, Prior studies (*Energy Storage Mater*. 2020, 24, 588; *Nano Lett.* 2023, 23, 276) focused on different goals. The former reported PVDF defluorination upon reaction with sodium, forming NaF and Na_2O_2-rich SEI layers, with performance improvements attributed to mechanical stiffness and ion conduction through these

products. The latter employed a porous PVDF-HFP scaffold to host LiF nanoparticles (LiF@PPF), enhancing electrochemical performance via mechanical reinforcement by LiF nanoparticles and deposition uniformity through β-phase PVDF.

(2) Distinct composition and structure: As shown in Figs. R5 and R6, the polymer coating reported in *Energy* Storage *Mater.* 2020, 24, 588 is composed solely of PVDF, while the system in *Nano Lett*. 2023, 23, 276 consists of porous PVDF-HFP loaded with LiF nanoparticles (LiF@PPF). In contrast, our IHCE system is composed of PVDF-HFP, cross-linked polyethylene glycol diacrylate (CPEGDA), LiTFSI and DME. This composition forms a bicontinuous, phase-separated polymer matrix due to the immiscibility of hydrophobic PVDF-HFP and hydrophilic CPEGDA, which exhibit a high Flory-Huggins interaction parameter ($\chi = 6.5\ k$, Supplementary Fig. 1 and Note 1). This architecture differs fundamentally from the dense PVDF films in *Energy* Storage *Mater.* 2020, 24, 588 and the porous LiF-filled PVDF-HFP scaffold in *Nano Lett.* 2023, 23, 276. More importantly, this bicontinuous, phase-separated structure is critical for achieving sub-nanoconfinement of solvated $TFSI^-$ anions, which is absent from previous PVDF-based systems.

Figure Redacted

Fig. R5. Compositions and chemical structures of different systems. The polymer coating reported in *Energy Storage Mater.* 2020, 24, 588 is composed only of PVDF. The functional material described in *Nano Lett*. 2023, 23, 276 consists of PVDF-HFP and LiF nanoparticles. In our work, I HCE is composed of PVDF-HFP, CPEGDA, LiTFSI and DME.

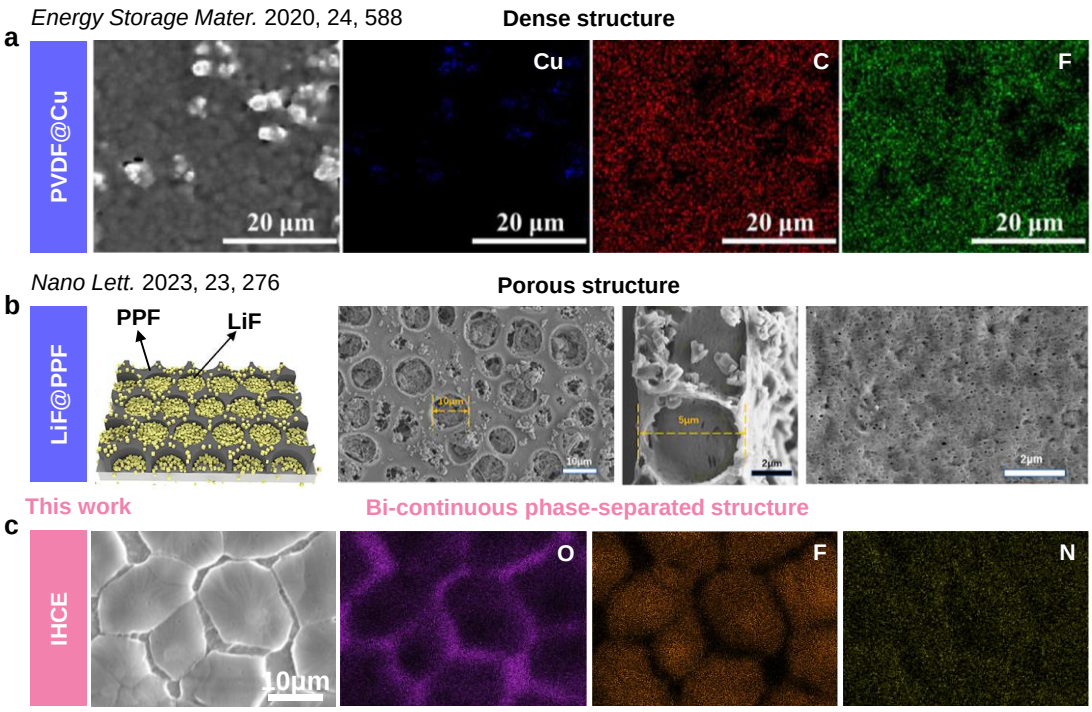

Fig. R6. Morphological comparison of different systems.
a, SEM image and corresponding energy-dispersive spectroscopy (EDS) mapping of PVDF@Cu current collector reported in *Energy Storage Mater.* 2020, 24, 588. The PVDF layer forms a dense and uniform coating on the Cu substrate.
b, Schematic illustration, top-view and cross-view SEM images of LiF@PPF structure reported in *Nano Lett*. 2023, 23, 276. In this system, PVDF-HFP is engineered into a porous framework that serves as a host for LiF nanoparticles.
c, SEM images and corresponding EDS mapping of dry-IHCE developed in this work. PVDF-HFP and CPEGDA components are combined to construct a bi-continuous phase-separated polymer matrix. This unique structural framework enables the confinement of a 5 M LiTFSI-DME electrolyte, thereby establishing a localized interfacial environment with high-concentration electrolyte.

(3) Design and functionality of polymer matrix: We also optimized the ratio of PVDF-HFP and CPEGDA to ensure that the IHCE layer offers mechanical robustness and high ionic conductivity. The resulting IHCE achieves a tensile strength of 91 MPa (Supplementary Fig. 4b), suitable for accommodating volume changes during Li deposition/stripping. Meanwhile, the ionic conductivity reaches 1.12×10^{-3} S cm^{-1} (Supplementary Fig. 4a and Table 2), nearly twice that of the Li@PPF reported in *Nano Lett*. 2023, 23, 276.

Importantly, the solvent uptake of our polymer matrix was controlled at ~30 wt% (Supplementary Table 3), enabling effective confinement of the 5 M LiTFSI-DME

electrolyte without excessive salt consumption. In contrast, the porous PVDF-HFP structure reported in *Nano Lett*. 2023, 23, 276 exhibits solvent uptake > 294 wt%, requiring ~10 times LiTFSI usage to reach comparable salt concentration. For further comparison, we performed salt-retention experiments using dense PVDF-HFP membranes (~41 mg each) immersed in DME, following the same testing protocol and quantification method as applied to the IHCE system (Supplementary Note 4). While the low solvent uptake (~20 wt%, Supplementary Table 3) of dense PVDF-HFP favors high salt concentration with reduced salt usage in principle, the absence of sub-nanoconfinement led to rapid LiTFSI leaching (Fig. R7 and Table R2). In sharp contrast, our IHCE retained a high LiTFSI concentration of 3.53 M even after 50 days (Fig. 3a), demonstrating long-term salt retention ability.

In summary, although PVDF and PVDF-HFP have been used in previous studies, our IHCE is fundamentally different in conceptual framework, chemical composition, structural design and functionality. It incorporates a bi-continuous phase-separated polymer network, tailored solvation structure, and a robust salt confinement mechanism, physical confinement mechanism, collectively enabling long-term interfacial salt retention and effective SEI regulation. We respectfully suggest that this work represents a significant advancement over existing literature and contributes a new conceptual framework for interfacial electrolyte engineering in LMBs.

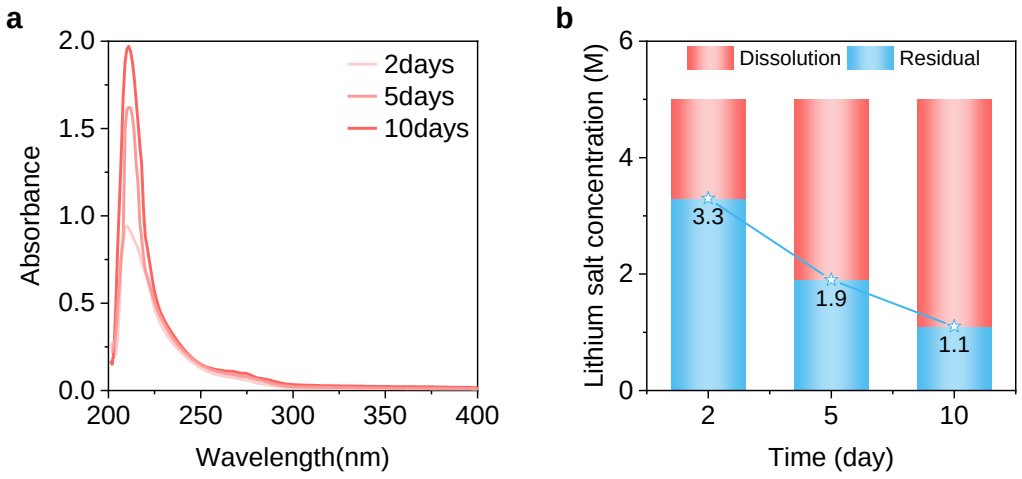

Fig. R7. Quantitative monitoring of LiTFSI dissolution concentration of PVDF-HFP in the DME immersion solution via ultraviolet-visible (UV-Vis) measurements over various days. b, Dissolution and residual concentration profiles of LiTFSI in PVDF-HFP versus immersion time.

Table R2. Parameters of UV experiments.

Time (day)	UV absorbance (y)	LiTFSI in DME		Residual LiTFSI in PVDF-HFP	
		Concentration (x, mg ml^{-1})	Mass (mg)	Mass (mg)	Concentration (M)
2	0.942	1.541	4.623	8.942	1.7
5	1.621	2.834	8.501	5.200	3.1
10	1.971	3.450	10.50	2.957	3.9

3. The proposed anion confinement mechanism remains ambiguously attributed to a combination of physical entrapment, hydrogen bonding, and ion-dipolar interactions. However, the decisive factor remains unclear, weakening the mechanistic foundation of this work.

Response: Thank the reviewer for this insightful comment regarding the need to clarify the dominant mechanism for salt confinement within our IHCE system. We agree that a more precise mechanistic hierarchy is essential for improving the clarity and scientific robustness of the work. To more clearly identify the dominant mechanism responsible for salt retention, we extended our investigations by conducting a series of comparative experiments and computational analyses to decouple the respective contributions of sub-nanometer physical confinement and molecular-level interactions (hydrogen

bonding and ion-dipole interactions).

Specifically, we synthesized a control polymer matrix (PFO) via free-radical copolymerization of perfluorohexylethyl acrylate and polyethylene glycol diacrylate. This matrix provides abundant hydrogen bonding and ion-dipole interactions but lacks a sub-nanoconfined structure of IHCE. Salt retention tests in DME revealed rapid LiTFSI loss in this PFO matrix (Fig. R8 and Table R3), indicating that such weak interactions alone are insufficient for stable salt retention, thus supporting nanoconfinement as the dominant mechanism.

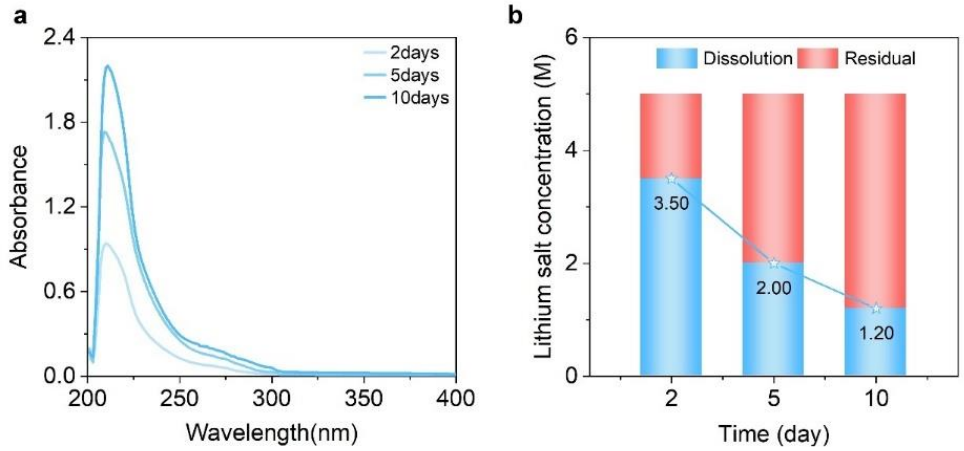

Fig. R8. a, Quantitative monitoring of LiTFSI dissolution concentration of PFO in the DME immersion solution via ultraviolet-visible (UV-Vis) measurements over various days. b, Dissolution and residual concentration profiles of LiTFSI in PFO versus immersion time.

Table R3. Parameters of UV experiments.

Time (day)	UV absorbance (y)	LiTFSI in DME		Residual LiTFSI in PFO	
		Concentration (x, mg ml^{-1})	Mass (mg)	Mass (mg)	Concentration (M)
2	0.942	1.541	4.623	10.743	3.5
5	1.732	3.045	9.135	6.078	2.0
10	2.201	3.936	11.808	3.730	1.2

To further understand the role of molecular-level interactions, we conducted energy decomposition analysis (EDA) using the sobEDA[6] at the B3LYP/6-311+G(2d,p) level, including DFT-D3(BJ) dispersion correction. As shown in Fig. R9, the total binding energy between $TFSI^-$ and three representative environments follows the order PVDF-

HFP-TFSI$^-$ > CPEGDA-TFSI$^-$ > DME-TFSI$^-$. Moreover, the dominant electrostatic energy (E_{els}) in the polymer systems reflects the contributions from hydrogen bonding and ion-dipole interactions, which are significantly weaker in the DME-TFSI$^-$ system. This suggests that the polymer matrix indeed offers enhanced anion stabilization at the molecular level.

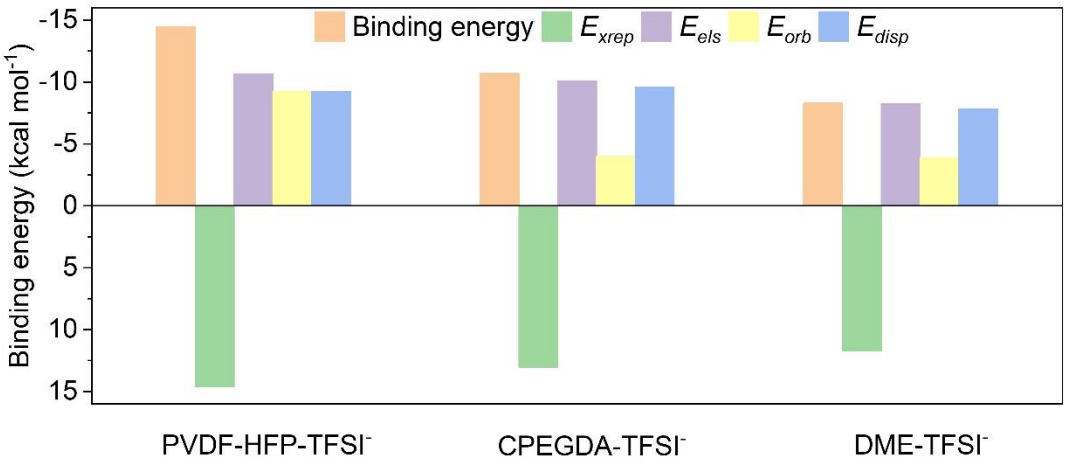

Fig. R9. Bonding energy decomposition. The total bonding energy can be decomposed into four components, including exchange-repulsion energy (E_{xrep}), electrostatic energy (E_{els}), orbital interaction energy (E_{orb}), and dispersion energy (E_{disp}). In all interactions involving PVDF-HFP-TFSI$^-$, PEGDA-TFSI$^-$, and DME-TFSI$^-$, E_{els} serves as the predominant contributor to the overall bonding energy.

To further clarify the contributions of weak interactions, we performed salt retention experiments at 40 °C, above ambient temperature (25 °C) yet below the glass transition temperature of our polymer matrix. Under these conditions, the sub-nanometer physical confinement remains structurally stable, while hydrogen bonding and ion-dipole interactions are expected to weaken. As shown in Fig. R10, the residual LiTFSI concentrations remained nearly unchanged over 20 days (~3.78 M), confirming that the salt retention capability is robust under elevated temperature and is primarily governed by structurally stable nanoconfinement.

In summary, these results support our conclusion that sub-nanometer physical confinement is the dominant mechanism for long-term anion retention in our IHCE system. Molecular interactions such as hydrogen bonding and ion-dipole interactions likely provide short-range stabilization but are insufficient on their own.

We have incorporated these clarifications and supporting results into the revised main text (*Page 7, lines 183-193*) and supplementary information (*Pages 13-15, lines 173-226 and Page 25, lines 316-318*).

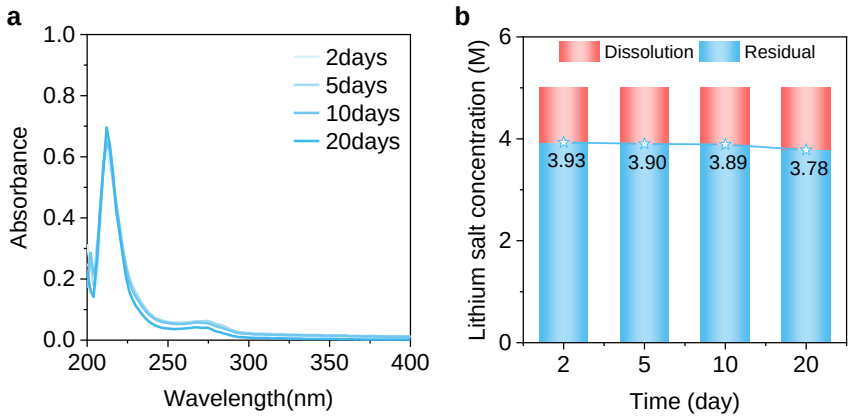

Fig. R10. a, Quantitative monitoring of LiTFSI dissolution concentration of IHCE in the DME immersion solution via ultraviolet-visible (UV-Vis) measurements over various days at 40 °C. b, Dissolution and residual concentration profiles of LiTFSI in IHCE versus immersion time.

Table R4. Parameters of UV experiments.

Time (day)	UV absorbance (y)	LiTFSI in DME		Residual LiTFSI in PFO	
		Concentration (x, mg ml^{-1})	Mass (mg)	Mass (mg)	Concentration (M)
2	0.632	1.07	2.85	10.42	3.93
5	0.645	1.10	2.93	10.32	3.90
10	0.652	1.11	2.97	10.34	3.89
20	0.696	1.22	3.22	9.92	3.78

Reference

1. Wu, J. Understanding the Electric Double-Layer Structure, Capacitance, and Charging Dynamics. *Chem. Rev.* **122**, 10821–10859 (2022).
2. Schott, C. M. *et al.* How to Assess and Predict Electrical Double Layer Properties. Implications for Electrocatalysis. *Chem. Rev.* **124**, 12391–12462 (2024).
3. Kim, J., Zhao, F., Bonagiri, L. K. S., Ai, Q. & Zhang, Y. Electrical Double Layers Modulate the Growth of Solid–Electrolyte Interphases. *Chem. Mater.* (2024).

4. Yan, C. *et al.* Regulating the Inner Helmholtz Plane for Stable Solid Electrolyte Interphase on Lithium Metal Anodes. *J. Am. Chem. Soc.* **141**, 9422–9429 (2019).
5. Wu, Q. & Qi, Y. Revealing heterogeneous electric double layer (EDL) structures of localized high-concentration electrolytes (LHCEs) and their impact on solid–electrolyte interphase (SEI) formation in lithium batteries. *Energy Environ. Sci.* **18**, 3036–3046 (2025).
6. Lu, T. & Chen, Q. Simple, Efficient, and Universal Energy Decomposition Analysis Method Based on Dispersion-Corrected Density Functional Theory. *J. Phys. Chem. A* **127**, 7023–7035 (2023).